Generalized Quantum Master Equations: Getting More for Less

Andrés Montoya-Castillo

Submitted in partial fulfillment of the

requirements for the degree of

Doctor of Philosophy

under the Executive Committee

in the Graduate School of Arts and Sciences

COLUMBIA UNIVERSITY

2016

ABSTRACT

Generalized Quantum Master Equations: Getting More for Less

Andrés Montoya-Castillo

This thesis describes the development of practical and efficient computational approaches to the quantum dynamics of complex systems. Most of the work presented here relies on the generalized quantum master equation (GQME) formalism, which provides a simple equation of motion of reduced dimensionality for a set of dynamical quantities, e.g., nonequilibrium averages and equilibrium time correlation functions. The reduced dimensionality of the GQME comes at a cost: the introduction of the memory kernel, which accounts for the influence of all "excluded" degrees of freedom. Focusing first on the second-order perturbative treatment of the memory kernel known as Redfield theory, I present a collaborative effort to extend its applicability into highly non-Markovian regions via a mode freezing approach. In this method, a portion of bath modes characterized by low frequencies are treated as sources of static disorder and used to calculate modified Redfield dynamics. Application of the method to the spin-boson and FMO complex models indicates that the Redfield+frozen modes scheme consistently produces dynamics that are as good or better than bare Redfield dynamics. Next, we explore GQME approach coupled to the self-consistent solution of the memory kernel, which requires the calculation of auxiliary kernels. Previous implementations of the method had shown impressive boosts in efficiency and, when approximate methods were used to calculate the auxiliary kernels, accuracy over direct calculation of nonequilib-

rium averages. We show that this method, when formulated from the Mori perspective, is equally applicable to nonequilibrium averages and equilibrium correlation functions. In addition, we examine the dependence of the improvements afforded by the GQME framework on the choice projection operator and kernel closure. In particular, we demonstrate that improvements in efficiency, which rely on short memory lifetimes, are sensitively dependent on the choice of projection operator, and that the choice of kernel closure directly dictates the improvements in accuracy. In addition, we present evidence that indicates that the success of the GQME formalism when the auxiliary kernels are calculated via semi- and quasi-classical methods is largely due to the *exact* sampling of bath operators at $t = 0$ required by the calculation of specific kernel closures. Next, we provide analytical arguments that delineate when the GQME framework coupled to the self-consistent solution of the memory kernel is likely to provide improvements in efficiency and accuracy. Finally, we present a path integral framework that can efficiently render the partially Wigner-transformed canonical density operator for systems coupled linearly to harmonic baths. This approach permits the direct calculation of any thermodynamic quantity and can be integrated into dynamical schemes like the Ehrenfest, surface hopping, or linearized semi-classical initial value representation methods to calculate equilibrium correlation functions.

This page is intentionally left blank

Contents

List of Figures

Acknowledgements

I have been immensely fortunate throughout my life and I have many of people to thank. And while I could never truly express the depth of my gratitude, I will at least try to name a few people in the hopes that they will know a fraction of my appreciation for them.

First, I have to thank David Reichman, who has been a great advisor—the type of advisor that many aspire to become. Dave has been a constant source of ideas and inspiration over these last five years. Often, his seemingly innocuous remarks would open new paths of inquiry in my research. With his remarkable knowledge of the literature, he has always been able to suggest the pertinent paper that could shed some light or place in a different perspective the obstacles that invariably arise in the course of research. Dave's questions and intuition have not only taught me how to check and double-check the validity of my results, but also the value of being the most demanding judge of one's own work. Dave's broad interests and attitudes toward science have also informed the way that I identify and approach questions, and his hands-off type of mentoring has given me the freedom to pursue the questions that I find interesting. In short, with a balance of freedom and care, Dave has provided me with the opportunity to grow into the independent thinker that I have become.

I also have to thank Dave for his incredible generosity. When I applied to Columbia's

graduate program in Chemical Physics, I was one of those students whose file had sizable complications. Although severely limited by my immigration situation, which has taken over 15 years to resolve, Dave worked hard to allow me to pursue my graduate studies at Columbia. Without his help and constant support, I am certain that I would not be where I am now.

I also want to thank Ruben Gonzalez, Ann McDermott, and Virginia Cornish, who were similarly instrumental in ensuring that my immigration situation would not deter me from pursuing my graduate studies at Columbia. And, while I am certain that many others also helped me in this regard, I do not know their identities; I apologize for not including them here.

I have also benefited greatly from the team of talented scientists and mentors that composed my committee: Bruce Berne, Rich Friesner, Louis Brus, and Suggy Jang. Their insightful questions and comments have helped shape my understanding of where my research fits in the context of the much larger scientific endeavor. For instance, Bruce's Stat Mech series introduced me to many of the topics of nonequilibrium statistical physics which inform and motivate much of my own current research. Indeed, Bruce has been a strong influence on my development from an early stage; I remember reading and working through (or trying to, at least!) many of his papers on the calculation of time correlation functions and a significant portion of his "Statistical Mechanics – Part B: Time-Dependent Processes" as an undergraduate working in Suggy Jang's group. Rich's classes (quantum and computational chemistry) have also given me a taste for all the things that I am yet to explore as a theorist. In addition, Rich's questions during my presentations always helped me uncover the importance of the practical aspects of my work.

I also had the honor of collaborating with Louis Brus. Whether we were talking about the technical or social aspects of science, Louis was always a source of brilliant insight and moral support. His kind words of encouragement served as an invaluable message to remember during times of self-doubt. In my conversations with him, it became apparent that Louis is the model of a brilliant and balanced scientist. With his questions, Louis opened my eyes to the types of issues that a theorist must address—or at least attempt to—if he or she is to be useful to experimentalists. In addition, his insight into physical systems and his critical eye for what is necessary to describe them reinforced in me the lesson that it is important to approach a problem not with the fanciest of methods, but with the right method.

I want to thank Suggy for his support not only throughout my graduate studies at Columbia, but also for being a thoughtful advisor throughout my years as an undergraduate and Master's student in his group. It was Suggy who introduced me to the world of theoretical chemistry and first showed me many of the topics that continue to interest me today: transition state theory, time correlation functions, and exciton dissociation across an interface, to name a few. He was always a source of invaluable career advice and useful suggestions for research directions. Just as importantly, my work with Suggy prepared me to pursue my graduate studies at Columbia.

Finally, I want to thank my theoretical collaborators, Tom Markland, Aaron Kelly, and Lu Wang. I am particularly glad to have had the chance to share many enriching conversations with Aaron, who also gave me helpful advice as I entered the final stages of my graduate career. I also thank Tom for being supportive of my work and a most welcoming postdoc advisor. I look forward to the work that we will produce in the coming years.

Thanks to my group and friends:

Of course, my life has been greatly enriched from being surrounded by a team of amazing researchers—graduate students and postdocs—who have made my time in the Reichman group a unique experience. I have collaborated with a few, learned from all, and made what I hope to be lasting friendships with them.

I want to thank those with whom I had the chance to collaborate. First, I had the chance to work with Tim Berkelbach on the extension of Redfield theory into non-Markovian regions. I am glad that I was able to learn from Tim's formidable intuition for what makes a problem interesting and his familiarity with and broad understanding of a wealth of topics. I also had the opportunity to learn from and work with Guy Cohen, whose work on the self-consistent solution of the memory kernel as a means of augmenting the reach of numerically exact methods served as my first introduction to this type of approach to generalized quantum master equations (GQMEs). Guy also introduced me to the density matrix renormalization group (DMRG) method, which we are currently using to investigate the dynamics of spin chains from the Mori perspective.

As more or less honorary members of the Reichman group, I am also deeply grateful to Archana Raja and Alexey Chernikov. Alexey graced me with his friendship, advice, and the occasional beer. Archana has been a friend since before joining Columbia as a graduate student; we clicked as early as our visiting weekend, where I surely scared her out of her mind by telling her with unshakable conviction that she should immediately decline all her other offers and come to Columbia. I choose to believe that she never regretted the choice; after all, we shared great friends, good wine, and a hefty amount of delicious food. Archana and I also had the chance to collaborate on a project on energy transfer from quantum dots to MoS_2 and graphene. This project gave me the opportunity to collaborate closely

not only with her, but also with Louis Brus and Tony Heinz, two amazing scientists whose questions never failed to challenge my understanding of energy transfer and always pushed my boundaries to produce deeper and more appealing work.

Although I did not get a chance to collaborate with the other group members, I have learned from each of them. I was happy to overlap, even if only briefly, with Kateri DuBay, Kuljit Virk, Lucia Palova, Marco Schiró, James Dama, Benedikt Kloss, and Jacko Rastikian. Richard Darst and Brenda Rubenstein, two of the senior graduate students in the group when I arrived, were always welcoming and generous in their advice. Tim Berkelbach and Glen Hocky always provided help and useful suggestions about science, where to eat, and fun things to do. I also thank the more recent (and very talented) arrivals—Soumyo Mukherjee, Matt Mayers, Ian Dunn, James Shee, and Arun Nanduri—who have been a pleasure to be around and from whom I have learned much. A few (Soumyo with his phobia of dogs, and Ian with his unintentionally hilarious comments) were particularly good at getting us to laugh. I thank them all.

I also have to thank Yevgeny Bar Lev, first, for being extremely loud and super close to my desk, and second, for being generous with his advice, for sharing his experiences and epiphanies, and for being one of the nicest and most helpful people in the office. He has been supportive throughout my graduate studies and I value his opinions and advice greatly. Roel Tempelaar has been a terrible companion, constantly making inappropriate comments and telling cruel jokes. Luckily, we share the same type of humor so we have gotten along—and amplified each other—pretty well. I will miss him and our 4:00pm coffee/tea + interpretative dance sessions.

Of course, this section would be severely lacking if I didn't thank Liesbeth Janssen and

Hsing-Ta (Theta) Chen. They have been and continue to be incredible sources of strength, patient listeners, and great friends. They have done amazing things for me. Liesbeth, for instance, has instilled in me a lasting and mostly unhealthy veneration of fries with frite sauce, introduced me to the wonders of curry ketchup, and even peer-pressured me into reading the vastly enjoyable *The Goldfinch*. Theta has answered my coding questions throughout the years, endured (and has even become inured to) my humor without complaints, and shared over 1000 cups of coffee with pie/cookies/banana and walnut bread with me. And yet, these examples pale in comparison to all the wonderful things that we have shared. I am truly honored to say that Liesbeth and Theta are my friends.

Life outside the Reichman group has similarly been enriching, in large part because of the friends who were gracious enough to share their precious time with me. I have to thank the "Pie people" for being awesome friends and for having an especially high tolerance for salty chocolate chess and sour cherry pies. Among them, Jaeeun (Jen) Yu, Fang Xu, and Dat Hoang have been constant companions. And, of course, I have to thank my friend, Olga Blik, whose balanced approach to life meant sprinkling the hard and often vexing life of a grad student with cathartic doses of kickboxing, great dinners, delicious drinks, and awesome company.

Thanks to my family:

Naturally, I have a monstrous debt of gratitude to my family that I can never hope to repay. I dedicate this thesis to them.

First, I want to thank Bonnie Blackwell and Joel Blickstein, who have been a second set of parents and mentors in every sense of the word. Since I was accepted and joined the Robert F. Kennedy Science Research Institute as a high school student, Bonnie and Joel

have treated me not so much as a student, but more as their son. They have been with me as I graduated from high school, college, and graduate school, listened to me complain about life and work, accompanied me during my wedding, and I know they will continue to be there as I go through life. Beyond showing me the ropes of electron spin resonance (ESR) spectroscopy and its use in dating archeological sites, Bonnie and Joel have shown me how to be a truly complete person. It is easy to admire their passion for science, their commitment to identifying promising students and providing them with the tools to pursue their dreams, and their generosity. I am truly fortunate in having found them as a high school student and I am even more fortunate that they have decided to encourage and love me all these years. I can only hope to make them proud.

My family is large and wonderful and I would like to thank them all. First, I thank my late uncle, Jaime, who instilled in me the love for science from an early age. In all regards he has been my role model: his brilliance and deep understanding of science, his dedication to his family, and his humility are all qualities I strive for. I wish he could be around to see me obtain my doctorate. My aunt, Inés, has loved and supported me since I was a young kid. She still makes me laugh as she tells me stories of my childhood. I also thank my extended family for all their support.

Most importantly, I thank my parents Angela and Alberto, and my siblings Andrea and Tomás. They have done more for me than I could ever recount and I am more grateful to them than I could ever say. They have been a constant source of strength and unconditional support. I love and admire them beyond words.

Finally, I thank my husband Carlos for his unwavering support all these years, for enduring my anxiety without complaint, and for laughing at my jokes even when they aren't

funny. His love and support have meant the world.

For my family.

Chapter 1

Introduction

1.1 Motivation

The simulation of quantum dynamics in condensed phases is both one of the major goals of current theoretical research and also one of its most enduring challenges. Superficially, the problem seems simple: solve the time-dependent Schrödinger equation. The complication arises from the explosion of dimensionality encountered in its direct assault, which makes addressing the dynamics of over ~ 10 interacting particles essentially impossible. The magnitude of this difficulty also implies that a universal approach to the calculation of quantum dynamics is unlikely to exist. To make progress, one must instead resort to approximations, the success of which often depends sensitively on the details of the system.

There are several canonical models that are known to capture much of the rich physics in the condensed phase [1–9]. As such, these models serve as the tools with which to investigate and model physical phenomena and also as the gold standards for determining whether new

dynamical methods are reliable. Among these is the spin-boson (SB) model [1, 2], which consists of a two-level system coupled linearly to an infinite bath of harmonic oscillators. It is the minimal model that describes quantum dissipation and captures the rich physics of, for instance, electron and energy transfer in molecular systems [10, 11], entanglement in many-body quantum systems [12–14], and the spectroscopy of coupled chromophores [15]. Hence, it is not surprising that a many research efforts are devoted to the development of accurate and practical dynamical schemes that recover the dynamics of the SB model and can be applied to more realistic systems. We use the SB model and its seven-site generalization, which has been used extensively to study the dynamics of the Fenna-Matthews-Olsen complex [16, 17], as a testing ground for the reliability of the methods we develop in this thesis.

1.2 Theoretical approaches

Vigorous research efforts over the last several decades have produced an array of numerically exact methods for the treatment of the dynamics of select model systems [18–38]. To reach convergence, these methods depend on certain detailed properties of the system that render the numerical procedure feasible. For instance, the quasi-adiabatic path integral (QUAPI) [18–21] scheme expoits the finite range of nonlocal interactions in the analytically known influence functional to truncate the path integral expansion it requires, whereas the hierarchical equations of motion (HEOM) [22–24] method relies on the noninteracting nature of the oscillator bath and the truncation of the rigorously infinite hierarchy of coupled equations. However, these approaches are often beset by severe limitations. For example, both QUAPI and HEOM become computationally expensive and difficult to converge in regions

of strong system-bath coupling and low temperature in the SB model. On the other hand, while quantum Monte Carlo (QMC) techniques [30–33] are not restricted to a particular system, their use in the calculation of dynamical properties must contend with myriad paths, each weighted by a complex phase. The need for the cancellation of many of these paths results in the exponential decrease of the signal-to-noise ratio with increasing path length, redering the QMC approach unstable at long times.[1] Hence, as the previous considerations suggest, the high accuracy of numerically exact methods can come at the price of general applicability and computational efficiency.

The development of robust and versatile, even if approximate, techniques [1, 2, 42–78] capable of treating a wide range of problems has also been of great importance. Of particular relevance to the work presented here are those techniques based on perturbative and semi- and quasi-classical approaches. These schemes can be used to address the dynamics of systems that range from simple models to realistic, multidimensional systems, but each suffers from different difficulties.

Perturbation theory, for instance, capitalizes on the similarity between a complex problem and an exactly solvable one and provides a simple protocol capable of producing highly accurate results in regions where the perturbation parameter remains small. However, perturbation series are not necessarily convergent and can lead to unphysical results when the perturbation parameter becomes substantial. Specifically, Redfield theory [42, 43], which is a second-order perturbative expansion with respect to the system-bath coupling, is known

[1]Recent progress based on bold line QMC [39, 40], the continuous-time formulation of QMC [33], and the development of the efficiency-boosting Inchworm algorithm [41] have enabled the calculation of long-time dynamics for select models. Much work is necessary to determine whether these approaches will be trasferrable to a broad class of systems.

to fail for cases characterized by strong system-bath coupling or baths containing significant portion of slow modes [79–81].

The semiclassical family of methods takes a fundamentally different approach. This hierarchy of techniques [44–57, 65–67] replaces the exponential scaling characteristic of quantum dynamics with the calculation of linearly scaling classical trajectories that can be used to construct quantum mechanical propagators. By virtue of their proximity to direct classical simulations, semiclassical methods often provide an intuitive grasp of the processes that dominate a system's behavior. Importantly, these methods range in complexity and, depending on their level of sophistication, are capable of yielding accurate dynamics for a class of systems. The most sophisticated of these, however, require the cancellation of phases in the construction of the propagators and consequently suffer a dynamical sign problem, similar to that of QMC-based methods, that make them exponentially difficult to simulate long times. The most computationally efficient but also generally the least accurate semiclassical method is the linearized semiclassical initial value representation (LSC-IVR) scheme [65–67], which simply averages classical trajectories subject to appropriate quantum mechanical initial conditions given by the Wigner formulation.

Closely related to the LSC-IVR method are the quasi-classical Ehrenfest [61, 62] and surface hopping [63, 64] methods, which treat a portion of the system classically while treating the rest quantum mechanically. These methods differ primarily in the *ad hoc* algorithms used for the evolution of classical and quantum parts of the system. Despite their simplicity, these methods are capable of accurately reproducing the coherent to incoherent behavior exhibited by the SB model, and are remarkably efficient and scalable to large, realistic systems [82–87]. A major drawback, however, is that these approaches often rely on uncontrolled

approximations that make it difficult to predict when they will fail. Naturally, the simplicity of these methods makes the extension of their applicability region highly desirable.

1.3 Generalized Quantum Master Equations

In light of the previous discussion, it is clear that the successes and failures of many of the methods outlined above are intimately related to their ability to effectively ameliorate the severity of the quantum catastrophe of dimensionality. In this respect, one more theoretical tool must be mentioned: the projection operator technique. With this technique it is possible to reduce, at least formally, the dimensionality of a problem and obtain a generalized quantum master equation (GQME) of the form,

$$\dot{\mathcal{C}}(t) = \mathcal{C}(t)\dot{\mathcal{C}}(0) - \int_0^t d\tau\ \mathcal{C}(t-\tau)\mathcal{K}(\tau). \tag{1.1}$$

Here, $\mathcal{C}(t)$ contains the set of nonequilibrium averages or time correlation functions that one seeks to calculate. These quantities can range from excitation dynamics in molecular systems, density fluctuations in normal and supercooled liquids, and even out-of-equilibrium currents of the type observed accross nanojunctions. Importantly, the dimensionality of $\mathcal{C}(t)$ can be significantly smaller than that of the full system. Taking the example of excitation dynamics in molecular systems, one can envision a system consisting of N states corresponding to different electronic excitations coupled to an extended structural backbone, say a protein or a molecular crystal, which is often called the bath. If one is interested solely in the dynamics of the electronic excitations, $\mathcal{C}(t)$ can consist of as few as N–N^2 components, where the potentially infinite number of states corresponding to the excitations of the bath have been formally eliminated.

One additional function appears in Eq. (1.1), the memory kernel which takes the form,

$$\mathcal{K}(t) = (\mathbf{A}|\mathcal{L}\mathcal{Q}e^{i\mathcal{Q}\mathcal{L}t}\mathcal{Q}\mathcal{L}|\mathbf{A}), \tag{1.2}$$

where $\mathbf{A}$ is a vector that contains the observables probed in $\mathcal{C}(t)$, $\mathcal{L}$ is the Liouvillian operator for the entire system and bath, and $\mathcal{P} = 1 - \mathcal{Q} = |\mathbf{A})(\mathbf{A}|$ is the projection operator that projects into the subspace of the observables in $\mathbf{A}$.[2]

While the dimensionality of Eq. (1.1) is indeed smaller than that of the full system, the original difficulty of the problem is shifted to the calculation of the memory kernel. Indeed, full knowledge of the memory kernel is tantamount to solving the original problem. Calculation of the memory kernel, however, is complicated by two factors. First, the original dimensionality of the problem resurfaces in the time evolution. Second, the projected propagator $e^{i\mathcal{Q}\mathcal{L}t}$ makes direct evolution problematic. These difficulties notwithstanding, the GQME has served and continues to serve as fertile ground for the development of highly successful dynamical approaches [1, 2, 24, 42, 43, 88–106] . The work in this thesis is largely concerned with the use of GQME as a starting point for the development of accurate and practical approaches to the quantum dynamics of complex systems in the condensed phase.

1.4 Outline

With the context provided by the above discussion, I now provide a detailed outline of this thesis. All work presented here was completed under the guidance of, and in collaboration with, Prof. David R. Reichman.

[2]We defer discussion of details, including the definition of the inner product $(\mathbf{A}|\mathbf{B})$ and the requirements on $\mathcal{P}$, to Chapters 3, 4, and 5 in the thesis.

In Chapter 2, we introduce a physically motivated and computationally simple modification that extends the applicability of the Redfield equations into highly non-Markovian regimes. This approach exploits the realization that low frequency bath modes, which lead to the failure of Redfield theory, evolve on a slower timescale than the system dynamics and are therefore effectively frozen. We apply the method to the SB and standard FMO complex models and find that the the frozen modes approximation dramatically improves the Redfield dynamics in highly non-Markovian regimes, at a similar computational cost. This work was done in collaboration with Timothy C. Berkelbach.

In Chapters 3, 4, and 5, we provide a unified Mori-Nakajima-Zwanzig formulation to nonequilibrium averages and equilibrium correlation functions for the SB model. Employing a Dyson-type expansion to circumvent the difficulty of projected dynamics, we obtain a self-consistent equation for the memory kernel which requires only knowledge of normally evolved auxiliary kernels.

In Chapters 3 and 4, we illustrate the properties of this approach by focusing on the SB model and limiting our attention to the use of a simple and inexpensive quasi-classical dynamics, given by the Ehrenfest method, for the calculation of the auxiliary kernels. For the first time, we provide a detailed analysis of the dependence of the properties of the memory kernels obtained via different projection operators. we further elucidate the conditions that lead to short-lived memory kernels and the regions of parameter space to which this program is best suited. Via a thorough analysis of the different closures available for the auxiliary kernels and the convergence properties of the self-consistently extracted memory kernel, we identify the mechanisms whereby the current approach leads to a significant improvement over the direct usage of standard semi- and quasi-classical dynamics. Importantly, we find

that the success of the current approach relies, to a large extent, on the *exact* sampling of *distinct* system-bath operators at $t = 0$ required for the calculation of the auxiliary kernels.

In Chapter 5, we present the analytical proofs that show what kernel closures are certain to recover the original dynamics used to calculate the axulilary kernels, regardless of the method used. Importantly, we also provide the requirements whose violation could lead to GQME dynamics that are *distinct* from those achievable via the method used to calculate the auxiliary kernels. This work was done in collaboration with Aaron Kelly, Lu Wang, and Thomas E. Markland.

Finally, in Chapter 6, we derive an analytical form for the Wigner transform for the canonical density operator of a discrete system coupled to a harmonic bath based on the path integral expansion of the Boltzmann factor. We show that this scheme can be made arbitrarily accurate with increasing number of path integral slices. We also demonstrate the feasibility of the method for the calculation of thermodynamic averages and the methods compatibility with quasi- and semi-classical dynamical schemes via the calculation of the correlation function $\mathcal{C}_{zz}(t) = \text{Re } \langle \sigma_z(0)\sigma_z(t) \rangle$ for the SB model using the Ehrenfest method. The results for $\mathcal{C}_{zz}(t)$ illustrate that accurately rendering the canonical density operator can significantly improve the results for time-correlation function obtained using semi- and quasi-classical methods.

Chapter 2

Extending the applicability of Redfield theories into highly non-Markovian regimes[1]

2.1 Introduction

Useful approximate methods for the description of quantum dynamics and relaxation can often circumvent the large computational expense of numerically exact approaches while maintaining quantitative accuracy in certain regions of parameter space. The general applicability of such methods, however, is often limited and their domain of validity difficult to assess. The most widely used approximate approaches fall into two broad and general classes.

[1]Based on work published in J. Chem. Phys. **143**, 194108 (2015). Copyright 2015, American Institute of Physics.

The first class of methods involves techniques that employ uncontrolled approximations to yield dynamics which are non-perturbative in the various couplings (e.g., intra-system or system-bath) that characterize the problem. The second class of methods are systematically perturbative in a well-defined coupling parameter, but are free from further classical or semiclassical approximations, at least for simply defined models such as a the spin-boson (SB) model.

One of the most celebrated perturbative techniques is a lowest-order treatment of the system-bath coupling, known traditionally as Redfield theory [42, 43, 107]. As we will show later, the relevant dimensionless parameter characterizing the accuracy of Redfield theory is $\eta = \max\left[2\lambda/\beta\omega_c^2, 2\lambda/\pi\omega_c\right]$, where λ is the nuclear reorganization energy, $\beta = 1/k_B T$ is the inverse temperature, and ω_c is a characteristic bath frequency (we henceforth work in units with $\hbar = 1$). Redfield theory becomes unreliable when $\eta \gtrsim 1$. We emphasize that η is controlled by multiple bath parameters and, in particular, low frequency degrees of freedom (small ω_c) limit the range of accessible reorganization energies. Indeed, violations of this condition explain the failures of Redfield theory found by Ishizaki and Fleming [24] for certain models of excitation energy transfer, which appear to be characterized by low-frequency protein baths.

While the very lowest frequency degrees of freedom are thus most problematic for Redfield theory to handle (even in its non-Markovian forms), it is often the case that nuclear modes of such frequencies are effectively frozen on the time scale of relevance for the system's dynamics. In this regard, the key function of such modes is simply to provide static energetic disorder for the more rapidly evolving degrees of freedom. This suggests a methodology whereby the very low frequency phonons are approximated as static (and treated

non-perturbatively as a source of static disorder), while the remaining portion of the bath is treated dynamically within Redfield theory. Here we develop this "Redfield theory with frozen modes" (Redfield-FM) method, and show that it greatly extends the applicability of Redfield theory into highly non-Markovian dynamical regimes at essentially no change in computational cost.

The outline of this paper is as follows. In Sec. 2.2, we introduce the theoretical background for the Redfield equations and the derivation and general properties of the Redfield-FM extension. In addition, we also introduce the spin-boson Hamiltonian as the model system on which we test the methods developed in this paper. Section 2.3 presents the computational details in the implementation of the Redfield-FM method, while Sec. 2.3 presents illustrative results for the method. Sec. 2.3 introduces the generalization of the Redfield-FM approach to a multi-site system and presents representative results. In Sec. 2.3, we relax the mode-freezing approximation via the derivation and implementation of a dynamical hybrid method (hybrid-Redfield) that combines Redfield dynamics for the high-frequency part of the bath coupled to the electronic system and Ehrenfest dynamics for the low-frequency modes. In Sec. 2.4, we conclude.

2.2 Theory

Model

First, we briefly describe the model system we use to test the approximations developed in subsequent sections. This allows us to define notation and parameters that will be used

in our numerical comparisons. We focus on the well-known SB model, which consists of a two-level system coupled linearly to a harmonic bath. This model has been extensively used to investigate a wide variety of relaxation, charge and energy transport processes in condensed phase systems [2].

The total Hamiltonian is divided into system, bath, and interaction components, $H = H_{\text{sys}} + H_{\text{bath}} + V$. The system Hamiltonian takes the form

$$H_{\text{sys}} = \varepsilon\sigma_z + \Delta\sigma_x, \tag{2.1}$$

where σ_i, $i = \{x, y, z\}$, are the Pauli matrices, 2ε is the energy difference, and Δ is the coupling between the two electronic sites, which is here assumed to be static. The bath Hamiltonian consists of an infinite set of harmonic oscillators,

$$H_{\text{bath}} = \sum_k \frac{1}{2}\left[P_k^2 + \omega_k^2 Q_k^2\right]. \tag{2.2}$$

Lastly, the system-bath interaction couples the electronic states linearly to coordinates of the bath oscillators,

$$V = \sigma_z \sum_k c_k Q_k. \tag{2.3}$$

Physically, the system-bath coupling acts as a (quantum) fluctuating field that shifts the origin of the bath harmonic oscillators by a magnitude that depends on the system's electronic state and the strength of the coupling.

The spectral density, which completely determines the coupling between the bath and the system, is taken to be Ohmic with a Lorentzian cutoff (Debye form),

$$\begin{aligned} J(\omega) &= \frac{\pi}{2}\sum_k \frac{c_k^2}{\omega_k}\delta(\omega - \omega_k) \\ &= 2\lambda\omega_c \frac{\omega}{\omega^2 + \omega_c^2}. \end{aligned} \tag{2.4}$$

The cutoff frequency, ω_c, characterizes how quickly the bath relaxes toward equilibrium, while the reorganization energy, $\lambda = \pi^{-1}\int_0^\infty d\omega\ J(\omega)/\omega$, characterizes the energy dissipated by the environment after a Franck-Condon transition between electronic states. It is important to note that the methods studied here are neither limited to the SB model nor to the Debye form for the spectral density.

Time-local Redfield Dynamics

Because of its simplicity in the time domain we employ the time-local (i.e. time-convolutionless) form of the generalized Redfield equations. A full derivation of these equations is contained in Appendix 2.A. Here our aim is to highlight important but often overlooked aspects pertaining to the applicability of the Redfield approach. For the SB model, the time-local version of the Redfield theory takes the following form,

$$\begin{aligned}\frac{d}{dt}\rho(t) = &-i\left[H_{\rm sys}, \rho(t)\right] \\ &- \int_0^t d\tau\ \Big\{C(\tau)\left[\sigma_z(0), \sigma_z(-\tau)\rho(t)\right] - C^*(\tau)\left[\sigma_z(0), \rho(t)\sigma_z(-\tau)\right]\Big\},\end{aligned} \tag{2.5}$$

where all operators except the reduced density matrix (RDM) are evolved in the interaction picture, $O(t) = e^{i(H_{\rm sys}+H_{\rm bath})t}Oe^{-i(H_{\rm sys}+H_{\rm bath})t}$, and the free bath correlation function is given by

$$\begin{aligned}C(t) &= \sum_k c_k^2 {\rm Tr}_{\rm bath}\Big\{\rho_{\rm bath}Q_k(t)Q_k(0)\Big\} \\ &= \frac{1}{\pi}\int_0^\infty d\omega J(\omega)[\coth(\beta\omega/2)\cos(\omega t) - i\sin(\omega t)].\end{aligned} \tag{2.6}$$

By going to the interaction picture with respect to $H_{\text{sys}} + H_{\text{bath}}$ (to eliminate the free-evolution) and formally integrating the equation of motion (2.5), one finds

$$\rho_I(t) = \rho_I(0)\left[1 + O\left(\int_0^t d\tau_1 \int_0^{\tau_1} d\tau_2\ C(\tau_2)\right) + \dots\right]. \tag{2.7}$$

Examination of the function $\int_0^t d\tau_1 \int_0^{\tau_1} d\tau_2\ C(\tau_2)$ reveals the natural dimensionless parameter that determines the limit of validity of Redfield theory. In general, even in the non-Markovian case, we expect that the ordering of terms in the expansion (2.7) is governed by the function $\int_0^t d\tau_1 \int_0^{\tau_1} d\tau_2\ C(\tau_2) = \eta g(t)$, where η is a dimensionless constant and $g(t)$ is a function expressed in terms of a scaled, dimensionless time variable. In the high-temperature limit ($\beta\omega_c \ll 1$), where $C(t) \approx (2\lambda/\beta)e^{-\omega_c t}$, it is easy to show

$$\eta = 2\lambda/(\beta\omega_c^2) \tag{2.8a}$$

$$g(t) = e^{-\omega_c t} - 1 + \omega_c t. \tag{2.8b}$$

In the low-temperature limit ($\beta\omega_c \gg 1$), we assume that the low-frequency behavior of the spectral function dominates, so we choose $J(\omega) = (2\lambda\omega/\omega_c)e^{-2\omega/\pi\omega_c}$ as an approximation to the Debye form in Eq. (2.4) that exactly matches the value of λ and its low-frequency asymptotic behavior. Using this spectral density, one can show

$$\eta = \frac{2\lambda}{\pi\omega_c} \tag{2.9a}$$

$$g(t) = \ln\left[1 + (\omega_c t)^2\right] + 2\ln\left[\frac{\sinh(\pi t/\beta\hbar)}{(\pi t/\beta\hbar)}\right]. \tag{2.9b}$$

Thus, for a Debye spectral density, Redfield theory will be reliable as long as $\max\left[2\lambda/\beta\omega_c^2, 2\lambda/\pi\omega_c\right]$ is not significantly larger than unity.[2] It should be noted that re-

[2]This criterion is only approximately valid because it ignores the magnitude of the system timescales. A more rigorous expression could be obtained via direct examination of the ratio of the 2^{nd} and 4^{th} order terms that may be found, e.g., in the work of Laird and Skinner [79] or Ref. [80].

cent work purported to be in the Redfield limit actually violates the above condition [108]. As long as the relevant energy scales in the system Hamiltonian are not too large, we expect the above to hold. In cases where the system's bare energy difference ε is the largest energy scale in the problem, the dynamics will be mediated by multi-phonon processes which are a challenge for lowest-order Redfield-like theories. However, in this limit, the problem acquires an increasing amount of 'pure-dephasing' character, for which the time-local version of Redfield theory provides an exact multi-phonon resummation.

Redfield Theory with Frozen Modes

As discussed in the Introduction, low-frequency bath modes ω_k which lead to a violation of the validity of the Redfield theory frequently evolve so slowly as to be effectively static on the electronic timescale. Here we develop the "Redfield theory with frozen modes" (Redfield-FM) method, based on the physically appealing notion of dividing modes into a low-frequency portion (treated as static disorder), and a high-frequency bath (treated by time-local Redfield theory). The separation of modes used here mirrors that utilized in previous work on a Förster-like dynamical hybrid approach [109]. The approach presented here is not in any way limited to time-local Redfield theory (nor even to any specific flavor of Redfield theory). However, due to pathologies associated with a strictly Markovian Redfield theory, we suggest certain adjustments to the partitioning algorithm, as discussed in Appendix 2.B.

First, it is advantageous to assume that the total density matrix is multiplicatively separable into weakly interacting parts, i.e., $\rho_{\text{tot}}(t) \approx \rho_{\text{slow}}(0)\rho_{\text{sys+fast}}(t)$ where $\rho_{\text{slow}}(0)$ is the density matrix of the frozen low-frequency "slow modes" and $\rho_{\text{sys+fast}}(t)$ is the density matrix for the system and high-frequency "fast modes". As in Ref. [109], a splitting function, $S(\omega)$,

divides the spectral density into two components, $J(\omega) = J_{\rm slow}(\omega) + J_{\rm fast}(\omega)$, where

$$J_{\rm slow}(\omega) = S(\omega, \omega^*) J(\omega), \tag{2.10}$$

and

$$J_{\rm fast}(\omega) = [1 - S(\omega, \omega^*)] J(\omega) \tag{2.11}$$

Here we take the same form of the splitting function as that suggested in Ref. [109], namely,

$$S(\omega, \omega^*) = \begin{cases} [1 - (\omega/\omega^*)^2]^2 & : \quad \omega < \omega^* \\ 0 & : \quad \omega \geq \omega^*, \end{cases} \tag{2.12}$$

which, by virtue of its smoothness, avoids problems associated with long-time oscillatory tails in the bath correlation function [109]. While the above splitting induces no errors if the dynamics are treated exactly, it is clear that ω^* serves as a free parameter that allows one to tune the optimum percentage of frozen bath modes, and hence the accuracy of the results if the dynamics are treated within our approximate method. The utility of the present method is greatly enhanced if a physical *a priori* prescription for choosing ω^* based only on the parameters of the initial Hamiltonian can be put forth. In this work we choose $\omega^* = \max[\omega_c, \omega_R/4]$, where $\omega_R = 2\sqrt{\varepsilon^2 + \Delta^2}$ is the system Rabi frequency. This choice for ω^* is simple, yields non-trivial improvements over standard Redfield theory, and may easily be generalized to multiple electronic states. Physically, this choice partitions the bath into modes that evolve slower than the system (to be treated as frozen) and modes that evolve faster than the system (to be treated via Redfield theory). However, it should be noted that this choice is not always optimal. Future work will be devoted to the goal of arriving at an optimal choice of ω^*. Other choices for ω^* that fit within the general physical guidelines discussed above will be discussed in the Results section.

With a prescription for choosing ω^* in hand, it is possible to separate the fast and slow portions of the Hamiltonian, starting with the interaction, $V_{\rm fast} = \sigma_z \sum_{k\in{\rm fast}} c_k Q_k$ and $V_{\rm slow} = \sigma_z \sum_{k\in{\rm slow}} c_k Q_k$. Regrouping terms, it is evident that freezing the slow part, $V_{\rm slow}$, will yield a classical reorganization energy that renormalizes the bias for every realization of the bath's initial conditions. The modified total Hamiltonian now takes the following form,

$$H' = [\varepsilon + \lambda^{cl}(0)]\sigma_z + \Delta\sigma_x + \sigma_z \sum_{k\in{\rm fast}} c_k Q_k + \frac{1}{2}\sum_k \Big[P_k^2 + \omega_k^2 Q_k^2\Big], \tag{2.13}$$

where the classical reorganization energy is defined as $\lambda^{cl}(0) = \sum_{k\in{\rm slow}} c_k Q_k(0)$ and the set of $Q_k(0)$ is sampled from a bath distribution function after the discretization of $J_{\rm slow}(\omega)$. Physically, each realization of the frozen bath degrees of freedom constitutes a local, rigid environment that modifies the site energies for the system Hamiltonian. The time-local Redfield dynamics, under the Hamiltonian in Eq. (2.13) with an interaction given by $V_{\rm fast} = \sigma_z \sum_{k\in{\rm fast}} c_k Q_k$, are subsequently ensemble averaged with respect to the slow frozen modes. Thus, there are two important differences for the Redfield equations used in each realization of the frozen modes: (i) the bias is given by $\tilde{\varepsilon} \equiv \varepsilon + \lambda^{cl}(0)$, and (ii) the bath correlation function given by Eq (2.6) is modified, with $J(\omega)$ replaced by $J_{\rm fast}(\omega)$.

To account for the classical frozen modes, the nonequilibrium population dynamics takes the following form,

$$\langle\sigma_z(t)\rangle \approx \int d\mathbf{P}d\mathbf{Q}\ \rho_{\rm slow}(\mathbf{P},\mathbf{Q},0){\rm Tr}_{\rm sys+fast}[\rho_{\rm sys+fast}(t)\sigma_z], \tag{2.14}$$

where $\rho_{\rm slow}(\mathbf{P},\mathbf{Q},0)$ could be either the classical distribution function or the Wigner transform of the equilibrium density operator of the slow bath degrees of freedom, and $\rho_{\rm sys+fast}(t)$ is the reduced density matrix of the system and the fast bath degrees of freedom. Observables such as ${\rm Tr}_{\rm sys+fast}[\rho_{\rm sys+fast}(t)\sigma_z]$ may then be calculated via the Redfield equations.

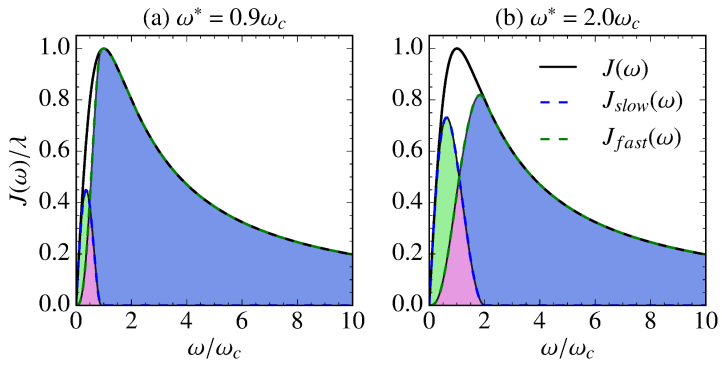

Figure 2.1: Spectral density and splitting via $S(\omega, \omega^*)$, illustrating the two situations expressed in Eqs. (2.10) and (2.11).

To understand the relaxation processes with mode freezing for finite ω^*, it is first useful to investigate the effect of the approximation at its most extreme, namely the adiabatic limit, where all bath modes are assumed to be static ($\omega^* \to \infty$). In this limit, we are effectively in the Born-Oppenheimer regime, where excitations in the electronic subspace move along the potential energy surface determined by the frozen reservoir. Analytical evaluation of the trace within Eq. (2.14) leads to the following expression for the nonequilibrium population dynamics,

$$\langle \sigma_z(t) \rangle \approx \int d\mathbf{P} d\mathbf{Q}\ \rho_{\rm bath}(\mathbf{P}, \mathbf{Q}, 0)\ \frac{\tilde{\varepsilon}^2 + \Delta^2 \cos(\xi t)}{\tilde{\varepsilon}^2 + \Delta^2}, \tag{2.15}$$

where $\xi = 2\sqrt{\tilde{\varepsilon}^2 + \Delta^2}$ is the Rabi frequency of the modified system Hamiltonian. The integration over the ensemble of equilibrium configurations of the bath reduces to averaging over different values of $\lambda^{cl}(0)$ that are consistent with the bath distribution function. For some realizations of the bath, Eq. (2.15) recovers the Rabi oscillations characteristic of the isolated system if $\lambda^{cl}(0) = 0$. Conversely, when $\lambda^{cl}(0) \neq 0$, the population starts from 1 at

$t = 0$ and will oscillate between $(\tilde{\varepsilon}^2 + \Delta^2)/(\tilde{\varepsilon}^2 + \Delta^2) = 1$ and $(\tilde{\varepsilon}^2 - \Delta^2)/(\tilde{\varepsilon}^2 + \Delta^2)$. Taking for simplicity $\varepsilon = 0$, one notes that the lower bound of the population oscillations increases with increasing $\lambda^{cl}(0)$, approaching 1 as $\lambda^{cl}(0) \to \infty$. This limit corresponds to an infinitely rigid bath that completely localizes the excitation on its initial site.

Averaging over different realizations of the slow modes decreases the amplitude of oscillations in the population dynamics due to the decoherence between the functions with distinct oscillation frequencies. In general, Redfield theory has difficulty describing non-Markovian, multi-step relaxation dynamics. However, when $\lambda_{\text{slow}} = \pi^{-1} \int_0^\infty d\omega \; J_{\text{slow}}(\omega)/\omega$ is sufficiently large, the full dynamics produced by Redfield theory with frozen modes at finite ω^* will include both a slow, perhaps oscillatory component as well as a more rapid decay induced by the high frequency modes in $J_{\text{fast}}(\omega)$. These qualitative considerations suggest this approach may correct certain deficiencies of conventional Redfield-like approaches. In the next section, we test the approach quantitatively.

An additional concern regarding any approximate dynamical theory is whether it leads to the appropriate long-time limit. While the asymptotic behavior in the standard (time-local and time-nonlocal) Redfield equations can only be studied numerically, it is simple to show that Markovian Redfield theory within the secular approximation, where the populations and coherences (in the system's eigenbasis) are assumed to evolve independently of each other, obeys detailed balance with respect to the isolated system [110]. In this case, one may write the long-time limit of the RDM as $\lim_{t\to\infty} \rho_{\text{sys}}(t) = e^{-\beta H_{\text{sys}}}/\text{Tr}_{\text{sys}}[e^{-\beta H_{\text{sys}}}]$, which is only correct in the weak system-bath coupling limit.. Making the analogous approximations for the Redfield-FM approach, calculation of the long-time limit of system observables requires tracing over the appropriate operator and averaging over the static disorder imposed by the

arrested modes. Hence, the equilibrium value of the population difference in the diabatic basis takes the form,

$$\lim_{t\to\infty}\langle\sigma_z(t)\rangle = -\int d\mathbf{P}d\mathbf{Q}\ \rho_{\text{slow}}(\mathbf{P},\mathbf{Q},0)\frac{\tilde{\varepsilon}}{\tilde{\xi}}\tanh(\beta\tilde{\xi}), \tag{2.16}$$

where $\tilde{\xi} = \sqrt{\tilde{\varepsilon}(\mathbf{Q})^2 + \Delta^2}$ is the (positive) eigen-energy of the isolated system for each realization of the environmental disorder. In the case of an unbiased system ($\varepsilon = 0$), the integrand in the above expression is odd with respect to $\mathbf{Q}$, leading to $\langle\sigma_z(t \to \infty)\rangle = 0$, agreeing with the result obtained via the Markovian secular Redfield approach. The two methods yield different results for biased cases, $\varepsilon \neq 0$. While the current discussion of detailed balance is strictly applicable only to Markovian Redfield-FM under the secular approximation, the result in Eq. 2.16 should serve as an approximate guide to the long-time limit of the populations in the Redfield-FM scheme presented here.[3] In this regard, it should be noted that the long-time behavior exhibited by the Redfield-FM approach appears to be in better agreement with exact results than is standard Redfield theory.

Finally we remark that, while the idea of dynamically arrested modes has been used in various contexts leading to much notable work, our approach exploits this idea in a novel way. Previous implementations of this idea have ranged from a partial freezing of the modes, as in the case of electron transfer in proteins [111], to complete arrest of the enviroment, leading to the Gaussian Disorder Model for studying charge carrier mobility in disordered organic semiconductors [112]. As with the two examples cited above, other

[3]The secular approximation is valid for cases where the eigen-energy of the isolated system is large, $\xi = \sqrt{\varepsilon^2 + \Delta^2} >> 1$. Consequently, factors that maximize the modified eigen-energy in the Redfield-FM approach, $\tilde{\xi} = \sqrt{(\varepsilon + \lambda^{cl})^2 + \Delta^2}$, such as a large bias ε or large reorganization energy λ and splitting frequency ω^*, lead to secular-like evolution of the populations and coherences (on average). For these cases, one can expect the long-time limit of the Redfield-FM dynamics to closely approach the limit defined by Eq. 2.16.

uses of the mode-freezing approximation (to the best of the authors' knowledge) have been concerned with the modification of incoherent, classical transfer rates of excitations among sites. In contrast, we employ the partial arrest of the bath in conjunction with a fully quantum mechanical treatment to obtain real-time dynamics that account for both *coherent* and *incoherent* motion of the excitations.

2.3 Results

In the following, we compare the numerically exact population dynamics reported by Thoss *et al.* [28] for the SB model with a Debye spectral density and the initial condition $\Gamma(0) = |1\rangle\langle 1| \exp(-\beta H_{\mathrm{bath}})/Z_{\mathrm{bath}}$ with the results obtained from the Redfield-FM method. Subsequently, we examine the effect of relaxing the mode-freezing approximation by treating the low-frequency modes dynamically via the Ehrenfest method. We call this latter approach the hybrid-Redfield method, in analogy with the previously developed hybrid-NIBA method [109, 113].

Computational Details

To treat the frozen portion of the spectral density, $J_{\mathrm{slow}}(\omega)$, we have discretized the bath into $f = 300$ modes with frequencies and couplings given by [55, 109]

$$\omega_k = \omega_c \tan\left[\frac{\pi}{2f}(k - 1/2)\right], \tag{2.17}$$

and

$$c_k^2 = \frac{2\lambda}{f}\omega_k^2. \tag{2.18}$$

Initial conditions for the reservoir of frozen modes were sampled from a Wigner distribution. Sampling from this distribution becomes particularly important at very low temperatures, where quantum effects become significant. However, for most cases, sampling from a Boltzmann distribution is sufficient since the modes being samples are always low-frequency. For convergence, up to 10^4 trajectories have been run for the results presented.

Redfield-FM Method

As mentioned in Sec. 2.2, the validity of Redfield theory is limited to the small η regime. Fig. 2.2(a) shows the results for a slow bath ($\omega_c = 0.25$) with small reorganization energy ($\lambda = 0.25$) at low temperature ($\beta = 5.0$); here and in the following, all energies are in units of Δ. In spite of the slow bath, the dimensionless applicability parameter is only slightly larger than unity ($\eta = 1.6$) suggesting that Redfield theory should be reasonably accurate, in agreement with the numerical results. The Redfield-FM method provides an even better estimate of the dynamics, almost quantitatively correcting the already accurate Redfield dynamics.

Fig. 2.2(b) considers a biased system ($\varepsilon = 1.0$) with the same parameters, except at much higher temperature ($\beta = 0.5$), yielding an applicability parameter which is now significantly larger than unity ($\eta = 16$). Here, it is evident that the Redfield dynamics relax far too quickly, suppressing the coherence and missing the slower relaxation process revealed by the exact dynamics. The improvement afforded by the Redfield-FM method compared to standard Redfield theory is clear. In particular, the Redfield-FM approach accurately reproduces the short- to intermediate-time dynamics, the frequency of the oscillations, and the initial rate of decoherence. The terminal decay rate is slightly underestimated due to

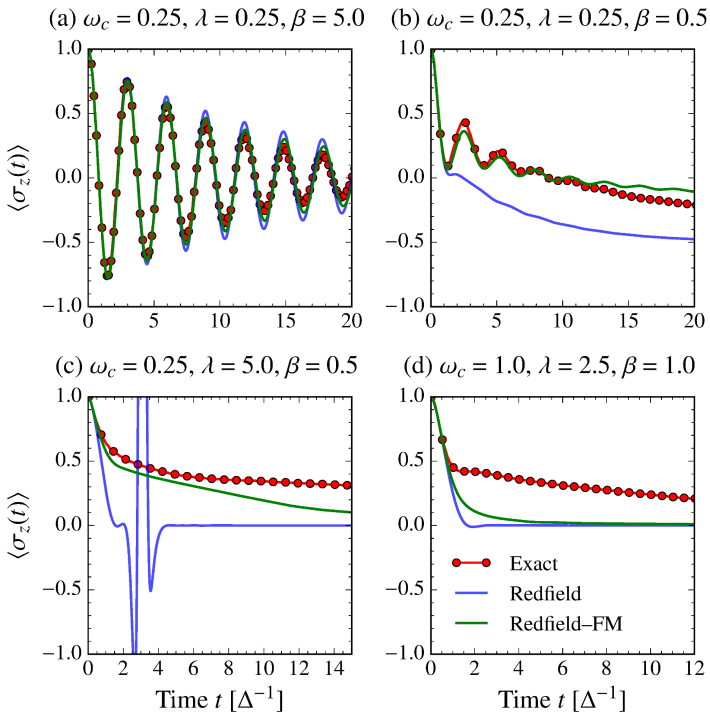

Figure 2.2: Results from Redfield-FM approach compared with standard time-local Redfield theory and exact numerics. $\omega^* = \max[\omega_c, \frac{\omega_R}{4}]$ and $\omega_R = 2\sqrt{\Delta^2 + \epsilon^2}$. All units are scaled by the electronic coupling Δ. All panels correspond to unbiased cases ($\varepsilon = 0$), except for panel (b), where $\varepsilon = 1.0$. Other parameters are stated in the panels.

the mode-freezing approximation, as discussed in Section II.B. Yet despite these shortcomings, the improvement derived from a simple scheme like the Redfield-FM approach with the numerical complexity of the original Redfield theory is noteworthy.

For cases exemplified by Fig. 2.2(c), serious problems such as the violation of the positivity of the RDM dynamics can occur within standard (non-secular) Redfield theory. Figure 2.2(c) corresponds to a slow bath ($\omega_c = 0.25$) and a large reorganization energy ($\lambda = 5.0$) again at high temperature ($\beta = 0.5$), for which the applicability parameter is very large ($\eta = 320$). Despite the evident failure of the Redfield equations to even maintain positivity, the Redfield-FM method is able to correct the positivity issue and almost quantitatively reproduce the two-step relaxation process in the exact dynamics up to intermediate times.

It is possible to understand the surprising success presented in Fig. 2.2(c) in the context of the analysis of Section II.B. Using the definitions given in that section, the effective parameters for the Redfield equation are $\lambda_{\text{fast}} = 2.5$, $\omega_c = 0.5$, yielding $\eta = 40$. Although $\eta \gg 1$, the reduction by an order of magnitude from the initial value, $\eta = 320$, is sizeable, and likely responsible for solving the positivity problem evident in the bare Redfield dynamics. The reproduction of the two-step relaxation process is a direct result of the trapping effect that arises from freezing a large portion of the low-frequency bath in the presence of large coupling. This example indicates that the trapping effect can partially reproduce slow relaxation dynamics associated with strong system-bath interactions.

Figure 2.2(d) shows the regime of intermediate bath speeds ($\omega_c = 1$), large reorganization energy ($\lambda = 2.5$), and intermediate temperature ($\beta = 1$). In contrast to Fig. 2.2(c), the Redfield-FM method is not capable of significantly improving the Redfield dynamics in this regime, missing the two-step relaxation process visible in the exact dynamics. In light of the

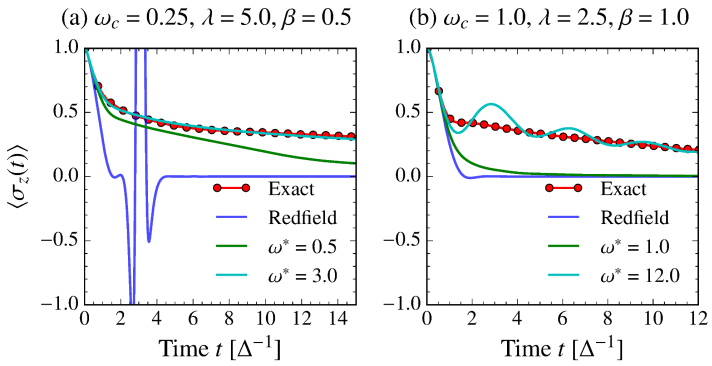

Figure 2.3: Redfield-FM results for $\omega^* = \max[\omega_c, \frac{\omega_R}{4}]$ and an "optimized" value for ω^*. Both cases considered here correspond to $\varepsilon = 0$ and all units are scaled by the electronic coupling, Δ. Note that the set of parameters for panels (a) and (b) in this figure correspond to the set of parameters in Fig. 2.2, panels (c) and (d), respectively.

previous case, it is evident that the slowing down of the RDM dynamics can be caused by freezing a large portion of the strongly coupled modes, an effect which is absent in this case. In this case, $\lambda_{\text{fast}} = 2.1$ and $\lambda_{\text{slow}} = 0.4$, which indicates that most of the reorganization energy is included already in the high-frequency portion of the bath. In such cases, the Redfield-FM method will yield results that are similar to bare Redfield theory.

We now address the dependence of the dynamics on the choice of ω^*. Eschewing the simple criteria for choosing ω^* presented above, one may ask how closely the Redfield-FM dynamics can be made to agree with exact dynamics when ω^* is allowed to vary. To address this question, we include two extreme cases in Fig. 2.3. First, Fig. 2.3(a), which corresponds to the same parameters as those of Fig. 2.2(c), shows that optimization of ω^* can result in *quantitative* agreement between the Redfield-FM result and the exact dynamics.

Such agreement may be understood as the result of fortuitous cooperation between strongly dissipative Redfield dynamics that damp the frozen mode-generated oscillations and the trapping effect from the mode-freezing approximation that prevents immediate relaxation to the equilibrium population. Conversely, Fig. 2.3(b), which corresponds to the parameters in Fig. 2.2(d), is an example of when perfect agreement is impossible. Clearly, attempts at optimizing ω^* result in better agreement of the two-step relaxation process at the cost of long-lived oscillations, a direct result of including a large fraction of modes into the slow part of the bath. In freezing a sufficiently large portion of the reservoir to reproduce the trapping effect, λ_{fast} is reduced to the point where the Redfield dynamics are no longer sufficiently dissipative to damp the frozen mode-generated oscillations. In addition, $\lambda_{\text{slow}} = \pi^{-1} \int_0^\infty d\omega J_{\text{slow}}(\omega)/\omega$ is also not large enough to ensure that the oscillations dephase sufficiently rapidly. Overall, it is clear that although it may be possible to optimize the results, the simple initial criteria presented represent a robust approach to frozen mode dynamics that essentially always yields results that are as good or better than bare Redfield dynamics without a significantly increased computational cost.

Application to Multi-Site Models: FMO Complex

While the SB model serves as a simple yet nontrivial model to test of the performance of new approximate dynamical theories, the usefulness of a method also largely lies in its applicability to multi-site systems where numerically exact methods become difficult to perform. Generalization of the Redfield-FM approach to multi-site systems is straightforward. To illustrate this, we focus on the theoretically [17] and experimentally [114] well characterized example of the Fenna-Matthews-Olson (FMO) complex.

Within the standard FMO model, the total Hamiltonian takes the form, $H = H_{\rm sys} + H_{\rm bath} + V$, where

$$H_{\rm sys} = \sum_{i=1}^{7} E_i \left|i\right\rangle \left\langle i\right| + \sum_{i\neq j}^{7} J_{ij} \left|i\right\rangle \left\langle j\right|, \tag{2.19}$$

with parameters E_i and J_{ij} taken from Ref. [16]. The bath Hamiltonian consists of independent reservoirs for each chromophore,

$$H_{\rm bath} = \sum_{i}^{7} \sum_{k} \left|i\right\rangle \left[\frac{1}{2}P_{i,k}^2 + \frac{1}{2}\omega_{i,k}^2 Q_{i,k}^2\right] \left\langle i\right|. \tag{2.20}$$

The system-bath coupling is bilinear, same as in the SB model,

$$V = \sum_{i=1}^{7} \sum_{k} \left|i\right\rangle c_{i,k} Q_{i,k} \left\langle i\right|, \tag{2.21}$$

where $c_{i,k}$ is the coupling constant between the i^{th} site and the k^{th} mode in the local bath.

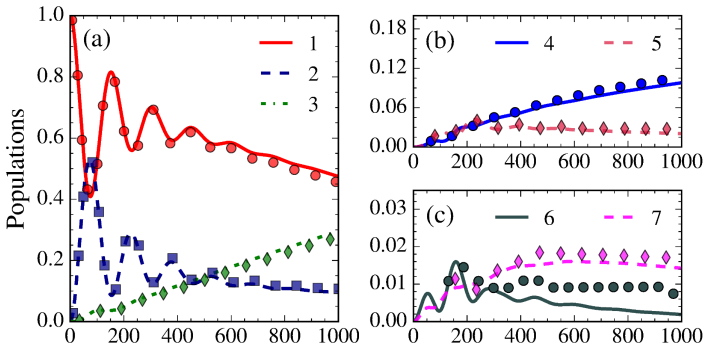

Figure 2.4: Population dynamics for the FMO complex at $T = 70$ K, with $\tau_c = 50$ fs and an initial electronic excitation on site 1. The shapes (circles, squares, and diamonds) correspond to the numerically exact results computed via the HEOM method [17] and the lines (solid, dashed, and dash-dotted) to the standard time-local Redfield results.

All local baths are assumed to be equivalent, characterized by Debye spectral densities, with $\lambda = 35$ cm^{-1}.

To define the splitting frequencies that generalize our previous choice, one first defines a set of "Rabi" frequencies associated with each pair of sites, $\{\omega_{R,ij}\}$, where $\omega_{R,ij} = 2\sqrt{(E_i - E_j)^2 + J_{ij}^2}$. The splitting frequency for each bath is then taken, as before, as $\omega_i^* = \max[\omega_{c,i},\ \max[\omega_{R,ij}]/4]$. As we will demonstrate, despite the fact that this definition is essentially unaltered from that used to treat the two-site cases, the results are in remarkable agreement with exact calculations for more complex multi-site examples.

Althouth Redfield theory has been criticized for its inability to recover the correct dynamics in prototypical electronic energy transfer systems where intrasystem and system-bath couplings are comparable [24], its performance for the FMO model is surprisingly good as long as temperature is low and the bath relaxation timescale is short. This is in harmony with the discussion contained in Sec. 2.2. In Fig. 2.4, we consider one such favorable case, corresponding to a fast bath with correlation time $\tau_c = 50$ fs ($\omega_c = \tau_c^{-1}$) and low temperature, $T = 70$ K. As is clear from the figure, the Redfield equations recover the dynamics quantitatively, including the correct oscillation frequency, amplitude, and long-time limit for all but sites 6 and 7. Fig. 2.5 corresponds to the case of high temperature ($T = 300$ K) and sluggish baths with correlation time $\tau_c = 166$ fs. Here the parameter η is significantly larger, rendering this a much more difficult parameter regime for the Redfield approach, which overestimates the decoherence and leads to incorrect behavior in the long-time limit for all but one of the site populations. The Redfield-FM approach corrects the dynamics quantitatively, alleviating the difficulties associated with a sluggish bath.

The examples presented here clearly illustrate the ingredients that determine the success

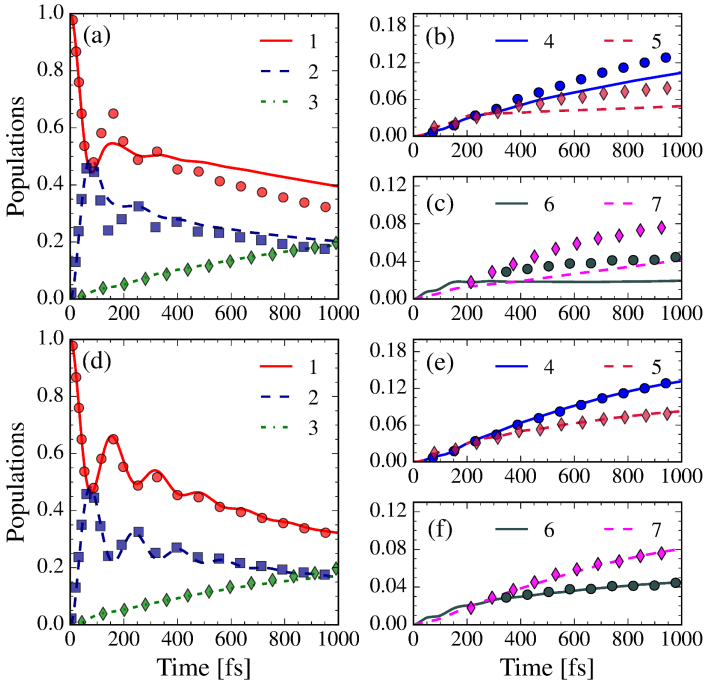

Figure 2.5: Population dynamics for the FMO complex at $T = 300$ K, with $\tau_c = 166$ fs and an initial electronic excitation on site 1. Shapes (circles, squares, and diamonds) correspond to numerically exact (HEOM) dynamics [17]. Panels (a)–(c) compare the exact dynamics to the dynamics obtained via the time-local Redfield equations (solid, dashed, and dash-dotted lines). Panels (d)–(f) provide a comparison to Redfield-FM results (solid, dashed, and dash-dotted lines). For the Redfield-FM dynamics, the splitting frequency for the i^{th} bath is taken to be $\omega_i^* = \max[\omega_{c,i}, \max[\omega_{R,ij}/4]]$.

or failure of standard Redfield theory. In contrast to the pervasive claim that Redield theory should fail when the reorganization energy exceeds the intersite couplings, we have shown in Fig. 2.4 that as long as the temperature is relatively low and the bath responds rapidly,

Redfield theory can be quantitative even in the "intermediate" coupling regime. On the other hand, when the parameter η becomes large, in particular in cases when the bath is sluggish, the Redfield-FM approach quantitatively corrects standard Redfield theory. The fact that this is the case for multi-site examples with no adjustment to the criteria for choosing ω^* lends credence to the robustness of the Redfield-FM methodology.

Relaxing the Mode-Freezing Approximation: A Dynamical Hybrid Redfield Method

On first inspection, the mode-freezing approximation appears extreme. To thoroughly assess its effect, we develop a dynamical hybrid method in which we evolve the previously frozen low-frequency modes in $J_{\text{slow}}(\omega)$ via classical Ehrenfest dynamics. The derivation and the implementation details of this approach may be found in Appendix 2.C.

This hybrid-Redfield method is similar in spirit to the successful hybrid-NIBA developed and implemented in Ref. [109]. Evolution of the low-frequency modes using Ehrenfest dynamics in such hybrid approaches only requires two assumptions: (i) that $\Gamma(t) \approx \rho_{\text{slow}}(t)\rho_{\text{sys+fast}}(t)$, and (ii) that the motion of the low-frequency modes is well-captured by classical mechanics. For such a factorization to be valid, the reorganization energy due to the low-frequency bath needs to be small, i.e., $\lambda_{\text{slow}} = \pi^{-1}\int_0^\infty d\omega\, J_{\text{slow}}(\omega)/\omega < \Delta$. The applicability of classical dynamics relies on the low energies of the reservoir modes and sufficiently high temperatures that help suppress quantum effects [62, 109]. However, even when the Ehrenfest approximation is valid, problems may arise. Most prominent among these is that the final populations approach those of the infinite-temperature limit [62].

In contrast to the Hamiltonian derived under the mode-freezing approximation in Eq. (2.13), the modified Hamiltonian that needs to be treated via the Redfield equation in the hybrid-Redfield method is time-dependent,

$$H''(t) = [\varepsilon + \lambda^{cl}(t)]\sigma_z + \Delta\sigma_x + \sigma_z \sum_{k\in\text{fast}} c_k Q_k + \frac{1}{2}\sum_k \left[P_k^2 + \omega_k^2 Q_k^2\right], \tag{2.22}$$

where the disorder due to the low frequency bath is no longer static as it is in the Redfield-FM method, but rather dynamic, namely $\lambda^{cl}(t) = \sum_k c_k Q_k(t)$.

Since the system part of this Hamiltonian is nondiagonal and time-dependent, evolution with respect to the system Hamiltonian requires diagonalization at every time-step, significantly increasing the computational cost associated with the method proposed here. The need to evolve the low-frequency bath also adds to the computational cost of the approach. Importantly, under the mode-freezing approximation, we circumvent these costly requirements. This means that, aside from the trivial cost of parallelization for the ensemble averaging over the slow bath, the Redfield-FM method scales as gracefully with system size as the original Redfield equation.

For completeness, we remark that the nonequilibrium population dynamics under the hybrid-Redfield approximation now take the form

$$\langle\sigma_z(t)\rangle \approx \int d\mathbf{P}d\mathbf{Q}\ \rho_{\text{slow}}(\mathbf{P},\mathbf{Q},t)\text{Tr}_{\text{sys+fast}}[\rho_{\text{sys+fast}}(t)\sigma_z]. \tag{2.23}$$

Fig. 2.4 shows two sets of parameters for which the hybrid-Redfield scheme yields results that illustrate the issues at play in comparing the hybrid-Redfield approach to the Redfield-FM method. Extensive testing of the hybrid method suggests that an approximately optimal form for the splitting frequency can be taken as

$$\omega_{hy}^* = \omega_R\lambda/\omega_c. \tag{2.24}$$

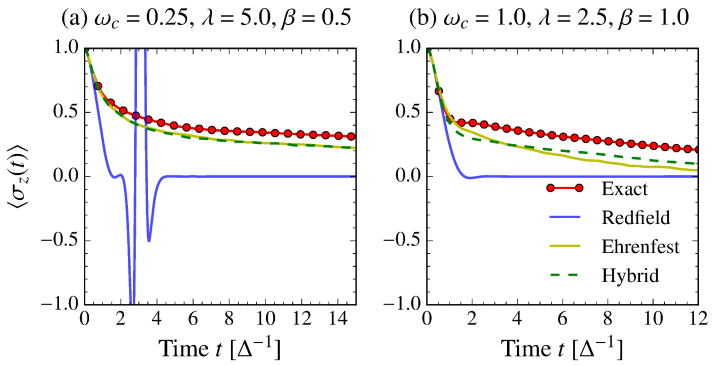

Figure 2.6: Hybrid-Redfield results for $\omega^*_{hy} = \omega_R \frac{\lambda}{\omega_c}$. Both cases considered here correspond to $\varepsilon = 0$ and all units are scaled by the electronic coupling, Δ. Similar to Fig. 2.3, the set of parameters for panels (a) and (b) in this figure correspond to the set of parameters in Fig. 2.2, panels (c) and (d), respectively.

Physically, this form encodes the interplay between the Redfield and Ehrenfest methods, favoring a larger portion of the modes to be treated classically with increasing Rabi frequency ω_R, which is a measure of how rapidly the electronic system evolves. Furthermore, this form of ω^* ensures that in the limit of small λ and large ω_c, the hybrid method correctly reproduces the more appropriate Redfield dynamics, whereas in the limit of large λ and small ω_c, it reproduces the Ehrenfest results. It is expected that generally nontrivial results may be obtained from this method for cases where $\omega^* \sim \omega_c$, as is the case for the choice of ω^* used in the Redfield-FM approach.

Fig. 2.6(a) corresponds to the parameters in Fig. 2.2(c) and illustrates that, by means of the suggested form for ω^*, hybrid-Redfield automatically tunes itself to yield nearly optimal results achievable from the two parent methods. This example, for which $\omega^*_{hy} \gg \omega_c$,

illustrates that the hybrid-Redfield method trivially reproduces the Ehrenfest result when it is appropriate. *It is noteworthy that the Redfield-FM method obtains similar agreement at a much lower computational cost* without evolving the reservoir modes, indicating that dynamic treatment of these modes may not be generally necessary. Indeed, it is rather remarkable that the Redfield-FM approach basically recapitulates the Ehrenfest results even though no Ehrenfest dynamics are used.

Fig. 2.6(b) shows the analogue of Fig. 2.2(d), where the Redfield-FM method fails to correct the Redfield dynamics. In contrast, the hybrid-Redfield results are in very good agreement with the exact dynamics. Indeed, the hybrid method is able to qualitatively and almost quantitatively reproduce the shape of the two-step relaxation process evident in the exact dynamics, an effect that both Ehrenfest and Redfield dynamics independently miss.

As the above considerations indicate, there are cases where the dynamical hybrid-Redifeld method can provide a substantial improvement over the Redfield-FM method, albeit at a much higher computational cost. In most regions of parameter space we have studied, however, we find that hybrid-Redfield theory offers little accuracy gain over the Redfield-FM approach. Thus, the benefits of the hybrid-Redfield approach compared to the Redfield-FM method do not justify its use when accuracy and cost are factored together.

2.4 Conclusions

In this work, we have presented a new scheme for simulating dynamics in quantum dissipative systems. Our approach, which we call the Redfield-FM method, recognizes that standard Redfield theory becomes inaccurate for slow bath degrees of freedom. By partitioning the

bath into high- and low-frequency components, we propose solving the Redfield equations for the high-frequency partition in the statically disordered field of the low-frequency components. Such an approach may greatly increase the accuracy of Redfield theory in highly non-Markovian regimes at essentially the same computational cost. In addition, we find that this simple approach can fundamentally cure positivity problems associated with standard non-secular Redfield theory. The straightforward generalization of the Redfield-FM method to multi-site models and its application to the FMO complex have proven efficient and highly successful, underlining the method's capacity to tackle problems of significant complexity. We have further discussed a scheme (the hybrid-Redfield approach) whereby the previously frozen degrees of freedom are instead evolved with classical Ehrenfest dynamics. While this method can improve upon the dynamics as described by the Redfield-FM approach, the increase in accuracy is incremental and comes at a significantly larger computational cost. Overall, while the Redfield-FM method does not cure all of the ills of Redfield theory, it does provide a simple and efficient framework for improving its accuracy and range of validity, especially for sluggish bath degrees of freedom such as those implicated in biological energy transfer.

Appendix

2.A Derivation of Redfield equations

Here, for completeness, we review the derivation of the Redfield equations. For a more detailed discussion of Redfield theory, we refer the reader to Refs. [80] and [115].

In the following development we utilize a projection operator technique to derive an equation of motion for the reduced density matrix (RDM) of the system, defined as $\rho(t) = \mathrm{Tr}_{\mathrm{bath}}[\Gamma(t)]$, where $\Gamma(t) = e^{-iHt}\Gamma(0)e^{iHt}$ and $\Gamma(0)$ is the initial density matrix of the full system and bath. Moreover, we assume that the initial condition for the (total) density matrix contains no system-bath correlation, such that $\Gamma(0) = \rho(0)\rho_{\mathrm{bath}}$, where $\rho(0)$ is an arbitrary Hermitian system operator, $\rho_{\mathrm{bath}} = e^{-\beta H_{\mathrm{bath}}}/Z$, $Z = \mathrm{Tr}_{\mathrm{bath}}[e^{-\beta H_{\mathrm{bath}}}]$ and $\beta = 1/k_B T$ is the thermal energy. Treatment of general initial conditions is also possible via the projection operator technique at the expense of the introduction of additional inhomogeneous terms in Eq. (2.5) [116–118]. In the following, we ignore initial correlations, but note that their inclusion in the present framework is straightforward.

We start from the Liouville equation for the full density matrix in the interaction picture where the total Hamiltonian is divided into a zeroth order part and an interaction part,

$H = H_0 + H_1$, such that

$$\frac{d}{dt}\Gamma_I(t) = -i\mathcal{L}_I(t)\Gamma_I(t), \tag{2.25}$$

$\Gamma_I(t) = e^{iH_0t}\Gamma(t)e^{-iH_0t}$ and $\mathcal{L}_I(t) = [e^{-iH_0t}H_1e^{iH_0t}, ...]$. To obtain the dynamics of the RDM, we define a projection operator of form $\mathcal{P} \equiv \rho_{\text{bath}}\text{Tr}_{\text{bath}}[...]$ with $Q \equiv 1 - \mathcal{P}$. We note that action of $\mathcal{P}$ on the full density matrix followed by trace over the bath results in the RDM in the interaction picture, $\rho_I(t) = \text{Tr}_{\text{bath}}[\mathcal{P}\Gamma_I(t)]$. Using these definitions, we obtain the following exact equations of motion,

$$\frac{d}{dt}\mathcal{P}\Gamma_I(t) = -i\mathcal{P}\mathcal{L}_I(t)(\mathcal{P} + \mathcal{Q})\Gamma_I(t) \tag{2.26}$$

$$\frac{d}{dt}\mathcal{Q}\Gamma_I(t) = -i\mathcal{Q}\mathcal{L}_I(t)(\mathcal{P} + \mathcal{Q})\Gamma_I(t). \tag{2.27}$$

Formal integration of Eq. (2.26) yields

$$\mathcal{Q}\Gamma_I(t) = -i\int_0^t d\tau\ g(t,\tau)\mathcal{Q}\mathcal{L}_I(t)\mathcal{P}\Gamma_I(\tau), \tag{2.28}$$

where $g(t,\tau) = \exp_+[-i\int_\tau^t ds\ \mathcal{Q}\mathcal{L}_I(s)]$ and the time ordering $(+)$ implies that time arguments increase from right to left. Substitution of this expression in Eq. (2.25) results in the Nakajima-Zwanzig equation [116, 117], which is expressed in terms of the time convolution of a memory term with $\rho_I(t)$ at earlier times as

$$\frac{d}{dt}\rho_I(t) = -\int_0^t d\tau\ K(t-\tau)\rho_I(\tau), \tag{2.29}$$

where $K(t-\tau) = \text{Tr}_{\text{bath}}[\mathcal{L}_I(t)g(t,\tau)\mathcal{Q}\mathcal{L}_I(\tau)\rho_{\text{bath}}]$ is the (time-nonlocal) memory function.

If, instead, we use the formal solution of Eq. (2.25) to evolve $\Gamma_I(t)$ backwards in time to an earlier time τ, we obtain

$$\Gamma_I(\tau) = G(t,\tau)\Gamma_I(t), \tag{2.30}$$

where $G(t,\tau) = \exp_-[i\int_\tau^t ds\mathcal{L}_I(s)]$ and the time ordering $(-)$ requires that time arguments increase from left to right. Replacing this expression in Eq. (2.28) and solving for $\mathcal{Q}\Gamma_I(t)$ yields

$$\mathcal{Q}\Gamma_I(t) = [1-\Sigma(t)]^{-1}\Sigma(t)\mathcal{P}\Gamma_I(t), \tag{2.31}$$

where

$$\Sigma(t) = -i\int_0^t d\tau\ g(t,\tau)\mathcal{Q}\mathcal{L}(\tau)\mathcal{P}G(t,\tau). \tag{2.32}$$

We note that a crucial requirement for the validity of this derivation is the existence of $[1-\Sigma(t)]^{-1}$.

Substitution of Eq. (2.31) into Eq. (2.26) and subsequent trace over the bath degrees of freedom results in the following time-local equation of motion for the RDM [118],

$$\frac{d}{dt}\rho_I(t) = R(t)\rho(t), \tag{2.33}$$

where $R(t) = -i\mathrm{Tr}_{\mathrm{bath}}[\mathcal{L}_I(t)[1-\Sigma(t)]^{-1}\rho_{\mathrm{bath}}]$ is the (time-local) rate function.

The expression for the dynamical evolution in either the time-nonlocal (Eq. (2.29)) or time-local (Eq. (2.33)) form is exact but prohibitively difficult to evaluate without resorting to approximation schemes, such as truncated generalized cumulant expansions. Perturbative expansion to second order in the system-bath coupling (where $H_1 = V$ from Eq. (2.3)) results in a non-Markovian generalization of the Redfield theory. Alternatively, one may derive both forms of the Redfield equations via resummations of differently time-ordered cumulants [119, 120]. These derivations explicitly show that both forms of generalized Redfield theory account for non-Markovian behavior and have similar applicability requirements [120–122]. Specifically, since Redfield theory is tantamount to second-order perturbation theory in the system-bath coupling, truncation at low order is only accurate for $\eta < 1$, where $\eta =$

$\max[\frac{2\lambda}{\beta\omega_c^2}, \frac{2\lambda}{\pi\omega_c}]$ is the validity parameter introduced in Sec. 2.2. Despite this restriction, the Redfield equations have been shown to perform surprisingly well, often beyond the small-λ and large-ω_c regimes [123, 124]. Nevertheless, for inappropriate regions of parameter space, severe problems can arise, such as violation of positivity in the reduced density matrix [107].

2.B Markovian Redfield theory with Frozen Modes

We wish to consider the performance of the frozen modes method for a strictly Markovian version of Redfield theory, i.e. with a rate tensor $R = R(t \to \infty)$. In this limit, the time integrals become Fourier-Laplace transforms, such that the Redfield tensor elements can be expressed algebraically in terms of the spectral density $J(\omega)$ evaluated at energy differences $\hbar\omega_{ij} \equiv (E_i - E_j)$ [24, 110]. More specifically, we are interested in the dephasing terms of the Redfield tensor, which in general contain an elastic contribution

$$R_{ijij} \sim g_{ij}^2 \; J(\omega = 0+) \; n_{BE}(\omega = 0+). \tag{2.34}$$

At low frequencies, the Bose-Einstein distribution, $n_{BE}(\omega) \sim kT/\omega$, such that for a spectral density of the form $J(\omega) \sim \omega^s$, we find

$$R_{ijij} \sim kT\omega^{s-1}\Big|_{\omega=0}. \tag{2.35}$$

For all 'super-Ohmic' spectral densities with $s > 1$, this elastic contribution to the dephasing rate vanishes. However, for an Ohmic spectral density with $s = 1$ there is a pure dephasing rate which vanishes only at $T = 0$. This contribution to the dephasing rate in the system's eigenbasis can significantly affect both the population and coherence dynamics in the original basis of the problem.

We now return to the idea of a frozen modes variant of Markovian Redfield theory. Consider specifically an Ohmic spectral density with any non-zero splitting frequency ω^*. After partitioning, the fast spectral density has the low-frequency behavior $J_{\text{fast}}(\omega) \sim \omega^s$ with $s > 1$, which yields no elastic contribution to the dephasing rate. For this reason, a frozen modes version of Markovian Redfield theory does not reduce to the Redfield limit until the singular point $\omega^* = 0$. Instead, as $\omega^* \to 0$, the result approach a Redfield result which neglects the Ohmic pure dephasing rate. We emphasize that the time-dependent variants of Redfield theory are not signficantly affected by this problem until very long times, and that all methods are only affected for strictly Ohmic spectral densities.

We propose a very simple solution to this pathological behavior in Markovian Redfield theory, by modifying the fast spectral density via

$$J_{\text{fast}}(\omega) = [1 - S(\omega, \omega^*)]J(\omega) + \ W(\omega, \epsilon)J(\omega), \tag{2.36}$$

where $W(\omega, \epsilon)$ is a rectangular window function centered at the origin with width ϵ, and ϵ should be chosen very small. In this way, the 'fast' part of the bath will always produce a pure dephasing rate for arbitrary splitting frequency ω^*. Thus, the Markovian Redfield-FM dynamics will smoothly interpolate towards the standard Markovian Redfield result as ω^* approaches zero. In Fig. 2.B.1, we compare the results of standard Markovian Redfield, Markovian Redfield-FM without this dephasing correction, and Markovian Redfield-FM with the correction. Results are presented for the model excitonic dimer discussed by Ishizaki and Fleming [24]. Importantly, we find that this correction typically improves the results of the Markovian Redfield-FM variant, quite significantly in cases of strong system-bath coupling.

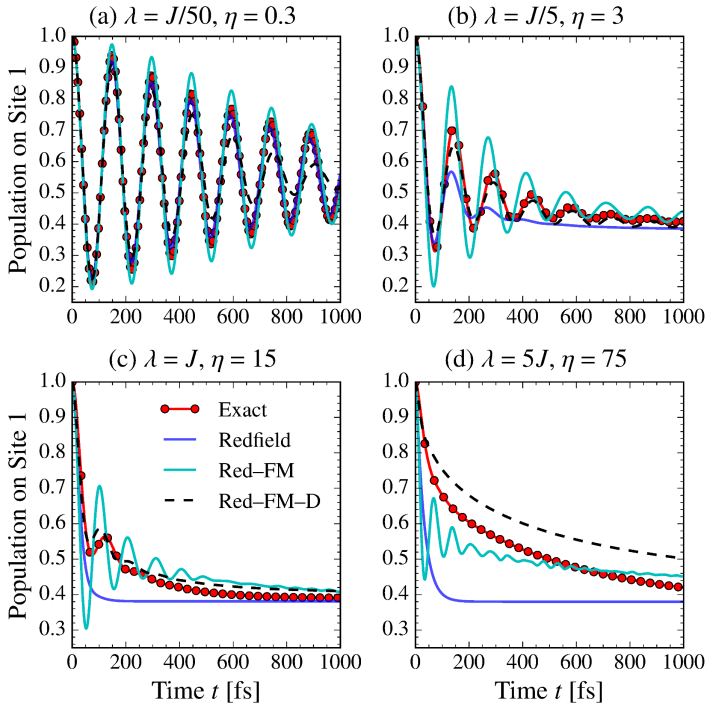

Figure 2.B.1: Comparison of numerically exact (HEOM) population dynamics to the results of standard Markovian Redfield theory, a straightforward variant of Markovian Redfield theory with frozen modes (Red-FM), and a dephasing-corrected variant as discussed in the text (Red-FM-D). The system-bath Hamiltonian is that of Ref. [24] with $\varepsilon = 100$ cm^{-1}, $J = 100$ cm^{-1}, $\omega_c^{-1} = 100$ fs, and $T = 300$ K.

2.C RDM Hybrid Method

Here we relax the mode-freezing approximation by deriving a fully hybrid method that separates the complete system into a slow part consisting of the low-frequency component of the bath, and a rapidly-evolving part that includes both the electronic system and the high-frequency portion of the phonon bath. In this hybrid scheme, the slow part is treated quasi-classically, while the fast part is treated at the level of Redfield theory. Overall, the fast (slow) component of the system evolves in the mean field of the slow (fast) one.

Other hybrid approaches that combine classical and quantum dynamics include the self-consistent hybrid method of Wang and coworkers [27, 28], which yields numerically exact dynamics, and the approximate hybrid-NIBA approach of Refs. [109, 113] In the former method, ω^*, which is the energy scale that determines the splitting of the bath into slow and fast parts, is strictly a convergence parameter. In the latter, ω^* is an empirically determined adjustable parameter. As an approximate method, the hybrid-Redfield scheme derived here is akin to the hybrid-NIBA method. For a more detailed discussion of the hybrid RDM method, we refer the reader to Ref. [109].

As in the Redfield-FM approach, we make the approximation that $\Gamma(t) \approx \rho_{\rm slow}\rho_{\rm sys+fast}(t)$, where $\rho_{\rm sys+fast}(t)$ is the density matrix for the system and fast bath degrees of freedom and $\rho_{\rm slow}(t)$ is the density matrix for the slow bath degrees of freedom. The system and fast bath modes obey the following effective Liouville equation,

$$\frac{d\rho_{\rm sys+fast}(t)}{dt} = -i[H''(t), \rho_{\rm sys+fast}(t)], \tag{2.37}$$

where

$$H''(t) = [\varepsilon + \lambda^{cl}(t)]\sigma_z + \Delta\sigma_x + \sigma_z \sum_{k\in\text{fast}} c_k Q_k + \frac{1}{2}\sum_k \Big[P_k^2 + \omega_k^2 Q_k^2\Big], \tag{2.38}$$

and λ^{cl} is a dynamically fluctuating bias, $\lambda^{cl}(t) = \sum_{k\in\text{slow}} c_k Q_k(t)$.

A classical treatment of the reservoir leads to the following equations of motion,

$$\frac{dQ_k}{dt} = P_k, \tag{2.39}$$

and

$$\frac{dP_k}{dt} = -\omega_k^2 Q_k - c_k\tilde{\sigma}_z(t). \tag{2.40}$$

Employing the Ehrenfest approach demands that each part of the system evolves in the mean field of the other. For the quantum portion, the classical mean field consists of the time-dependent contribution to the bias, $\lambda^{cl}(t)$. For the classical portion, the force term $-c_k\tilde{\sigma}_z(t) = -c_k\text{Tr}_{\text{sys+fast}}[\sigma_z\rho_{\text{sys+fast}}(t)]$ in the equations of motion embodies the mean-field 'back-reaction.' This force term moves the classical oscillators from the ground state minima to the displaced minima associated with the excited state.

Using Eqs. (2.5) and (2.38), the time-local Redfield equation takes the form

$$\begin{aligned}\frac{d}{dt}\rho(t) = &-i[H''_{\text{sys}}(t), \rho(t)] \\ &- \int_0^t ds\, \Big\{C(s)[\sigma_z, \sigma_z(-s)\rho(t)] - C^*(s)[\sigma_z, \rho(t)\sigma_z(-s)]\Big\},\end{aligned} \tag{2.41}$$

where $\sigma_z(t) = U_0^\dagger(t)\sigma_z U_0(t)$, $U_0(t) = \exp_+[-i\int_0^t d\tau\ H''_{\text{sys}}(\tau)]$, and $H''_{\text{sys}}(t) = [\varepsilon + \lambda^{cl}(t)]\sigma_z + \Delta\sigma_x + \sum_{k\in\text{slow}}[P_k^2 + \omega_k^2 Q_k^2]/2$. The bath correlation, as in the case of the Redfield-FM method, takes the following form,

$$C(t) = \frac{1}{\pi}\int_0^\infty d\omega\ J_{\text{fast}}(\omega)[\coth(\beta\omega/2)\cos(\omega t) - i\sin(\omega t)]. \tag{2.42}$$

To obtain the results shown in Fig. 2.3, trajectories corresponding to a set of initial conditions sampled from the Wigner distribution [125] were calculated via a second-order Runge-Kutta scheme, using a step size of $\delta t = 0.01\Delta^{-1}$. As required by the Runge-Kutta procedure, $\tilde{\sigma}_z(t)$ was kept constant during the evolution of the bath while $\lambda^{cl}(t)$ was kept constant during the evolution of the system. Explicitly, over a half-time step, the equations for the bath become

$$Q_k\left(t+\frac{\delta t}{2}\right) = \alpha_k(t)\cos\left(\frac{\omega_k\delta t}{2}\right) - \frac{c_k}{\omega_k^2}\tilde{\sigma}_z(t) + \frac{P_k(t)}{\omega_k}\cos\left(\frac{\omega_k\delta t}{2}\right), \tag{2.43}$$

and

$$P_k\left(t+\frac{\delta t}{2}\right) = P_k(t)\cos\left(\frac{\omega_k\delta t}{2}\right) + \omega_k\alpha_k(t)\sin\left(\frac{\omega_k\delta t}{2}\right), \tag{2.44}$$

where

$$\alpha_k(t) = Q_k(t) + \frac{c_k}{\omega_k^2}\tilde{\sigma}_z(t). \tag{2.45}$$

In the hybrid-NIBA method of Ref. [109] the zeroth-order propagator necessary to evolve the perturbation in the interaction picture, $U_0(t) = \exp[-i\int_0^\infty d\tau H''_{\rm sys}(\tau)]$, was simple to calculate since $H''_{\rm sys}$ was diagonal. In contrast, $H''_{\rm sys}(t)$ for hybrid-Redfield contains off-diagonal elements. Within the Runge-Kutta scheme, this obstacle is easy to overcome, though it requires diagonalization of the time dependent $H''_{\rm sys}(t)$ at every time step. Because numerical diagonalization at every time-step is necessary for systems with more than two degrees of freedom, this can become computationally expensive for sufficiently large systems.

Chapter 3

Approximate but Accurate Quantum Dynamics from the Mori Formalism: I. Nonequilibrium Dynamics[1]

3.1 Introduction

The continued effort to develop accurate and efficient approaches for the calculation of the dynamics of many-body quantum systems has produced a rich variety of methods, ranging from the numerically exact to the approximate. While exact methods provide important benchmark results for model systems [18, 20, 21, 24–28], their computational cost makes them impractical for realistic multidimensional systems. Conversely, approximate methods,

[1]Based on work published in J. Chem. Phys. **144**, 184104 (2016). Copyright 2016, American Institute of Physics.

whether perturbative [1, 42, 43] or based on quasi- [61–64, 126] or semi-classical [44–48, 66, 67] approaches, tend to scale more gracefully with system size and can address both model and realistic systems, albeit at the expense of general applicability and accuracy. For cases where one is interested in the dynamics of a limited number of degrees of freedom, the Nakajima-Zwanzig (NZ) equation [127, 128] provides a useful starting point for a plethora of methods based on generalized quantum master equations (GQME).

The NZ equation, which may be derived via the projection operator technique [129, 130], dictates the evolution of the reduced density matrix (RDM) for the portion of the Hilbert space denoted as the system. The influence of the complementary subspace, referred to as the bath, on the RDM dynamics appears in the form of a memory term, full knowledge of which is tantamount to solving the original problem. The apparent simplicity of the NZ equation, however, belies the complexity of the memory term, which can be formidably difficult if not impossible to calculate exactly. Despite the seeming conservation of difficulty, different treatments of the memory kernel have led to manageable and often very successful approximate and numerically exact schemes [1, 23, 42, 43, 131, 132].

A major difficulty in the calculation of the memory kernel lies in the fact that its dynamical evolution involves the "projected" propagator, $e^{i(1-\mathcal{P})\mathcal{L}t}$, where $\mathcal{P}$ is the projector that defines the reduced dynamics. To circumvent the problem of projected dynamics, Shi and Geva [93, 94, 100] proposed a self-consistent expansion of the memory kernel, which requires the calculation of auxiliary kernels evolved with the *normal* rather than the *projected* propagator. From an exact perspective, this approach is useful only if the numerical effort necessary for the calculation of the auxiliary kernels is less than that required for the direct calculation of the system dynamics. Using the numerically exact quasi-adiabatic path

integral (QUAPI) method [20, 21], Shi and Geva have shown that the memory kernel for the spin-boson model can decay up to 10 times faster than the system dynamics [93], lending credence to the feasibility of the self-consistent approach. More recently, a similar scheme has been used by Rabani and co-workers within a path integral framework for the study of quantum transport problems [95–99]. Just as importantly, applications of the method have successfully used semi- and quasi-classical theories to calculate the auxiliary kernels [100]. In particular, Kelly, Markland, and coworkers have illustrated the impressive accuracy and robustness of this approach in both model and realistic problems [101–103]. These studies have led to two important conclusions: (i) the memory kernels are short-lived in a wide region of parameter space for canonical problems such as the spin-boson model and (ii) the self-consistent solution of the memory kernel using approximate dynamics can yield impressively more accurate results than *direct* simulation of the RDM dynamics using the very same approximate method.

Despite these important results, questions of general applicability still remain. For instance, the conditions that lead to short-lived memory kernels remain unknown. Further, it is still unclear how the breakdown of approximate methods (in unfavorable parameter regimes) affects the quality of the self-consistently extracted memory function. Perhaps most importantly, an understanding of the necessary and sufficient conditions that lead to improvements in accuracy of approximate dynamics via the memory function formalism, as observed in Refs. [100–103], is lacking. Finally, the convergence properties of different versions of the auxiliary kernels arising from the alternative closures in the self-consistent expansion of the memory function have not yet been explored. We expect these convergence properties to differ when approximate methods are employed in the calculation of the

auxiliary kernels.

The remarkable utility of the NZ equation notwithstanding, objects beyond single-time nonequilibrium dynamics are cumbersome to obtain within this framework. Despite this difficulty, recent work has generalized the NZ equation to multi-time correlation functions [133]. In contrast, the more flexible Mori formulation permits direct extension to multiple-time and equilibrium correlation functions, which are essential in the treatment of linear [107] and non-linear spectroscopy [15], and the calculation of chemical rate constants [46, 134] and kinetic coefficients [4], to name a few examples. For this reason, in paper I (this paper) of this series, we provide a unified Mori-type framework to approach single-time nonequilibrium correlation functions, and address several of the open questions listed above. In a second paper, we present the a similar framework to treat equilibrium correlation functions. It should be noted that a major advantage of the Mori formulation is that it can naturally address problems where no system-bath distinction exists, such as spin and fermion lattice models [5–7], and quantum fluids [8, 9, 72, 135].

The structure of this paper is as follows: In Sec. 3.2, we present the formalism for nonequilibrium correlation functions from the Mori perspective and show that, with the appropriate choice of projection operator, one recovers equations identical to those arising from the conventional NZ treatment. Sec. 3.2 also introduces the spin-boson model and proposes two types of projection operators for this model. Sec. 3.3 discusses different closures of the memory kernel based on different placements of the projection operator $\mathcal{Q} = 1 - \mathcal{P}$ and the use of time derivatives. To illustrate the arguments related to convergence, we implement the mean field Ehrenfest method, as first proposed in Ref. [102], to obtain the auxiliary kernels. We henceforth refer to the use of the Ehrenfest method coupled to the

self-consistent extraction of the memory kernels as the GQME+MFT approach. In Sec. 3.4, we show the different properties of the memory kernels associated with the Redfield- and NIBA-type projectors, explore the performance of the GQME+MFT approach to SB models whose system-bath coupling is characterized by Ohmic and Debye spectral densities, and investigate the convergence properties of the distinct closures introduced in Sec. 3.3. In Sec. 3.5, we conclude.

3.2 Mori Approach

For illustrative purposes, we focus on the spin-boson (SB) Hamiltonian, which is representative of typical open quantum systems, but note that the current approach is general and may be applied to any Hamiltonian [2]. In particular, a major advantage of the Mori formalism developed here over the traditional NZ approach is the ability to treat systems with no natural system-bath separation, such as spin-chains and lattice models [5–7] and liquids [8, 9, 72, 135]. We reserve these applications for later work.

The SB Hamiltonian takes the form $H = H_S + H_B + V$. It contains a system part consisting of two sites offset by an energy bias 2ε and with off-diagonal coupling Δ, which is assumed to be independent of the bath coordinates,

$$H_S = \varepsilon\sigma_z + \Delta\sigma_x, \tag{3.1}$$

where σ_i corresponds to the i^{th} Pauli matrix. The bath part of the Hamiltonian consists of independent harmonic oscillators,

$$H_B = \frac{1}{2}\sum_k \left[\hat{P}_k^2 + \omega_k^2\hat{Q}_k^2\right], \tag{3.2}$$

where P_k and Q_k are the mass weighted momenta and coordinates for the k^{th} harmonic oscillator, respectively, and ω_k is the frequency of the k^{th} mode. The coupling between the system and bath is assumed to be linear in the bath coordinates and diagonal and antisymmetric with respect to the system basis,

$$V = \alpha\sigma_z \sum_k c_k \hat{Q}_k, \tag{3.3}$$

where c_k is the coupling constant between the system and the k^{th} oscillator, and $\alpha = \pm 1$, depending on the definition of the model. The spectral density, $J(\omega)$, fully characterizes the system-bath interaction, and takes the form,

$$J(\omega) = \alpha^2 \sum_k \frac{c_k^2}{2} \delta(\omega - \omega_k). \tag{3.4}$$

It is common to assume one of several forms for the spectral density. Two important cases describe Ohmic dissipation in condensed phase systems where $J(\omega)$ is proportional to ω as $\omega \to 0$. These are the standard Ohmic spectral density [1] characterized by an exponential cutoff, and the Debye spectral density characterized by a Lorentzian cutoff:

$$J_{Oh}(\omega) = \frac{\pi}{2} \xi \omega e^{-\omega/\omega_c}, \tag{3.5}$$

$$J_{De}(\omega) = 2\lambda\omega_c \, \frac{\omega}{\omega^2 + \omega_c^2}. \tag{3.6}$$

Here the cutoff frequency ω_c determines the correlation time of the bath at sufficiently high temperatures [136]. The reorganization energy, $\lambda = \pi^{-1} \int_0^\infty d\omega \; J(\omega)/\omega$, is a measure of the strength of the system-bath coupling. In the case of the Ohmic spectral density, the Kondo parameter, $\eta = \pi\xi/2 = \pi\lambda/\omega_c$, is often used instead to gauge the coupling strength.

To assess the applicability of the formalism presented here, we compare our results to exact nonequilibrium population dynamics of the SB model,

$$\langle \sigma_z(t) \rangle = \mathrm{Tr}[\sigma_z(t) \left|1\right\rangle \left\langle 1\right| \rho_B], \tag{3.7}$$

where $\rho_B = e^{-\beta H_B}/\mathrm{Tr}_B[e^{-\beta H_B}]$ is the equilibrium density operator for the uncoupled bath, $\beta = [k_B T]^{-1}$ is the inverse thermal energy, and the initial condition $\left|1\right\rangle \left\langle 1\right| \rho_B$ corresponds to a Frank-Condon transition.

Generalized Nakajima-Zwanzig-Mori Equation

Here, we deviate from the derivations commonly given for the NZ equation and the Mori equation of motion (EOM) for an operator and instead focus on a generalized EOM for the full propagator,

$$\frac{d}{dt} e^{i\mathcal{L}t} = i e^{i\mathcal{L}t} \mathcal{P}\mathcal{L} + i\mathcal{Q} e^{i\mathcal{L}\mathcal{Q}t}\mathcal{L} - \int_0^t d\tau \; e^{i\mathcal{L}(t-\tau)} \mathcal{P}\mathcal{L}\mathcal{Q} e^{i\mathcal{L}\mathcal{Q}\tau}\mathcal{L} \tag{3.8}$$

where $\mathcal{P}$ is the projection operator that defines the subsystem whose dynamics we seek and $\mathcal{Q} = 1 - \mathcal{P}$ is the complementary projection operator. This equation is general and can be employed within both the NZ and Mori approaches. For instance, applying Eq. (3.8) on an operator $\hat{A}$, yields the Mori EOM for that operator. Conversely, taking the Hermitian conjugate of Eq. (3.8), applying it on the initial density matrix of the system and bath, ρ_0, and acting the projection operator $\mathcal{P}$ from the left followed by a trace over the bath degrees of freedom yields the NZ equation for the system's RDM.

To date, essentially all work on the self-consistent expansion of the memory kernel has employed the thermal (Argyres-Kelley) projection operator $\mathcal{P} = \mathcal{R}_B \mathrm{Tr}_B[...]$ [93–97, 100–

102], where $\mathcal{R}_B$ is a bath operator with unit trace and $\mathrm{Tr}_B[...]$ corresponds to partial trace over the bath. To use the Mori formulation, it is convenient to rewrite the thermal projector, in the Heisenberg picture using Liouville notation,[2] as $\mathcal{P} = \sum_i |A_i\rangle\rangle\langle\langle \mathcal{R}_{Bi} A_i|$, where $\{A_i\}$ contains all outer product states spanning the system. For the spin-boson model, $A_i \in \{|1\rangle\langle 1|, |2\rangle\langle 1|, |1\rangle\langle 2|, |2\rangle\langle 2|\}$.

Using the thermal type projector, applying Eq. (3.8) to $|A_k\rangle\rangle$, and closing on the left with $\langle\langle \mathcal{R}'_{Bj} A_j|$, where $\mathcal{R}'_{Bj}$ is again a bath operator with unit trace that may be different from $\mathcal{R}_{Bj}$ in the projection operator, yields the following EOM for system observables,

$$\frac{d}{dt}\mathcal{C}(t) = i\mathcal{C}(t)\mathcal{X} + \mathcal{I}(t) - \int_0^t d\tau\ \mathcal{C}(t-\tau)\mathcal{K}(\tau), \tag{3.9}$$

where $\mathcal{X}_{jk} = \langle\langle \mathcal{R}_{Bj} A_j| \mathcal{L} |A_k\rangle\rangle$ is a static rotation matrix, $\mathcal{C}_{jk}(t) = \langle\langle \mathcal{R}'_{Bj} A_j| e^{i\mathcal{L}t} |A_k\rangle\rangle = \mathrm{Tr}[(\mathcal{R}'_{Bj})^\dagger A_j^\dagger A_k(t)]$ corresponds to nonequilibrium averages of populations and coherences with all possible factorizable initial conditions, and $\mathcal{I}_{jk}(t) = i\langle\langle \mathcal{R}'_{Bj} A_j| \mathcal{Q} e^{i\mathcal{L}\mathcal{Q}t}\mathcal{L} |A_k\rangle\rangle$ is the so-called the inhomogeneous term. The elements of the memory kernel are given by,

$$\mathcal{K}_{jk}(t) = \langle\langle \mathcal{R}_{Bj} A_j| \mathcal{L}\mathcal{Q} e^{i\mathcal{Q}\mathcal{L}t}\mathcal{Q}\mathcal{L} |A_k\rangle\rangle. \tag{3.10}$$

When $\mathcal{R}'_{Bj} = \mathcal{R}_{Bj}$, the inhomogeneous term disappears, $\mathcal{I}(t) = 0$. Often, $\mathcal{R}_{Bj} = R_{Bj}/\mathrm{Tr}_B[R_{Bj}]$ is chosen such that $R_{Bj} \in \{e^{-\beta H_B}, e^{-\beta(H_B \pm \alpha \sum_k c_k \hat{Q}_k)}\}$, which correspond to the harmonic oscillator bath at equilibrium with the ground electronic state or with one of the two excited states, respectively. Initial conditions of the form $\rho(0) = \rho_S(0)\mathcal{R}_{Bi}$, where $\rho_S(0)$ is an arbitrary system operator and $\mathcal{R}_{Bi}$ is taken from the set above, correspond either to a Frank-Condon excitation where the bath is in the electronic ground state also called

[2]For an introduction to this notation, see Chapter 2 in Ref. [15]

the spectroscopic initial condition, or a charge transfer initial condition where the bath is in equilibrium with one of the excited states.

We henceforth refer to the thermal projector above with the additional restriction that $R_{Bi} = \exp[-\beta H_B]$ as Redfield-type [42, 43]. The reason for this name is that truncation of the memory kernel at second order in $\mathcal{Q}$ is equivalent to a second-order perturbative expansion of the memory kernel with respect to the system-bath coupling, which corresponds to Redfield theory [42, 43]. The choice for $R'_{B,i}$, however, remains flexible.

An important alternative for the projection operator consists of restricting the set $\{A_i\}$ to the system populations $B_i = |i\rangle\langle i|$, and choosing $R_{Bi} = \exp[-\beta(H_B + (-1)^{i+1}\alpha\sum_k c_k\hat{Q}_k)]$. When using this projection operator, a similar second-order truncation of the memory kernel with respect to $\mathcal{Q}$ leads to equations that are equivalent to the non-interacting blip approximation (NIBA), which is a second order expansion in the electronic coupling Δ as opposed to the system-bath coupling [1, 137]. Accordingly, we hereafter refer to this projector as NIBA-type. As in the case of the Redfield-type projector, the choice for $R'_{B,i}$ determines whether the inhomogeneous term is zero or finite.

3.3 Self-Consistent Expansions for $\mathcal{K}(t)$

As mentioned in Sec. 3.1, the main difficulty associated with the memory kernel, Eq. (3.10), is the presence of the projected propagator, $e^{i\mathcal{L}\mathcal{Q}t}$. To circumvent this problem, Shi and Geva

proposed the use of the Dyson identity,

$$e^{(A+B)t} = e^{At} + \int_0^t ds\ e^{As} B e^{(A+B)(t-s)} \tag{3.11}$$

$$= e^{At} + \int_0^t ds\ e^{(A+B)s} B e^{A(t-s)}, \tag{3.12}$$

yielding a self-consistent expansion of the memory kernel that only involves unprojected dynamics [93, 94]. Not surprisingly, Eq. (3.8) can also be derived using the Dyson identity, Eqs. (3.11) and (3.12). Despite considering only time-independent Hamiltonians in this work, extension of the formalism to time-dependent Hamiltonians is simple and only requires the time-ordered form for the propagators in Eqs. (3.11) and (3.12).

It is important to remark that in the literature different variants of the Dyson expansion have led to a menagerie of seemingly distinct expressions, which differ with respect to the number and type of auxiliary kernels employed [94]. When these distinct expressions are evaluated via exact methods, all expansions yield equivalent results, up to numerical errors. However, when the auxiliary kernels are computed via approximate methods, different expansions can lead to memory kernels with different properties. In the following, we show that there are only a limited number of kernel expansions and ways of expressing the auxiliary kernels that can yield numerically distinct approximate memory kernels from the self-consistent solution of the resulting integral equations.

Bare expansions: Backward and Forward $\mathcal{Q}$

Substitution of Eq. (3.11) into Eq. (3.10), where $A = i\mathcal{L}$ and $B = -i\mathcal{P}\mathcal{L}$, yields the following integral equation for the memory kernel,

$$\mathcal{K}(t) = \mathcal{K}^{(1)}(t) + \int_0^t d\tau\ \mathcal{K}^{(3b)}(t-\tau)\mathcal{K}(\tau), \tag{3.13}$$

where the superscript b refers to the placement of the $\mathcal{Q}$ in the projected propagator as "backward" with respect to the placement of the Liouvillian, i.e., $e^{i\mathcal{Q}\mathcal{L}t}$. The auxiliary kernels take the forms

$$[\mathcal{K}^{(1)}(t)]_{jk} = \langle\langle \mathcal{R}_{Bj} A_j |\, \mathcal{L}\mathcal{Q}e^{i\mathcal{L}t}\mathcal{Q}\mathcal{L}\,|A_k\rangle\rangle, \tag{3.14}$$

$$[\mathcal{K}^{(3b)}(t)]_{jk} = -i\ \langle\langle \mathcal{R}_{Bj} A_j |\, \mathcal{L}\mathcal{Q}e^{i\mathcal{L}t}\,|A_k\rangle\rangle. \tag{3.15}$$

A seemingly distinct type of closure that is commonly used in the literature involves a *third* auxiliary kernel. In Appendix 3.B, we show that the three-member expansions are equivalent to the two-member expansions given by Eqs. (3.13) and (3.16). We further note that the auxiliary kernels we obtain are equivalent to those used by others in the field [93, 101, 102].

A second set of closures makes use of the identity $e^{i\mathcal{Q}\mathcal{L}t}\mathcal{Q} = \mathcal{Q}e^{i\mathcal{L}\mathcal{Q}t}$. To indicate that the $\mathcal{Q}$ is to the right of the Liouvillian $\mathcal{L}$ in the propagator, we have used the superscript f (indicating a "forward" placement). Inserting the previous identity in Eq. (3.10) and expanding the projected propagator using the Dyson identity given by Eq. (3.12), with $A = i\mathcal{L}$ and $B = -i\mathcal{L}\mathcal{P}$, yields

$$\mathcal{K}(t) = \mathcal{K}^{(1)}(t) + \int_0^t d\tau\ \mathcal{K}(t-\tau)\mathcal{K}^{(3f)}(\tau). \tag{3.16}$$

We note that $\mathcal{K}^{(1)}(t)$ has the form given in Eq. (3.14), and $\mathcal{K}^{(3f)}(t)$ has the following form,

$$[\mathcal{K}^{(3f)}(t)]_{jk} = -i\ \langle\langle \mathcal{R}_{Bj} A_j |\, e^{i\mathcal{L}t} \mathcal{Q}\mathcal{L}\, | A_k \rangle\rangle. \tag{3.17}$$

It bears remarking that Eqs. (3.16) and (3.13) differ in the placement of $\mathcal{K}(t)$ under the integral and Eqs. (3.17) and (3.15) differ in whether $\mathcal{Q}\mathcal{L}$ or its Hermitian conjugate act on operators that require sampling only at $t = 0$ or at finite times. We further note that the auxiliary kernels given by Eqs. (3.14), (3.15) and (3.17) no longer require the use of projected dynamics and can be simulated directly.

Expansions using time-derivatives

Because the auxiliary kernels given by Eqs. (3.14), (3.15), and (3.17) require sampling of additional bath operators at $t = 0$ and at finite times, convergence of these functions, at least within the context of semi- and quasi-classical methods, necessitates the sampling of a larger number of bath realizations than for the direct simulation of $\mathcal{C}(t)$, making the initial step of the calculation more expensive, even if trivially parallelizable. To avoid this added complexity and expense, the expressions for the auxiliary kernels can be rewritten as time derivatives of simpler correlation functions, including $\mathcal{C}(t)$ itself. Indeed, this observation has been made in recent work [95–99, 138].

Here we focus on three types of auxiliary kernels that exploit different placements of the time-derivative. The first type replaces the Liouvillian acting on operators that require dynamic sampling and leaves the Liouvillian acting on the static parts intact. In this scheme,

$\mathcal{K}^{(3b)}(t)$ remains unchanged. The other auxiliary kernels may be expressed as follows,

$$\mathcal{K}_1^{(1)}(t) = \dot{\mathcal{K}}^{(3b)}(t) - i\mathcal{K}^{(3b)}(t)\mathcal{X}, \tag{3.18}$$

$$\mathcal{K}_1^{(3b)}(t) = \mathcal{K}^{(3b)}(t), \tag{3.19}$$

$$\mathcal{K}_1^{(3f)}(t) = -\dot{\mathcal{C}}(t) + i\mathcal{C}(t)\mathcal{X}. \tag{3.20}$$

The second type focuses on replacing the Liouvillian operating on static operators with the time derivative, yielding the following expressions,

$$\mathcal{K}_2^{(1)}(t) = \dot{\mathcal{K}}^{(3f)}(t) - i\mathcal{X}\mathcal{K}^{(3f)}(t), \tag{3.21}$$

$$\mathcal{K}_2^{(3b)}(t) = -\dot{\mathcal{C}}(t) + i\mathcal{X}\mathcal{C}(t), \tag{3.22}$$

$$\mathcal{K}_2^{(3f)}(t) = \mathcal{K}^{(3f)}(t). \tag{3.23}$$

The final type replaces all Liouvillians with time derivatives,

$$\mathcal{K}_3^{(1)}(t) = -\ddot{\mathcal{C}}(t) + i\{\dot{\mathcal{C}}(t), \mathcal{X}\} - \mathcal{X}\mathcal{C}(t)\mathcal{X}, \tag{3.24}$$

$$\mathcal{K}_3^{(3b)}(t) = \mathcal{K}_2^{(3b)}(t), \tag{3.25}$$

$$\mathcal{K}_3^{(3f)}(t) = \mathcal{K}_1^{(3f)}(t). \tag{3.26}$$

It should be noted that Eqs. (3.18)–(3.26) are exact identities in the context of exact quantum dynamics but *may yield different results when approximate quantum dynamics are employed.*

For clarity in the subsequent discussion, we henceforth refer to the different closures via abbreviations of the form $c(xy)$, where $x \in \{\text{f(orward)}, \text{b(ackward)}\}$, and $y \in \{0, 1, 2, 3\}$ where 0 denotes the bare expansion and 1, 2, 3 the three types of expansion in the present section. For example, the $cb2$ closure refers to the use of Eqs. (3.21) and (3.22) to solve for $\mathcal{K}(t)$ in Eq. (3.13).

3.4 Results

The recent success achieved in using semi- and quasi-classical schemes to calculate the auxiliary kernels required in the self-consistent extraction of memory kernels underscores the importance of understanding the properties of this program in more detail. Consequently, we employ a simple quasi-classical method, namely Ehrenfest dynamics [126, 139], to obtain the auxiliary kernels and study the performance of the Redfield- and NIBA-type projectors and of the different closures available for the kernels. The procedural steps we follow can be summarized as follows:

1. Calculate the various auxiliary kernels via a dynamical method of choice. Here, we use the approximate Ehrefest approach.

2. Solve Eqs. (3.13) or (3.16) iteratively until the relative error becomes negligible. We define the relative error, $R.E.$, as the maximum absolute difference between two subsequent iterations of the memory kernel in the self-consistent scheme, i.e., $R.E. = \max[\mathrm{abs}[\mathcal{K}_{\mathrm{n+1}}(\mathrm{t}) - \mathcal{K}_{\mathrm{n}}(\mathrm{t})]]$. Our threshold is 10^{-10}.

3. Numerically integrate Eq. (3.9) subject to the appropriate initial conditions. In the following we use a second-order Runge-Kutta algorithm.

The memory kernel decays to zero for large sections of parameter space for the SB and other impurity-type models.[3] We refer to the timescale that determines this decay as the

[3]We are currently exploring cases for which the memory kernel decays to zero very slowly or decays to a finite constant.

memory lifetime. As mentioned in the Introduction, the computational efficiency of the memory function approach depends sensitively on this lifetime.

When approximate methods, such as semi- and quasi-classical schemes, are used to calculate the auxiliary kernels, the extracted memory function can accrue errors that are expected to grow with increasing simulation time. Hence, the decay of the memory kernel may not be accurately captured by these methods. Previous applications of the memory function approach have implemented a cutoff time for the memory kernel, after which all its components are set to zero. Sensitivity of the results to this cutoff time will be discussed in Sec. 3.4. For all results showing only one GQME+MFT curve, the cutoff time, τ_c, was chosen at the point where the extracted $\mathcal{C}(t)$ dynamics reached a plateau of stability. Importantly, our implementation of the Ehrenfest method employs Wigner-transformed initial conditions and is exact at $t = 0$, and, as is characteristic of all methods stemming from the semiclassical hierarchy, decreases in accuracy for increasing simulation time [140]. For a more thorough discussion of the Ehrenfest method and its implementation for obtaining the auxiliary kernels, see Appendices 3.C and 3.D.

Projection Operators

In this section, we restrict our attention to the Ohmic spectral density, a model whose performance has already been studied extensively using the Redfield-type projection operator and closure scheme *cb*0 by Kelly, Brackbill, and Markland [102]. The purpose of this section is mainly to provide an analysis of the NIBA-type memory kernels and show the viability of the GQME+MFT approach using both the Redfield- and NIBA-type projectors. Here and in Sec. 3.4, we show results only for the *cb*1 closure, and postpone the discussion of the

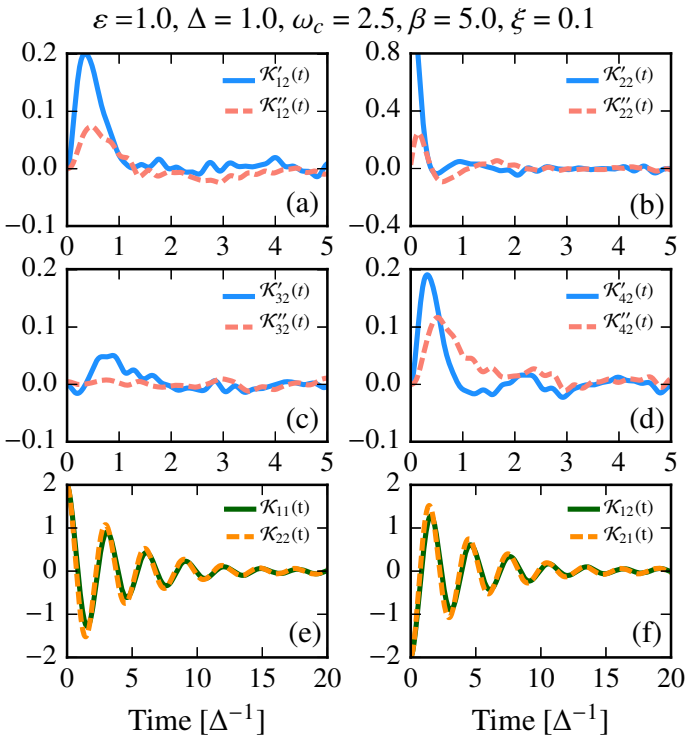

Figure 3.1: Redfield- and NIBA-type *cb*1 memory kernels for the SB model characterized by the Ohmic spectral density. Panels (a)-(d) correspond to the real (solid) and imaginary (dashed) parts of the Redfield-type memory kernel elements $\mathcal{K}_{x2}(t) = \mathcal{K}'_{x2}(t) + i\mathcal{K}''_{x2}(t)$. Panels (e)–(f) display *all* components of the NIBA-type memory kernel, $\mathcal{K}(t)$.

closure dependence of the results to Sec. 3.4.

We first compare the different properties of the Redfield- and NIBA-type memory kernels for a realization of the biased ($\varepsilon = 1$) spin-boson model characterized by weak system-bath coupling ($\xi = 0.1$), low temperature ($\beta = 5.0$), and a moderately fast bath ($\omega_c = 2.5$). Fig. 3.1 shows a representative set of components of the Redfield-type memory kernel, $\mathcal{K}_{x2}(t)$,

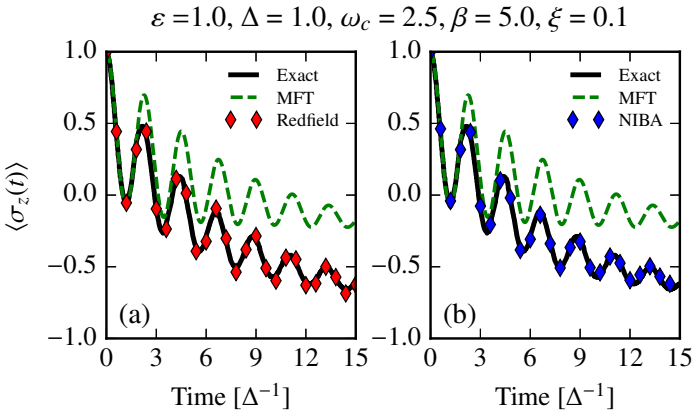

Figure 3.2: Population dynamics for the realization of the spin-boson model corresponding to the parameters in Fig. 3.1. Panel (a) compares the dynamics obtained from the Redfield-type memory kernel with a cutoff time $\tau_c = 2.0$ with the standard MFT and exact dynamics. Panel (b) provides a similar comparison with the dynamics obtained from the NIBA-type memory kernel, with a cutoff time of $\tau_c = 15$. Only results for the $cb1$ closure are shown. Exact results for the Ohmic SB model ($\alpha = -1$) are obtained from Ref. [102].

in panels (a)-(d), and all components of the NIBA-type memory kernel $\mathcal{K}(t)$ in panels (e)-(f). Comparison of the two types of memory kernel reveals the different timescales associated with their decay. Although seemingly noisy at longer times, the Redfield-type memory kernel has a short lifetime ($\tau_c \sim 2$), while the NIBA-type memory kernel decays much more slowly, ($\tau_c > 15$).

Fig. 3.2 illustrates the dynamics for the parameters used in Fig. 3.1. Despite capturing the correct oscillation frequency and amplitude decay, the Ehrenfest dynamics (green dashes) fails to capture the long-time limit of the populations. Indeed, because of the assumption of

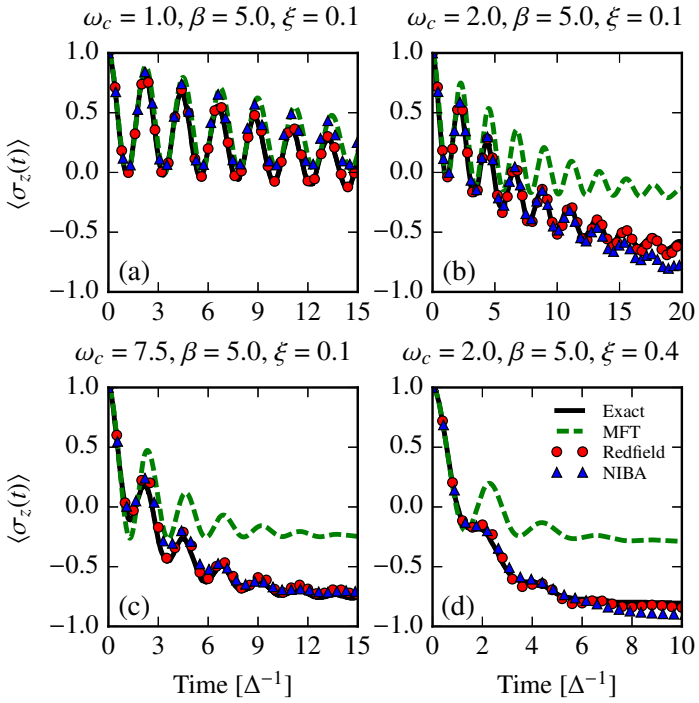

Figure 3.3: Population dynamics for four sets of parameters for the spin-boson model, assuming closure 1b. For all panels $\varepsilon = 1$ and all parameters are in units of Δ. The results shown correspond to the *cb*1 closure. Exact results are obtained from Ref. [102].

a classical bath, the Ehrenfest method is known to violate detailed balance [141]. Instead, the dynamics resulting from both the Redfield- and NIBA-type GQMEs with the *cb*1 closure quantitatively agree (to within graphical accuracy) with the exact results, showing that either method presented here is viable for recovering highly accurate dynamics from approximate dynamics.

To understand the difference in the lifetimes of the Redfield- and NIBA-type memory kernels we recall that the Mori approach to Brownian motion [142], which focuses on the

properties of a massive particle suspended in a bath of lighter particles, relies on the separation of timescales for the dynamics of the heavy and light particles. This separation of timescales is made effective via the projection operator, which must be chosen such that it contains all slow variables associated with the massive particle. Appropriate inclusion of all slow variables in the projector ensures that the memory kernel decays on a shorter timescale than the system dynamics [143]. The Redfield-type projector spans the entire Hilbert space of the system, whereas the NIBA-type projector excludes projections onto coherences, $|i\rangle \langle j|$ where $i \neq j$. While coherences often decay faster than populations, their decay is often slower than bath correlations, as long as the bath dimensionality is large. Hence, the slower time-scale associated with the decay of the coherences induces the slow decay of the NIBA-type memory kernels. This conclusion further suggests that the NIBA-type projector may be most useful in instances of fast system relaxation, such as strong system-bath coupling cases at high temperatures.

It has been suggested that the success of the memory function program, where the auxiliary kernels are calculated via semi- and quasi-classical schemes like Ehrenfest mean-field theory [102], the momentum-jump solution to the quantum-classical Liouville equation [101], and the linearized semiclassical initial value representation (LSC-IVR) scheme [144], relies primarily on the confluence of two important factors. First, the memory kernels are short-lived in comparison to the desired system dynamics. Second, approaches based on semi-classical arguments are more accurate at short times. Considered in tandem, these factors imply that the present scheme can lead to highly accurate short-time memory kernels, thus avoiding problems associated with the long-time dynamics produced by these approximate methods by virtue of fast memory decay. However, the ability of the slowly decaying NIBA-

type memory kernel to nearly recover the exact dynamics raises an important question: given the long lifetime of the NIBA-type kernel, how can it remain sufficiently accurate at long times to correct the long-time behavior of the bare quasi-classical dynamics? To answer this question, it is necessary to scrutinize the form of the auxiliary kernels. The NIBA-type auxiliary kernels for closure *cb*1 include two types of correlation functions, $q_{nm}^{(00)}(t)$ and $q_{nm}^{(10a)}(t)$ given by Eqs. (3.55) and (3.58). Clearly, $q_{nm}^{(00)}(t)$ is the Ehrenfest version of $\mathcal{C}(t)$, while $q_{nm}^{(10a)}(t)$ involves a new type of correlator that requires the sampling of an additional bath operator, $\zeta^W = -\alpha \sum_j c_j P_j \tanh(\beta\omega_j/2)/\omega_j$, at $t = 0$. At this point, two possible reasons for the improvement afforded by the NIBA-type approach seem likely. First, it may be that the Ehrenfest method describes the dynamics of coherences, which are required as input in the auxiliary kernels, better than those of populations. Second, $q_{nm}^{(10a)}(t)$ contains exact sampling of the bath operator ζ^W at $t = 0$, which may encapsulate important information about the system-bath interaction. With the information above, however, it is difficult to decide on which hypothesis is more likely. We return to this discussion in Sec. 3.4. The previous questions notwithstanding, the ability of the long-lived NIBA-type memory kernel to produce dynamics that are comparably accurate to those obtained via the Redfield-type approach underscores the fact that *a rapidly decaying memory function is not required for the success of the GQME+MFT approach.*

Fig. 3.3 provides a more thorough test of the performance of the NIBA-type projector. Here we compare the NIBA-type GQME+MFT dynamics to exact results for the cases addressed by Kelly *et al.* [102] in their recent work characterizing the performance of the Redfield-type GQME+MFT approach. For convenience, we include the results from the Redfield-type projector as well. The focus of these cases is the performance of the present

approach to biased systems coupled weakly ($\lambda = 2\xi/\omega_c < 1$) to a bath characterized by varying timescales, evident in the range of ω_c. As is clear from Fig. 3.3, direct use of the Ehrenfest MFT method consistently leads to incorrect long-time values of the population difference. In agreement with the work of Kelly and co-workers [102], the Redfield-type GQME+MFT method quantitatively corrects the dynamics in all cases considered. The NIBA-type approach generally provides clear improvement over direct use of MFT, but is slightly less accurate than the Redfield-type GQME+MFT. Regardless, the improvement of the dynamics produced by the NIBA-type projector is remarkable not just because of the fact that the memory function is long-lived, but also because such an approach is not tailored for the weak system-bath coupling limit as is the Redfield-type projector where the benchmark calculations of Fig. 3.3 have been performed.

Debye Spectral Density

Due to its slower decay at large frequencies, the Debye spectral density is generally considered a more challenging case for trajectory-based dynamical methods [109]. Here we show that the conclusions drawn from the Ohmic case, namely that the GQME+MFT method can significantly improve the problematic MFT dynamics for weakly coupled, biased systems at low temperatures, are similarly applicable to the Debye case. A few differences are worth mentioning, chief among them that the highly oscillatory nature of the Redfield-type memory kernels for this spectral density generally means that a larger number of trajectories to achieve convergence is required.

Panels (a)-(d) of Fig. 3.4 show the components $\mathcal{K}_{x2}(t)$ for the Redfield-type memory kernel, and panels (e)-(f) show all components of the NIBA-type memory kernel. While the

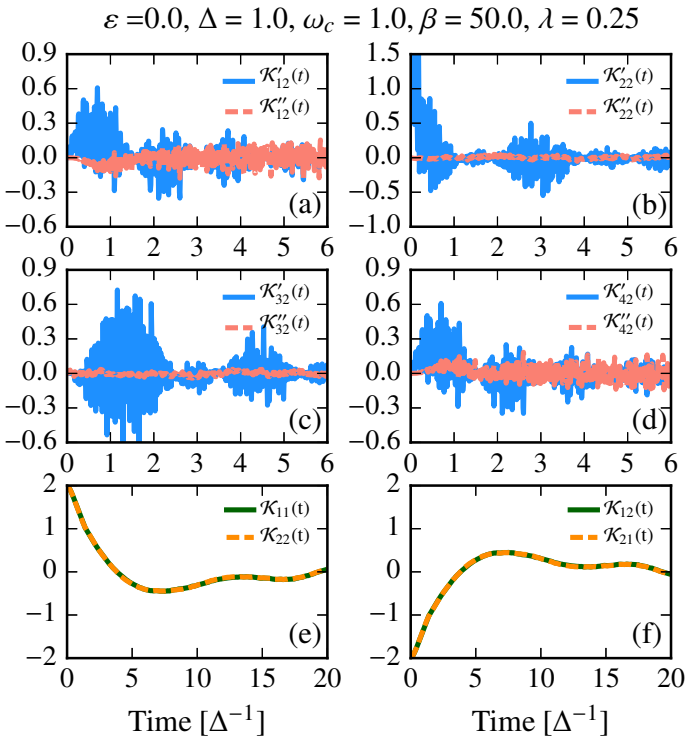

Figure 3.4: Redfield- and NIBA-type memory kernels using the *cb*1 closure for the unbiased SB model characterized by the Debye spectral density. Panels (a)–(d) correspond to the real (solid) and imaginary (dashed) parts of the Redfield-type memory kernel elements $\mathcal{K}_{x2}(t)$. Panels (e)-(f) display *all* components of the NIBA-type memory kernel.

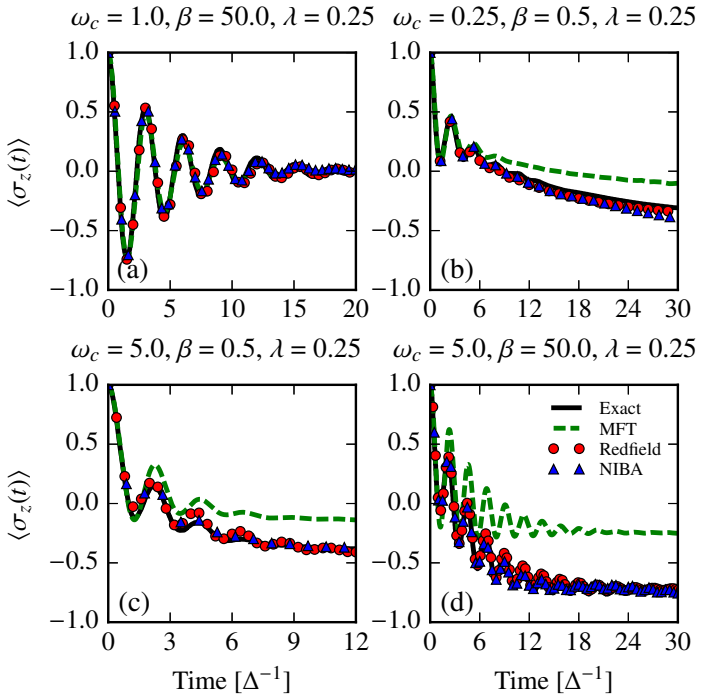

Figure 3.5: Population dynamics calculated from the $\mathcal{Q}$-forward closures of the memory kernel. For this set of parameters the $\mathcal{Q}$-backward closures yield equivalent results. The results shown correspond to the $cb1$ closure. Exact dynamics for the Debye SB model ($\alpha = 1$) are obtained from Ref. [28].

NIBA-type memory kernels do not show any obvious differences from their Ohmic counterparts, the Redfield-type memory kernel displays recurrent beating alongside overall decay. The presence of this much stronger oscillatory behavior requires that the dynamics of high frequency modes in the Ehrenfest procedure be treated more accurately than is necessary in the Ohmic case. We discuss this issue in more depth in the next section, where we explore the convergence properties of the difference closures.

Fig. 3.5 presents some illustrative examples of the capability of the GQME+MFT approach to yield accurate dynamics for the biased SB model at low temperatures, over a wide range of ω_c. Panel (a), which corresponds to an *unbiased* case characterized by weak system-bath coupling at low temperature ($\beta = 50.0$) and an intermediate bath frequency ($\omega_c = 1.0$), shows nearly perfect agreement between the Ehrenfest and exact dynamics. Both the Redfield- and NIBA-type GQME+MFT approaches are able to recover the remarkable agreement between the Ehrenfest and exact dynamics. Panels (b)-(d) correspond to biased cases, spanning a wide range of bath frequencies ($\omega_c = 0.25$, 5.0) and temperatures (β =0.5, 50.0). As expected, the bare Ehrenfest method leads to incorrect long-time limits for all three biased cases. As in the Ohmic case, both the Redfield- and NIBA-type approaches yield results in almost quantitative agreement with the exact dynamics. Slight deviations are evident, as in panel (b), where the NIBA-type GQME slightly underestimates the long-time limit of the population difference. Perhaps the most difficult case for the current approach, panel (d), shows that the NIBA-type GQME+MFT treatment leads to overly damped oscillations at long times, whereas the Redfield-type approach yields results in near quantitative agreement with the exact dynamics. In short, the results in Fig. 3.5 illustrate the robustness of the approach for weak-coupling cases over a wide range of bath frequencies and temperatures.

Memory Kernel Closures and Dynamics

In Sec. 3.3, we introduced *eight* different closures for the memory kernels. These include two subsets consisting of the $\mathcal{Q}$-forward and $\mathcal{Q}$-backward closures, which are further subdivided into the bare expansion ($cf0$ and $cb0$) and three expansions that use numerical time

derivatives of the simulated correlation functions, ($cf1$–$cf3$ and $cb1$–$cb3$). While the resulting dynamics do not differ when the auxiliary kernels are calculated via exact methods, the same claim is not necessarily true when using approximate dynamics. Here, we continue to use the Ehrenfest method to illustrate the sensitivity of the results that occur across the spectrum of closures.

To inform the discussion on the properties of different closures of either the Redfield- or NIBA-type memory kernels, we first provide an overview of the underlying types of correlation functions that are employed in the calculation of the auxiliary kernels. These are summarized in Eqs. (3.55)–(3.60) of Appendix 3.B. For convenience, we reproduce these expressions, within the Ehfenfest approximation, below,

$$q_{nm}^{(00)}(t) = \int d\Gamma\ \rho_B^W(0)\mathrm{Tr}_{\mathrm{sys}}[A_n^\dagger A_m(t)], \tag{3.27}$$

$$q_{nm}^{(01)}(t) = \int d\Gamma\ \rho_B^W(0)V_B^W(t)\mathrm{Tr}_{\mathrm{sys}}[A_n^\dagger A_m(t)], \tag{3.28}$$

$$q_{nm}^{(10s)}(t) = \int d\Gamma\ \rho_B^W(0)V_B^W(0)\mathrm{Tr}_{\mathrm{sys}}[A_n^\dagger A_m(t)], \tag{3.29}$$

$$q_{nm}^{(10a)}(t) = \int d\Gamma\ \rho_B^W(0)\zeta^W(0)\mathrm{Tr}_{\mathrm{sys}}[A_n^\dagger A_m(t)], \tag{3.30}$$

$$q_{nm}^{(11s)}(t) = \int d\Gamma\ \rho_B^W(0)V_B^W(0)V_B^W(t)\mathrm{Tr}_{\mathrm{sys}}[A_n^\dagger A_m(t)], \tag{3.31}$$

$$q_{nm}^{(11a)}(t) = \int d\Gamma\ \rho_B^W(0)\zeta^W(0)V_B^W(t)\mathrm{Tr}_{\mathrm{sys}}[A_n^\dagger A_m(t)], \tag{3.32}$$

where $V_B^W = \sum_k c_k x_k$ and $\zeta^W = -\alpha \sum_j c_j P_j \tanh(\beta\omega_j/2)/\omega_j$.

Inspection of Eqs. (3.27)–(3.32) reveals that there are two main types of functions containing bath operators: those that require their sampling exclusively at $t = 0$ [Eqs. (3.27), (3.29) and (3.30)], and those containing both statically and dynamically sampled bath operators [Eq. (3.28), (3.31), and (3.32)]. We recall the important fact that at $t = 0$, the Ehrenfest

method is exact and the accuracy of the method diminishes with increasing simulation time [140]. What is not clear, however, is whether the accuracy associated with the *dynamical* sampling of a single system operator is the same as that of a product of system and bath operators, as is required in Eqs. (3.28), (3.31), and (3.32). Because the bath is treated classically, dynamical sampling of bath operators may indeed accrue larger errors. Since the classical approximation is most problematic for high frequency modes, this problem may be exacerbated by fast baths characterized by broad spectral densities, namely the Debye spectral density. Instead, when bath operators are sampled statically, as is the case in Eqs. (3.27), (3.29), and (3.30), the $t = 0$ weighting of trajectories of the correlation functions is captured exactly. One may also distinguish the correlation functions above on the basis of sampling of *distinct* bath operators not normally included, whether explicitly or implicitly, in $\mathcal{C}(t)$. Naively, one may suppose that Eqs. (3.28)–(3.32) contain information distinct from that in contained in $\mathcal{C}(t)$, but the Ehrenfest evolution algorithm requires sampling of $V_B^W(t)$, which contributes a dynamic component to the system's bias energy $\varepsilon \mapsto \varepsilon + V_B^W(t)$. Consequently, only Eqs. (3.30) and (3.32), which sample ζ^W, contain *distinct* information about the system which is not already included in the calculation of $\mathcal{C}(t)$. Indeed, these correlation functions may contain additional information about the system-bath interaction via the statically sampled bath operator, ζ^W, that facilitates the improvement over the bare Ehrenfest dynamics afforded by the memory function approach.

A distinct source of error that may affect the accuracy of closures that implement numerical time-derivatives lies in the accuracy of the time-derivatives themselves. If the correlation functions calculated via the Ehrenfest procedure are sufficiently smooth and well converged and the time-step is sufficiently small, this error can be expected to be minimal. However,

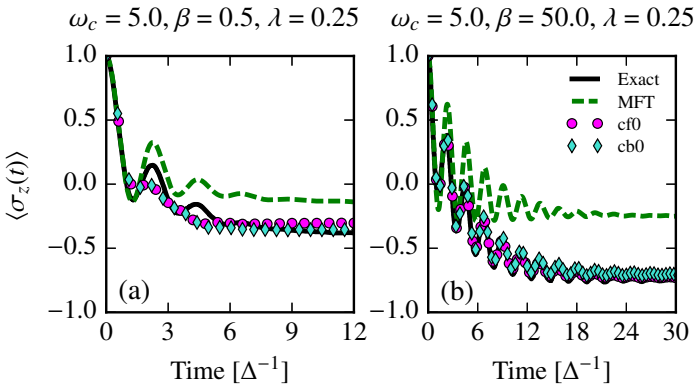

Figure 3.6: Comparison of the dynamics resulting from the $\mathcal{Q}$-forward and $\mathcal{Q}$-backward $cf0$ (fuschia dots) and $cb0$ (blue diamonds) closures for the Redfield-type memory kernel. Exact results are obtained from Ref. [28].

correlation functions containing bath operators that require sampling at finite times tend to be highly oscillatory, especially for fast baths, which may lead to less accurate results.

Armed with these considerations, it is possible to explore the differences associated with the different closures of the auxiliary kernels. Because the Redfield- and the NIBA-type projectors require different combinations of the aforementioned correlators, Eqs. (3.27)–(3.32), as input for their auxiliary kernels, we discuss the behaviors of the different closures for the two projectors separately.

Focusing first on the Redfield-type kernel closures, we assess the effect of the $\mathcal{Q}$-backward and $\mathcal{Q}$-forward approaches by focusing first on the $cb0$ and $cf0$ closures. Inspection of Eqs. (3.15) and (3.17) reveals that the only difference between the $\mathcal{Q}$-forward and $\mathcal{Q}$-backward closures lies in the fact that $\mathcal{K}^{(3f)}(t)$ contains the time-evolved bath operator $V_B^W(t)$, whereas $\mathcal{K}^{(3b)}(t)$ requires sampling of the static bath operator, $V_B^W(0)$ (see also

Eqs. (3.62)–(3.64)). Consistent with the above discussion, we may expect that the $cf0$ closure will lead to less accurate results than $cb0$. As Fig. 3.6 shows, the difference between the two closures is minimal. To understand the smallness of the difference between these two closures, it is sufficient to consider that, while each closure has a different form for $\mathcal{K}^{(3)}(t)$, both closures share the same form for $\mathcal{K}^{(1)}(t)$, which requires the sampling of bath operators both at $t = 0$ and at finite times. Hence, any error associated with the explicit inclusion of time evolved bath operators would affect both closures, $cb0$ and $cf0$, and any benefit derived from the exclusive sampling of $t = 0$ bath operators is also maintained in the form for $\mathcal{K}^{(1)}(t)$. Further, the similarity in performance of the $cb0$ and $cf0$ closures indicates that the error associated with the dynamical sampling of products of system and bath operators is often similar to the error associated with the exclusive sampling of system operators. Because the difference between the results of the $\mathcal{Q}$-forward and $\mathcal{Q}$-backward closures is small, we henceforth exclusively address the differences among the $\mathcal{Q}$-backward closures, $cb0$, $cb1$, $cb2$, and $cb3$.

Consideration of the remaining three $\mathcal{Q}$-backward closures, $cb1$, $cb2$, and $cb3$, likewise requires close scrutiny of the types of correlation functions that are used in each. First we note that, while the form of $\mathcal{K}^{(3b)}(t)$ in the $cb0$ closure avoids the sampling of bath operators at finite time, $\mathcal{K}^{(1)}(t)$ still samples bath operators at finite times. Instead, the $cb1$ closure completely avoids the sampling of bath operators at $t \neq 0$, while still benefiting from sampling of static bath operators for both auxiliary kernels. In contrast, the $cb2$ and $cb3$ closures explicitly avoid sampling of static bath operators, other than the density operator for the bath. As is evident from panels (a) and (b) in Fig. 3.7, the $cb1$ closure performs as well or better than the $cb0$ closure. However, because *the $cb1$ closure leads to equations*

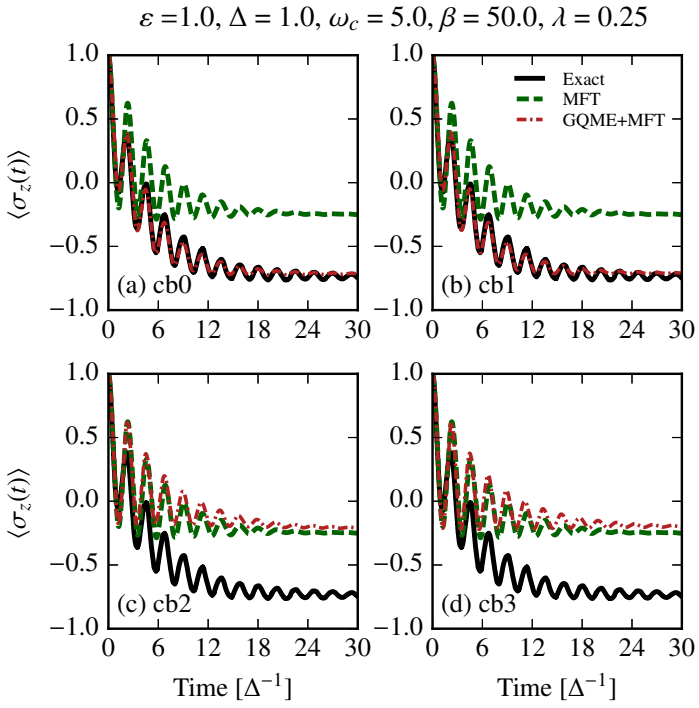

Figure 3.7: Comparison of population dynamics obtained from the $cb0$, $cb1$, $cb2$, and $cb3$ closures for the Redfield-type kernels, with $\tau_c = 2.0$. Exact results are obtained from Ref. [28].

that are easier to converge and auxiliary kernels that are easier to calculate, it should be preferred over the $cb0$ closure.

Inspection of panels (c) and (d) of the same figure shows that the $cb2$ and $cb3$ essentially recover the bare Ehrenfest behavior. Thus, we have demonstrated the remarkable fact that different closures for the memory function, all of which are exact when implemented with exact input, can yield markedly different results when combined with approximate dynamical input. The analytical proof that, for example, the $cb3$ (and $cf3$) closure must yield correlators that are identical to the use of the bare input dynamics is provided in the companion paper

[106]. The slight discrepancy between the *cb*3 and the Ehrenfest results may be attributed to the finite precision of the first and second numerical time derivatives of $\mathcal{C}(t)$. Further, the fact that the *cb*2 closure also recovers the bare Ehrenfest dynamics clearly indicates that the first of the two criteria specified in Ref. [106], i.e.,

$$\frac{d}{dt}[\langle\langle \rho A| \, e^{i\mathcal{L}t} \, |B\rangle\rangle]^{\mathrm{Eh}} = [\langle\langle \rho A| \, e^{i\mathcal{L}t} \, |(i\mathcal{L}B)\rangle\rangle]^{\mathrm{Eh}}, \tag{3.33}$$

where ρ corresponds to an initial, normalized density matrix and A and B are arbitrary operators, is satisfied by the Ehrenfest method. Indeed, the numerical data show that within the Ehrenfest approach the action of the Liouvillian acting on a dynamically sampled operator is equivalent to the numerical time-derivative of the analogous correlation function. In addition, given the violation of the second criterion ($[\mathcal{L}^{\mathrm{Eh}}, (e^{i\mathcal{L}t})^{\mathrm{Eh}}] \neq 0$), it is not surprising that the *cb*0 and *cb*1 closures yield GQME dynamics that are *distinct* from the the results of direct application of the Ehrenfest method. However, the violation of the second criterion does not explain the reason for the marked improvement in the dynamics afforded by the *cb*0 and *cb*1 closures. These results also lend additional credence to the claim that the success of the GQME+MFT approach does *not* rely on the short-time accuracy of Ehrenfest dynamics. Further, they illustrate that improvement within the memory formalism over the bare quasi-classical theory depends sensitively on the correlation functions calculated as input for the auxiliary kernels. In Sec. 3.4 we suggested that the Ehrenfest method might capture the dynamics of coherences more accurately than that of the populations, and that the self-consistent extraction of the memory kernel would include corrections to the population dynamics afforded by the ostensibly more accurate coherence dynamics. However, the recovery of Ehrenfest dynamics by closures *cb*2 and *cb*3, which also use the dynamics of

coherences, implies that this cannot be the root cause of the improvement of dynamics within the memory function approach. Instead, the more likely explanation is that the sampling of static bath operators in Eqs. (3.29) and (3.31) contributes important information about the system-bath interaction, which leads to far greater accuracy in the extracted memory kernels themselves.

The differences in the dynamics resulting from the different closures are also evident in the extracted memory kernels. Direct comparison of the Redfield-type memory kernels for cases characterized by the Debye spectral density fails to reveal much, since their highly oscillatory behavior obfuscates subtle differences among the memory kernels obtained from different closures. However, the fast decay of the Ohmic spectral density, which results in quickly decaying memory kernels with minor oscillations, makes discerning qualitative and quantitative differences between the extracted kernels possible. Fig. 3.8 compares a representative set of Redfield-type kernel elements arising from different closures. As is clear from the figure, all closures agree within numerical and sampling error in their $t = 0$ values. However, the *cb*2 and *cb*3 closures display a stronger oscillatory behavior, in contrast to the *cb*0 and *cb*1 closures, which correctly recover accurate dynamics (see Fig. 3.2). We further note that the difference in behavior is greatest at intermediate times.

The previous discussion suggests that the main factor leading to highly accurate memory kernels is the *exact* sampling of specific static bath operators. A corollary question arises: do all correlation functions with statically sampled bath operators lead to a similar improvement? After all, Eq. (3.28) samples $V_B^W(0)$ at $t = 0$, but its use in closure *cb*3 does not lead to any improvement over the bare Ehrenfest dynamics. This suggests either that the exact sampling of exclusively static bath operators adds an important correction to the auxiliary

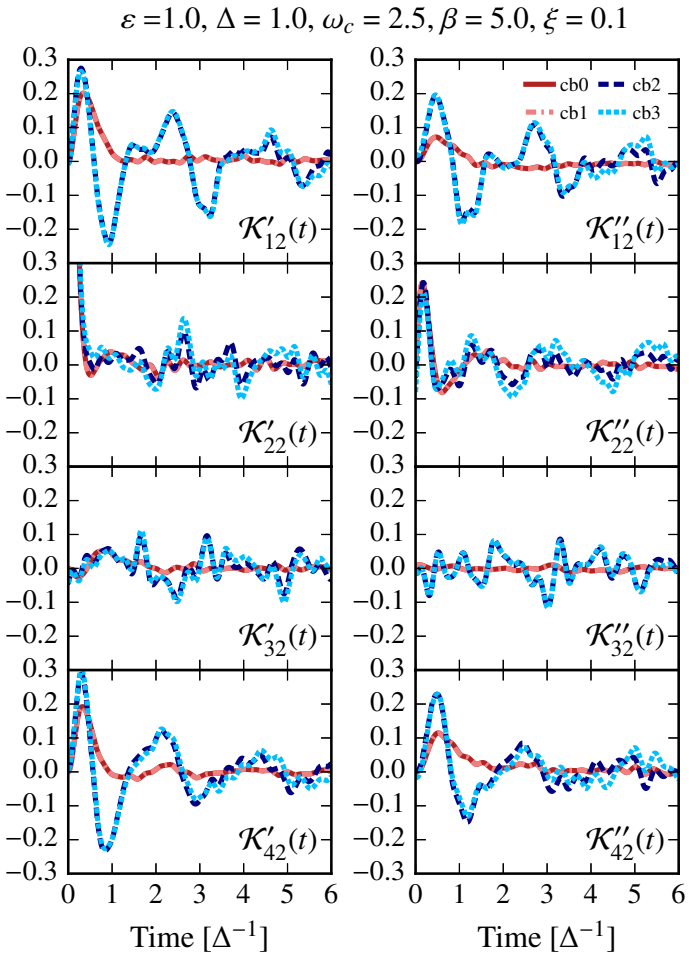

Figure 3.8: Comparison of Redfield-type memory kernel elements for $\mathcal{Q}$-backward closures *cb*0, *cb*1, *cb*2, and *cb*3 for the SB model with Ohmic spectral density. Consistent with the notation in Figs. 3.1 and 3.4, the memory kernel elements are separated into real and imaginary components, $\mathcal{K}_{x2}(t) = \mathcal{K}'_{x2}(t) + i\mathcal{K}''_{x2}(t)$.

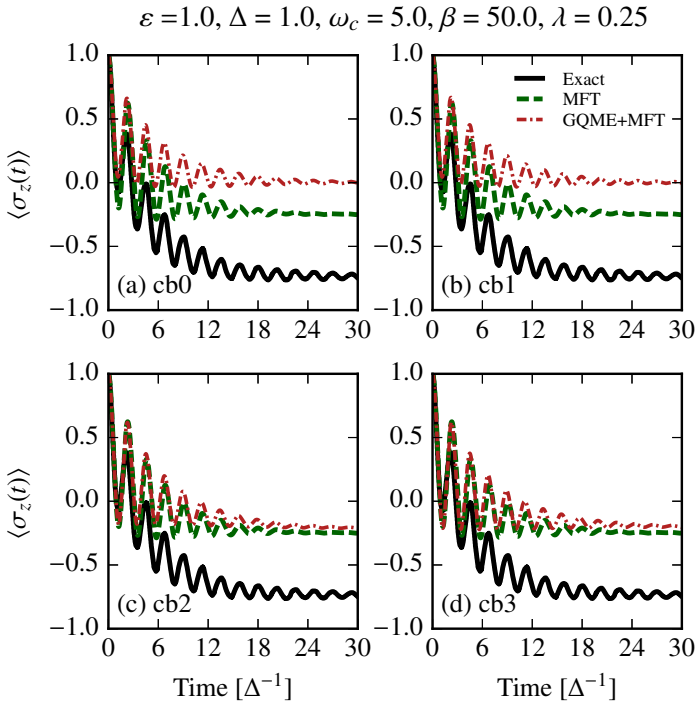

Figure 3.9: Comparison of population dynamics obtained from the $cb0$, $cb1$, $cb2$, and $cb3$ closures for the Redfield-type kernels when the making the approximation $[\rho_B V_B]^W \approx V_B^W V_B^W$. Exact results are obtained from Ref. [28].

kernels, or that correlation functions that sample $V_B^W(0)$ are not as important as those that sample ζ^W. The idea that ζ^W is neither sampled explicitly nor implicitly (via the Ehrenfest evolution protocol) in the calculation of $\mathcal{C}(t)$ provides some support to the latter claim. It is also fair to ask whether one can similarly benefit from "improperly" Wigner-transformed bath operator products sampled at $t = 0$. This question becomes particularly important when a functional form for the density operator of the bath is either not available or challenging to obtain. To see the importance of properly including the terms in the Wigner transformation,

we take an approximate form for the Wigner transform of the product $\rho_B V_B$ (defined in Appendix 3.D). Our approximation truncates the Moyal expansion for the Wigner transform of a product of operators at zeroth order in $\hbar$, neglecting the second term (containing ζ^W) on the right side of Eq. (3.79). Results for this approximation are shown in Fig. 3.9. As is evident in the figure, the benefits in closures $cb0$ and $cb1$ that originally led to the quantitative agreement between the GQME+MFT and exact dynamics are eliminated. Instead, the final result, while not unphysical, is not better than the standard Ehrenfest result. Since the $cb2$ and $cb3$ closures do not contain this neglected term, the results in panels (c) and (d) of Fig. 3.9 are the same as those in panels (c) and (d) of Fig. 3.7. This result underscores the importance of proper sampling of *all* contributions arising from the Wigner transform of operator products.

In comparison to the Redfield-type closures, the NIBA-type kernels (see Eqs. (3.66)–(3.68)) only contain two types of correlation functions, $q^{(00)}(t)$ and $q^{(10a)}(t)$. As mentioned in the discussion of the Redfield-type closures, $q^{(00)}(t)$ contains the same information as the Ehrenfest version of $\mathcal{C}(t)$, whereas $q^{(10a)}(t)$ contains *exact* information about the system-bath interaction at $t = 0$. For this reason, we expect the $c0b$ and $c1b$ closures to yield significantly better dynamics than the $cb2$ and $cb3$ closures, which should simply recover the Ehrenfest dynamics [106]. Indeed, as Fig. 3.10 shows, the $cb0$ and $cb1$ closures are able to quantitatively correct the Ehrenfest dynamics. In contrast to the Redfield case, the $cb0$ and $cb1$ NIBA-type auxiliary kernels require the sampling of the same bath operators, which explains the lack of difference in the behaviors of the two closures.

Of paramount importance to the success of the memory approach is the finite lifetime of the memory kernel. For the GQME+MFT implementation used here, we have chosen a

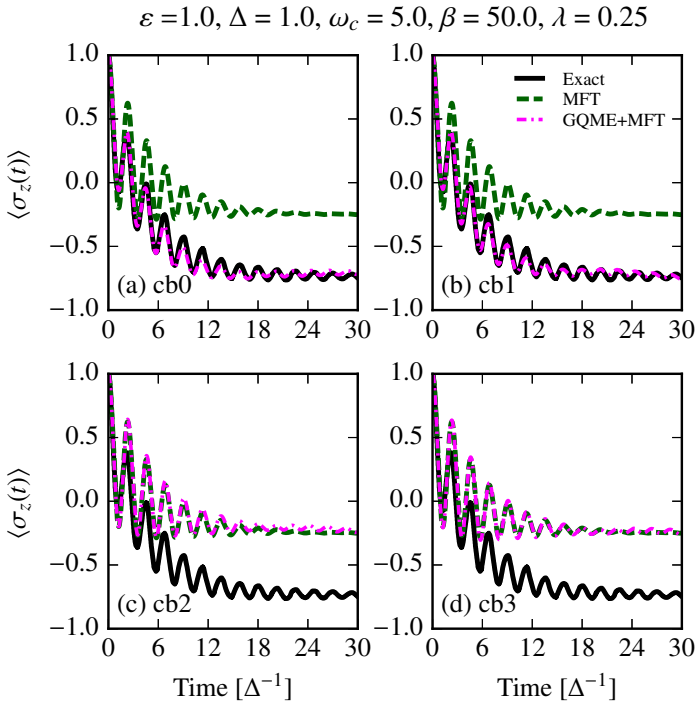

Figure 3.10: Comparison of population dynamics obtained from the $\mathcal{Q}$-backward closures $cb0$, $cb1$, $cb2$, and $cb3$ for the NIBA-type kernels with $\tau_c = 20.0$. Exact results are obtained from Ref. [28].

cutoff time for the memory kernel, τ_c, which lies in a stability plateau alluded to in Sec. 3.4. The range of the stability plateau can depend sensitively on the regime of parameter space explored. Fig. 3.11 shows the dependence of the GQME+MFT dynamics for the Redfield- and NIBA-type projectors on the specific value of τ_c used. Panels (a) and (b), corresponding to a fast bath, high temperature, biased case, show the greatest sensitivity of the GQME dynamics to the exact cutoff time, τ_c. In contrast, the results in panels (c) and (d), which correspond to lower temperatures, are more stable. Despite the slight

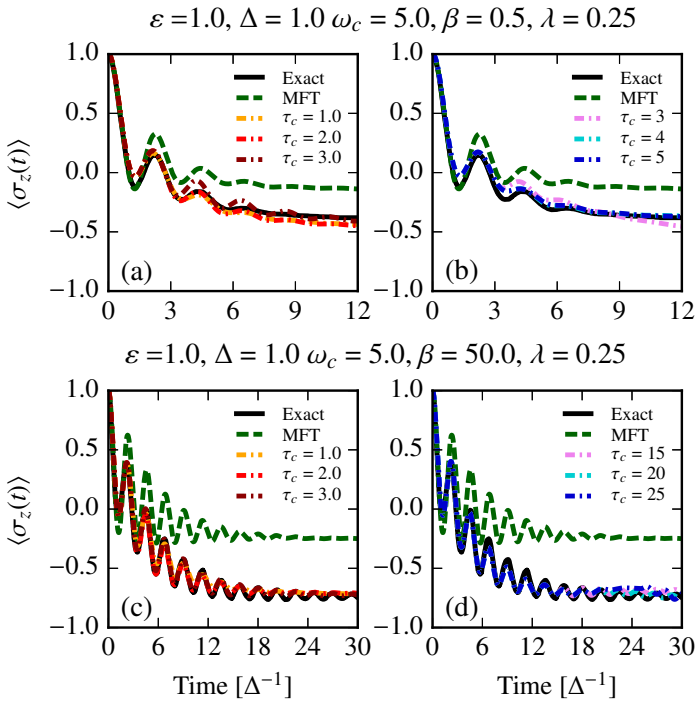

Figure 3.11: Comparison of population dynamics obtained using the *cb*1 closures for the Redfield- and NIBA-type kernels with varying τ_c. Panels (a) and (c) correspond to the Redfield-type projector, while panels (b) and (d) correspond to the NIBA-type projector. Exact results are obtained from Ref. [28].

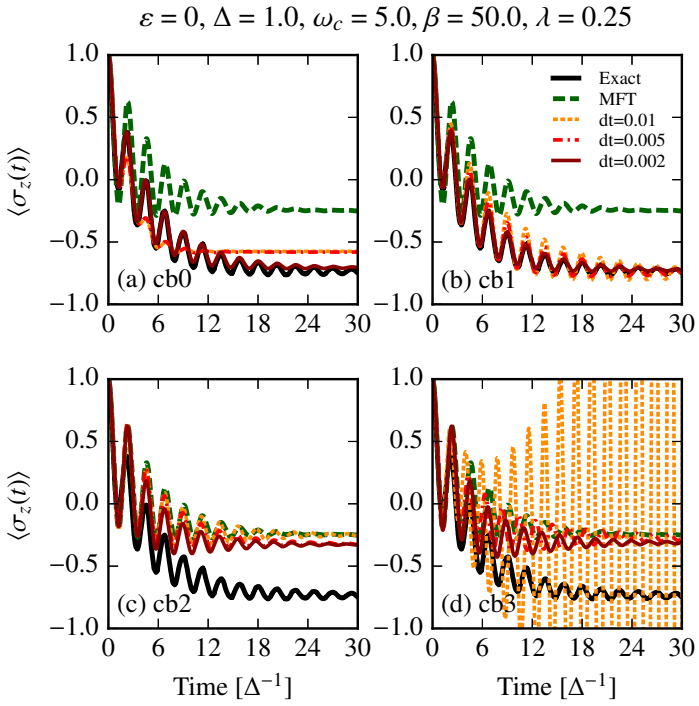

Figure 3.12: Comparison of population dynamics obtained from the $\mathcal{Q}$-backward closures $cb0$, $cb1$, $cb2$, and $cb3$ for the Redfield-type kernels with $\tau_c = 2.0$ upon varying the time step used in the GQME evolution. Note that the actual time step used in the GQME solution is twice that used in the calculation of the memory kernels. Exact results are obtained from Ref. [28].

sensitivity of the results on the choice of τ_c for the examples shown, the GQME dynamics are clearly robust. We remark, however, that there are regions of parameter space for which this stability plateau is short-lived or nonexistent. In those cases, the present approach is clearly not appropriate.

Finally, we address the convergence properties of the GQME dynamics with respect to

the time-step of the memory kernel and the GQME evolution algorithm. As Fig. 3.12 shows, decreasing the time step used in the extraction of the memory kernel can greatly alter the accuracy of the GQME dynamics. The closures most sensitive to the time step are $cb0$ and $cb3$ closures. The sensitivity of the $cb3$ closure to the time step is not difficult to understand, since for large dt the second numerical time derivative becomes noisy, leading to the growing oscillations in panel (d). Because closure $cb0$ shown in panel (a) contains the correlation functions $q^{(11s)}(t)$ and $q^{(11a)}(t)$, which require sampling of bath operators at $t = 0$ and at finite times and are highly oscillatory functions, a smaller time step is required to achieve sufficiently accurate memory kernels. It is important to note that, as stated before, the $cb0$ and $cb1$ closures, when fully converged with respect to bath realizations and time step, yield identical results that greatly improve the Ehrenfest results, while closures $cb2$ and $cb3$ are only capable of recovering the Ehrenfest dynamics.

3.5 Conclusions

In this paper we have developed a method to obtain the nonequilibrium population and coherence dynamics based on the Mori formalism. Our approach is general and, depending on the choice of projector, can treat arbitrary single-time nonequilibrium populations and coherences as well as more complicated dynamical objects, such as multi-time, equilibrium and nonequilibrium correlation functions. We have shown that use of the Redfield-type projector recovers the conventional NZ treatment previously used by Shi and Geva [93, 94, 144] and Kelly, Markland, and coworkers [101–103] in the context of the SB model, and Rabani and coworkers [95–99] for more general models.

While previous applications of the GQME+semi-classical approach [101, 102, 144] have been limited to the Redfield-type projector and have focused on the improvement over the bare semi-classical dynamics that the memory function formalism can afford, we have systematically explored the sensitivity of the results to the choice of projector and the type of closure employed. In doing so, we find two important facts. First, slowly decaying memory kernels, often observed when using the NIBA-type projector, do not result in an inaccurate description of the GQME dynamics. This demonstrates that the success of the GQME+semi-classical approach is *not* a function of the short-time accuracy of the approximate method used to calculate the auxiliary kernels. Second, we identify the types of closures that consistently lead to improvements over the bare semi-classical dynamics ($cb0$, $cb1$, $cf0$, and $cf1$) and attribute this improvement, in part, to the sampling of static bath operators, ζ^W, which do not appear in the evaluation of the approximate bare populations. Just as importantly, we identify the types of closures that recover the Ehrenfest dynamics ($cb2$, $cb3$, $cf2$, and $cf3$). Our findings also provide numerical confirmation of the analytical proof included in the companion paper [106], which indicates that use of the $cb3$ and $cf3$ closures *can only* recover the level of dynamics used to calculate the auxiliary kernels.

Finally, we remark that the Mori-based formulation furthered in this work provides a flexible framework to accurately study problems that go beyond the scope of nonequilibrium dynamics for SB-type models. For instance, the Mori formalism can easily address equilibrium and multi-time correlation functions in systems coupled to harmonic *and* anharmonic baths, as well as problems where the system-bath distinction is absent. Work in this latter direction will be pursued in future papers.

Appendix

3.A Fourier-Laplace Analysis of Closures

We begin by introducing the Fourier-Laplace transform of a time-dependent function $f(t)$,

$$f(\omega) = \int_0^\infty dt e^{i\omega t} f(t). \tag{3.34}$$

Its first and second time-derivatives take the following form,

$$\int_0^\infty dt e^{i\omega t} \dot{f}(t) = -f(0) + (-i\omega) f(\omega), \tag{3.35}$$

$$\int_0^\infty dt e^{i\omega t} \ddot{f}(t) = -\dot{f}(0) - (-i\omega) f(0) + (-i\omega)^2 f(\omega). \tag{3.36}$$

The kernel expansions in Eqs. (3.13) and (3.16) can be rewritten as follows,

$$\mathcal{K}(\omega) = [1 - \mathcal{K}^{(3b)}(\omega)]^{-1} \mathcal{K}^{(1)}(\omega) \tag{3.37}$$

$$= \mathcal{K}^{(1)}(\omega)[1 - \mathcal{K}^{(3f)}(\omega)]^{-1}. \tag{3.38}$$

In their original paper, Shi and Geva [93] derived the following identity for the Redfield-type (thermal) projector,

$$\mathcal{Q}\mathcal{L}\mathcal{Q} = \mathcal{Q}(\mathcal{L} - \mathcal{P}\mathcal{L}_{sb}), \tag{3.39}$$

$$= (\mathcal{L} - \mathcal{L}_{sb}\mathcal{P})\mathcal{Q}, \tag{3.40}$$

where $\mathcal{L}_{sb}$ is the Liouvillian corresponding to the system-bath interaction for the SB model $V = \alpha\sigma_z \sum_k c_k x_k$. The second line is a simple extension of the derivation provided by Shi and Geva. These identities allow for the exact rewriting of the "$\mathcal{Q}$-surrounded" projected propagator,

$$\mathcal{Q}e^{i\mathcal{Q}\mathcal{L}t}\mathcal{Q} = \mathcal{Q}e^{i(\mathcal{L}-\mathcal{P}\mathcal{L}_{sb})t}\mathcal{Q} \tag{3.41}$$

$$= \mathcal{Q}e^{i(\mathcal{L}-\mathcal{L}_{sb}\mathcal{P})t}\mathcal{Q}. \tag{3.42}$$

Replacing these expressions for the projected propagator in Eq. (3.10) followed by use of the Dyson decomposition leads to the following *three-* rather than *two*-membered expansions,

$$\mathcal{K}(t) = \mathcal{K}^{(1)}(t) + \int_0^t d\tau\ \mathcal{K}^{(2b)}(t-\tau)\mathcal{K}^{(1)}(\tau), \tag{3.43}$$

$$= \mathcal{K}^{(1)}(t) + \int_0^t d\tau\ \mathcal{K}^{(1)}(t-\tau)\mathcal{K}^{(2f)}(\tau), \tag{3.44}$$

where the second auxiliary kernel also contains the projected propagator,

$$\mathcal{K}^{(2b)}_{nm}(t) = -i\langle\langle \rho_B A_n |\, \mathcal{L}_{sb} e^{i(\mathcal{L}-\mathcal{P}\mathcal{L}_{sb})t}\, |A_m\rangle\rangle, \tag{3.45}$$

$$\mathcal{K}^{(2f)}_{nm}(t) = -i\langle\langle \rho_B A_n |\, e^{i(\mathcal{L}-\mathcal{L}_{sb}\mathcal{P})t} \mathcal{L}_{sb}\, |A_m\rangle\rangle. \tag{3.46}$$

In Fourier-Laplace space, the previous expressions for the memory kernel become,

$$\mathcal{K}(\omega) = \mathcal{K}^{(1)}(\omega) + \mathcal{K}^{(2b)}(\omega)\mathcal{K}^{(1)}(\omega), \tag{3.47}$$

$$= \mathcal{K}^{(1)}(\omega) + \mathcal{K}^{(1)}(\omega)\mathcal{K}^{(2f)}(\omega). \tag{3.48}$$

In the time-domain, the second auxiliary kernels may be expanded as follows,

$$\mathcal{K}^{(2x)}(t) = \mathcal{K}^{(3x)}(t) + \int_0^t d\tau\ \mathcal{K}^{(2x)}(t-\tau)\mathcal{K}^{(3x)}(\tau), \tag{3.49}$$

$$= \mathcal{K}^{(3x)}(t) + \int_0^t d\tau\ \mathcal{K}^{(3x)}(t-\tau)\mathcal{K}^{(2x)}(\tau), \tag{3.50}$$

where $x \in \{b, f\}$. Transforming Eqs. (3.49) and (3.50), we may solve for $\mathcal{K}^{(2x)}(\omega)$

$$\mathcal{K}^{(2x)}(\omega) = \mathcal{K}^{(3x)}(\omega)[1 + \mathcal{K}^{(3x)}(\omega)]^{-1}, \tag{3.51}$$

$$= [1 + \mathcal{K}^{(3x)}(\omega)]^{-1}\mathcal{K}^{(3x)}(\omega). \tag{3.52}$$

Substitution of Eqs. (3.51) and (3.52) into Eqs. (3.47) and (3.48) for the $\mathcal{Q}$-forward and $\mathcal{Q}$-backward closures yields,

$$\mathcal{K}(\omega) = [1 - \mathcal{K}^{(3b)}(\omega)]^{-1}\mathcal{K}^{(1)}(\omega) \tag{3.53}$$

$$= \mathcal{K}^{(1)}(\omega)[1 - \mathcal{K}^{(3f)}(\omega)]^{-1}, \tag{3.54}$$

which are clearly equivalent to Eqs. (3.37) and (3.38), implying that the three-membered closures are equivalent to the two-membered closures.

3.B Expressions for Auxiliary Kernels

Here we provide explicit expressions for the components of the memory kernel using the Redfield- and NIBA-type projection operators. Before going further, however, we introduce for notational clarity the following correlation functions.

$$q_{nm}^{(00)} = \mathrm{Tr}[\rho_B A_n^\dagger A_m(t)], \tag{3.55}$$

$$q_{nm}^{(01)} = \mathrm{Tr}[\rho_B A_n^\dagger A_m(t) V_B(t)], \tag{3.56}$$

$$q_{nm}^{(10s)} = \frac{1}{2}\mathrm{Tr}[\{V_B, \rho_B\} A_n^\dagger A_m(t)], \tag{3.57}$$

$$q_{nm}^{(10a)} = \frac{-i}{2}\mathrm{Tr}[[V_B, \rho_B] A_n^\dagger A_m(t)], \tag{3.58}$$

$$q_{nm}^{(11s)} = \frac{1}{2}\mathrm{Tr}[\{V_B, \rho_B\} A_n^\dagger A_m(t) V_B(t)], \tag{3.59}$$

$$q_{nm}^{(11a)} = \frac{-i}{2}\mathrm{Tr}[[V_B, \rho_B] A_n^\dagger A_m(t) V_B(t)], \tag{3.60}$$

where s and a indicate symmetrized (anticommutator) or antisymmetrized (commutator) bath products.

Using the Redfield-type projector,

$$\mathcal{P}_{Red} = \sum_i |A_i\rangle\rangle\langle\langle \rho_B A_i| \,, \tag{3.61}$$

where $A_i \in \{|0\rangle\langle 0|, |1\rangle\langle 0|, |1\rangle\langle 0|, |1\rangle\langle 1|\}$, $i \in \{1,2,3,4\}$, and $\rho_B = e^{-\beta H_B}/\mathrm{Tr}_B[e^{-\beta H_B}]$, the elements of the memory kernels take the following forms,

$$[\mathcal{K}^{(1)}(t)]_{nm} = [X_n q^{(11s)}_{nm}(t) + iY_n q^{(11a)}_{nm}(t)]X_m, \tag{3.62}$$

$$[\mathcal{K}^{(3b)}(t)]_{nm} = iX_n q^{(10s)}_{nm}(t) - Y_n q^{(10a)}_{nm}(t), \tag{3.63}$$

$$[\mathcal{K}^{(3f)}(t)]_{nm} = iq^{(01)}_{nm}(t)X_m, \tag{3.64}$$

where $X_n = 2(\delta_{n3} - \delta_{n2})$ and $Y_n = 2(\delta_{n1} - \delta_{n4})$.

Using the NIBA-type projector,

$$\mathcal{P}_{NIBA} = \sum_i |B_i\rangle\rangle\langle\langle \rho_B B_i| \,, \tag{3.65}$$

where $B_i \in \{|0\rangle\langle 0|, |1\rangle\langle 1|\}$, $i \in \{1,2\}$ and $\rho_B = e^{-\beta H_B}/\mathrm{Tr}_B[e^{-\beta H_B}]$, the elements of the memory kernels take the following forms,

$$[\mathcal{K}^{(1)}(t)]_{nm} = 2(-1)^{n+m}\Big[2\Delta\Im[q^{(10a)}_{n^2 2}(t)] - \Delta^2\Re[q^{(00)}_{32}(t) - q^{(00)}_{33}(t)]\Big], \tag{3.66}$$

$$[\mathcal{K}^{(3b)}(t)]_{nm} = 2(-1)^{n}\Big[q^{(10a)}_{n^2 m^2}(t) + \Delta\Im[q^{(00)}_{n^2 2}(t)]\Big], \tag{3.67}$$

$$[\mathcal{K}^{(3f)}(t)]_{nm} = 2\Delta(-1)^{m}\Im[q^{(00)}_{n^2 2}(t)]. \tag{3.68}$$

We employ a notation where some indices are squared since the $q(t)$ functions are labelled using the indices corresponding to the A_j operators, which are related to the B_j operators in the following way: $B_1 \mapsto A_1 = A_{1^2}$ and $B_2 \mapsto A_4 = A_{2^2}$.

For the projector above to be truly of NIBA-type, $\mathcal{K}^{(1)}(t)$ should be $\mathcal{O}(\Delta^2)$. Instead, $\mathcal{K}^{(1)}(t)$ has contributions of first and second order in Δ. Indeed, the proper NIBA-type projector has the following form,

$$\mathcal{P}_{NIBA} = \sum_i |B_i\rangle\rangle\langle\langle \rho_B^{(i)} B_i| \,, \tag{3.69}$$

where $\rho_B^{(i)} = e^{-\beta(H_B-(-1)^i\alpha V_B)}/\mathrm{Tr}_B[e^{-\beta(H_B-(-1)^i\alpha V_B)}]$.

3.C Initial Conditions in the Ehrenfest method

In an open quantum system where a subsystem interacts weakly with a heat bath, the Ehrenfest method [61, 62, 126, 139] treats the subsystem quantum mechanically and the bath classically. The validity of this approximation relies on two important assumptions: correlations between the system and bath are negligible, and the characteristic energy of the bath is smaller than the other energy scales in the problem, justifying the use of classical mechanics for the evolution of the bath.

The Ehrenfest method has been derived from complementary wavefunction [126] and density matrix formulations [139]. Because of its clarity, the derivation based on the density matrix and the quantum-classical Liouville equation has garnered much attention in the last decade. The density matrix formulation only requires that the subsystem and bath density matrices have norms equal to unity. However, the lack of restriction of the subsystem density matrix to pure states results in ambiguities in its implementation. To illustrate the source of the ambiguity, we focus on the following correlation function for the spin-boson model

$$C(t) = \mathrm{Tr}[R_B \sigma_i \sigma_z(t)], \tag{3.70}$$

where $i \in \{x, y\}$, and the bath initial condition has unit trace, $\mathrm{Tr}_B[R_B] = 1$. This corresponds to a nonequilibrium initial condition where the system is initially in a superposition of coherences. Immediately it is clear that $\rho_S(0) = \sigma_i$ has zero norm. To remedy this, one may take advantage of the linearity of the problem and rewrite Eq. (3.70) into sums of correlation functions with proper initial conditions,

$$C(t) = \mathrm{Tr}[R_B(|1\rangle\langle 1| + \sigma_i)\mathcal{O}(t)] - \mathrm{Tr}[R_B|1\rangle\langle 1|\mathcal{O}(t)], \tag{3.71}$$

$$= \mathrm{Tr}[R_B(|2\rangle\langle 2| + \sigma_i)\mathcal{O}(t)] - \mathrm{Tr}[R_B|2\rangle\langle 2|\mathcal{O}(t)], \tag{3.72}$$

$$= \frac{1}{2}\mathrm{Tr}[R_B(\mathbf{1}_S + 2\sigma_i)\mathcal{O}(t)] - \frac{1}{2}\mathrm{Tr}[R_B\mathbf{1}_S\mathcal{O}(t)], \tag{3.73}$$

where $\mathbf{1}_S = |1\rangle\langle 1| + |2\rangle\langle 2|$.

Returning to the wavefunction-based derivation of the Ehrenfest approach requires that any subsystem initial condition correspond to a pure state. Referring again to Eq. (3.70), we may rewrite the trace over the subsystem in the eigenbasis of the subsystem's initial condition,

$$C(t) = \sum_i \lambda_i \mathrm{Tr}_B[R_B\langle\lambda_i|\sigma_z(t)|\lambda_i\rangle]. \tag{3.74}$$

Although there are other ways of choosing a pure state so as to evaluate the above correlation function, the wavefunction formulation avoids the ambiguity fostered by the density matrix derivation.

Fig. 3.C.1 shows the calculation of the nonequilibrium population dynamics given different system initial conditions, $\rho_S(0) \in \{\sigma_x, \sigma_y, |1\rangle\langle 1|\}$. For the initial conditions corresponding to the Pauli matrices, we implement three different decompositions given by Eqs. (3.71), (3.72), and (3.73), labeled A, B, and C, respectively. We also include the results for two different decompositions for the initial condition $|1\rangle\langle 1|$, labeled A and B. As is clear from pan-

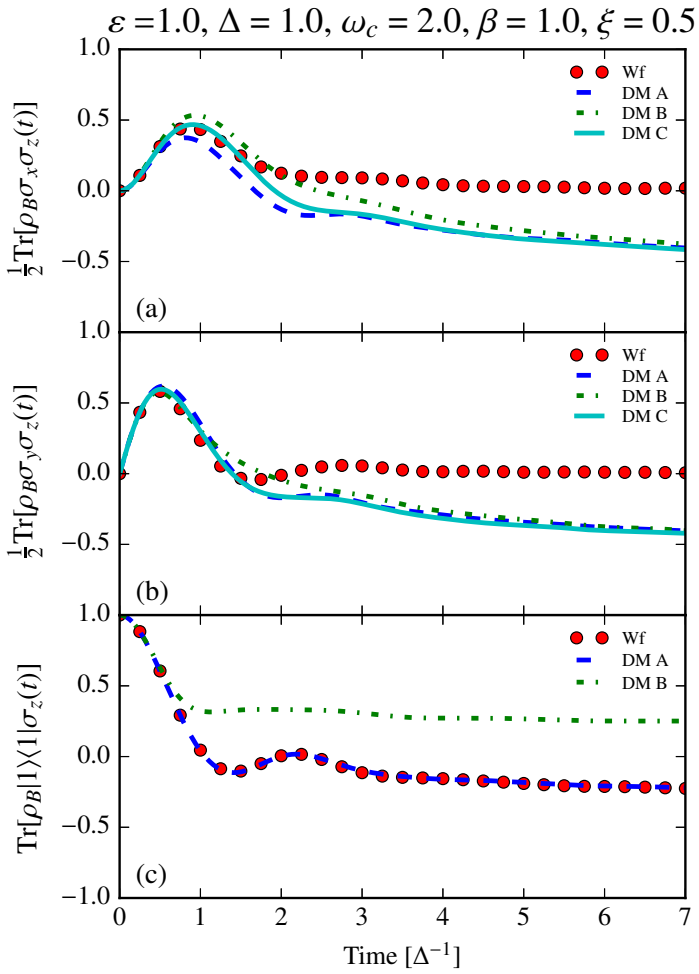

Figure 3.C.1: Comparison of Ehrenfest dynamics resulting from the wavefunction- and density matrix-based approaches. In panels (a) and (b), DM 1 corresponds to the following combination of initial conditions $[|1\rangle\langle 1| + \sigma_i] - [|1\rangle\langle 1|]$, DM 2 to $[|2\rangle\langle 2| + \sigma_i] - [|2\rangle\langle 2|]$, and DM 3 to $[0.5 * \mathbf{1}_S + \sigma_i] - [0.5 * \mathbf{1}_S]$, where $i = x, y$ for panels (a) and (b), respectively. In panel (c), DM 1 corresponds to $[|1\rangle\langle 1| + \sigma_y] - [|1\rangle\langle 1|]$, and DM 2 to $2 * [0.5 * \mathbf{1}_S] - [|1\rangle\langle 1|]$.

els (a) and (b), all density matrix based decompositions agree in their short- and long-time limits, but disagree in their descriptions of intermediate-time behavior. More importantly, all density matrix decompositions disagree with the wavefunction-based result. Panel (c) shows the ability of the density matrix-based approach to recover the wavefunction-based result when the initial condition corresponds to a population rather than a coherence, but decomposition B underscores the problems associated with the lack of uniqueness in the density matrix based approach.

3.D Ehrenfest Method: Correlation Functions

Unlike previous implementations of the Ehrenfest method, we are interested in two time correlation functions rather than nonequilibrium single quantity dynamics,

$$C_{AB}(t) = \mathrm{Tr}[\mathcal{A}_S(0)\mathcal{A}_B(0)\mathcal{B}_S(t)\mathcal{B}_B(t)], \tag{3.75}$$

where X_S (X_B) is a generic system (bath) operator. Under the quasi-classical approximation of Wigner dynamics, we may rewrite the above correlation function as follows,

$$C_{AB}(t) \approx \int d\Gamma \; \mathcal{A}_B^W \mathcal{B}_B^W(t) \mathrm{Tr}_S[\mathcal{A}_S(0)\mathcal{B}_S(t)], \tag{3.76}$$

where the superscript W denotes the Wigner transform of the operator and Γ is the set of all classical variables.

For the auxiliary kernels of the spin-boson model, the following Wigner transforms are

necessary,

$$\rho_B^W = \prod_j \frac{\tanh(\beta\omega_j/2)}{\pi} \exp\left[-\frac{\tanh(\beta\omega_j/2)}{\omega_j}\Big[P_j^2+\omega_j^2 Q_j^2\Big]\right], \tag{3.77}$$

$$V_B^W = \alpha\sum_j c_j Q_j, \tag{3.78}$$

and, using the Moyal bracket for products of operators [145],

$$[V_B\rho_B]^W = \alpha V_B^W\rho_B^W + i\zeta^W\rho_B^W, \tag{3.79}$$

where

$$\zeta^W = -\alpha\sum_j c_j P_j\frac{\tanh(\beta\omega_j/2)}{\omega_j} \tag{3.80}$$

Using the above definitions, the correlation functions in Eqs. (A1)–(A6) take the following form under the Ehrenfest approximation,

$$q_{nm}^{(00)}(t) = \int d\Gamma\ \rho_B^W \mathrm{Tr}_{\mathrm{sys}}[A_n^\dagger A_m(t)], \tag{3.81}$$

$$q_{nm}^{(01)}(t) = \int d\Gamma\ \rho_B^W V_B^W(t)\mathrm{Tr}_{\mathrm{sys}}[A_n^\dagger A_m(t)], \tag{3.82}$$

$$q_{nm}^{(10s)}(t) = \int d\Gamma\ \rho_B^W V_B^W(0)\mathrm{Tr}_{\mathrm{sys}}[A_n^\dagger A_m(t)], \tag{3.83}$$

$$q_{nm}^{(10a)}(t) = \int d\Gamma\ \rho_B^W \zeta^W(0)\mathrm{Tr}_{\mathrm{sys}}[A_n^\dagger A_m(t)], \tag{3.84}$$

$$q_{nm}^{(11s)}(t) = \int d\Gamma\ \rho_B^W V_B^W(0)V_B^W(t)\mathrm{Tr}_{\mathrm{sys}}[A_n^\dagger A_m(t)], \tag{3.85}$$

$$q_{nm}^{(11a)}(t) = \int d\Gamma\ \rho_B^W \zeta^W(0)V_B^W(t)\mathrm{Tr}_{\mathrm{sys}}[A_n^\dagger A_m(t)]. \tag{3.86}$$

The above considerations regarding the subtlety in the density matrix picture with regard to the implementation of the Ehrenfest method underlines an important interpretation issue.

While it is often regarded that in the Ehrenfest method the system (bath) evolves under the mean field of the classical (quantum) variables, it is important to add the caveat that these mean fields correspond to single rather than ensembles of trajectories. As such, under the Ehrenfest approximation the system evolves under the time-dependent Hamiltonian defined as

$$H_{S,Eh}(t) = [\varepsilon + \lambda^{cl}(t)]\sigma_z + \Delta\sigma_x \tag{3.87}$$

where the classical bath provides a fluctuating contribution to the bias energy $\lambda^{cl}(t) = \alpha \sum_k c_k Q_k(t)$ and the equation of motion for the density matrix of the system is the Liouville equation using the modified Hamiltonian,

$$\frac{d}{dt}\rho_S(t) = -i[H_S^{Eh}, \rho(t)]. \tag{3.88}$$

The bath, in turn, evolves under the influence of the time-dependent Hamiltonian

$$H_B^{Eh}(t) = \frac{1}{2}\sum_k \Big[P_k^2 + \omega_k^2 Q_k + 2\alpha\bar{\sigma}_z(t)c_k Q_k\Big], \tag{3.89}$$

where $\bar{\sigma}_z(t) = \mathrm{Tr}_S[\rho_S(t)\sigma_z]$, and the equations of motion for the classical variables are given by Hamilton's equations,

$$\frac{dP_k}{dt} = -\frac{\partial H_B^{Eh}}{\partial Q_k}, \tag{3.90}$$

$$\frac{dQ_k}{dt} = \frac{\partial H_B^{Eh}}{\partial P_k}. \tag{3.91}$$

$$\tag{3.92}$$

To calculate auxiliary kernels used in the present work, trajectories corresponding to a set of initial conditions given by the Wigner distribution, Eq. (3.77), are calculated via a second-order Runge-Kutta scheme. During individual time steps, $\bar{\sigma}_z(t)$ is kept constant for

the evolution of the bath, while $\lambda^{cl}(t)$ is kept constant during the evolution of the system. Over a half time step, the equations for the classical variables take the forms,

$$Q_k\left(t+\frac{\delta t}{2}\right) = \gamma_k(t)\cos\left(\frac{\omega_k\delta t}{2}\right) - \frac{\alpha c_k}{\omega_k^2}\bar{\sigma}_z(t) + \frac{P_k(t)}{\omega_k}\cos\left(\frac{\omega_k\delta t}{2}\right), \tag{3.93}$$

and

$$P_k\left(t+\frac{\delta t}{2}\right) = P_k(t)\cos\left(\frac{\omega_k\delta t}{2}\right) + \omega_k\gamma_k(t)\sin\left(\frac{\omega_k\delta t}{2}\right), \tag{3.94}$$

where

$$\gamma_k(t) = Q_k(t) + \frac{\alpha c_k}{\omega_k^2}\bar{\sigma}_z(t). \tag{3.95}$$

While convergence for correlation functions of system operators only requires only $\sim 10^3 - 10^4$ trajectories, correlation functions with bath operators require $\sim 3\times10^4 - 10^5$ trajectories for sufficiently accurate results.

Chapter 4

Approximate but accurate quantum dynamics from the Mori formalism: II. Equilibrium correlation functions.

4.1 Introduction

By encoding a system's response to a weak perturbation [146], equilirbrium time correlation functions (ECF) provide direct access to the dynamical quantities that characterize important quantities such as transport coefficients,[147, 148] absorption spectra [15], and chemical rate constants [134, 148, 149]. It is therefore not surprising that the development of accurate and efficient approaches to the calculation of EFCs has been a focus of intense theoretical investigation, spawning a rich array of analytical and computational methods.

Attempts at calculating ECFs face the challenge of striking a balance between computa-

tional tractability and accuracy. On the more computationally expensive side lie numerically exact schemes, which are generally restricted to small, idealized models and tend to scale unfavorably, and at worst exponentially, with simulation time [132, 150–157]. Approximate methods, on the other hand, are more scalable to realistic, multidimensional systems, but suffer from limited accuracy. These include perturbative approaches [1, 42, 43, 158], analytic continuation [73–78], quantum mode coupling theory [68–72], and quasi- [61–64, 126] and semi-classical [44–49, 51–60, 65–67] methods. While each method has its virtues, all suffer from limited applicability, either due the violation of parameter regime restrictions, the breakdown of uncontrolled approximations, or convergence problems. As a result, despite the availability of many methods for the calculation of ECFs, there remains a clear need for the development of widely applicable, accurate, and computationally efficient approaches.

A successful marriage of computational efficiency and accuracy may be enabled through a judicious use of the Mori formalism. Based on the projection operator technique [129, 130], the Mori approach provides a simple, low-dimensional equation of motion for the ECF, called a generalized quantum master equation (GQME). The reduced dimensionality of the GQME corresponds to that of the space spanned by the observables probed in the ECF, while the influence of the excluded degrees of freedom is encoded in the memory kernel. Calculation of the memory kernel, in turn, is beset by two difficulties: application of the projected propagator, $e^{i\mathcal{Q}\mathcal{L}t}$, and the full dimensionality of the original problem. The former can be sidestepped using a Dyson-type expansion, which leads to a self-consistent equation for the memory kernel that requires only the calculation of projection-free auxiliary kernels [93]. The latter, however, continues to plague the calculation of the auxiliary kernels. Nevertheless, this approach has been vigorously pursued to obtain nonequilibrum averages

in the context of impurity-type models where the auxiliary kernels have been obtained via numerically exact [93–99] or approximate methods [100–104, 106]. These studies have shown that the short lifetime of the memory kernels can lead to dramatic increases in computational efficiency, regardless of the method used to compute the memory kernels [93–104, 106]. Just as importantly, when approximate methods are used, the Mori approach has also provided impressive boosts in accuracy over the bare approximate dynamics [100–104, 106]. Hence, the approach based on the GQME coupled to the self-consistent solution of the memory kernel shows great promise as a means of increasing the efficiency and, when appropriate, accuracy of dynamical methods.

Here we argue that the remarkable boosts in efficiency and accuracy afforded by the GQME approach can be extended to arbitrary systems and dynamical quantities beyond simple nonequilibrium averages. To show the viability of the approach, we specialize the Mori approach to treat the symmetrized ECFs for the spin variables of the spin-boson (SB) model [1, 2]. In the same spirit as the first paper of this series [104], we calculate the auxiliary kernels necessary for the self-consistent solution of the memory kernel via the mean-field Ehrenfest method and assess the potential benefits of this approach in terms of increases in efficiency and accuracy (we henceforth refer to the this framework as the GQME+MFT approach). In this work, we also endeavor to elucidate the dependence of the GQME dynamics on the choice of closure, and try to provide further evidence for the claim that the source of the improvement over bare semiclassical dynamics afforded by the GQME framework depends, at least partially, on the *exact* sampling of *distinct* initial conditions necessary in the calculation of the auxiliary kernels. It also bears remarking that the Mori approach can be easily generalized to multi-time correlation functions and is applicable to

a wide variety of systems. In fact, a major advantage of the Mori formulation is that it can naturally address problems where the system-bath dichotomy is absent, such as spin and fermion lattice models [5–7], and quantum fluids [8, 9, 72, 135].

The paper is organized as follows. In Sec. 4.2, we briefly introduce SB model and the projection operator that allows for the investigation of symmetrized correlation functions of the Pauli matrices. Sec. 4.3, compares the dynamics obtained via the GQME+MFT approach to numerically exact results for the symmetrized spin-spin correlation function $\mathcal{C}_{zz}(t) = \mathrm{Re}\langle\sigma_z(0)\sigma_z(t)\rangle$. Sec. 4.3 explores the dependence of GQME results on the choice of closure and the accuracy of the initial conditions. Sec. 4.4 is devoted to our concluding remarks.

4.2 Mori Approach

As in paper I, we apply the Mori formalism for ECFs to the SB model, which is representative of typical condensed phase systems that exhibits nontrivial decoherence and dissipation patterns [1, 2]. We note, however, that the Mori approach is general and may be applied to any Hamiltonian system, including those where the system-bath distinction is absent. This point is of crucial importance for the modeling of quantum correlation functions such as those associated with absorption spectra in liquids [9].

The SB Hamiltonian takes the form $H = H_S + H_B + H_{SB}$, where

$$H_S = \varepsilon\sigma_z + \Delta\sigma_x, \tag{4.1}$$

corresponds to the system part of the Hamiltonian. Here, 2ε corresponds the energy difference between the two sites, Δ, which is assumed to be static, represents the tunneling

matrix element, and σ_i corresponds to the i^{th} Pauli matrix.

The bath Hamiltonian consists of independent harmonic oscillators,

$$H_B = \frac{1}{2}\sum_k \left[\hat{P}_k^2 + \omega_k^2 \hat{Q}_k^2\right], \tag{4.2}$$

where P_k, Q_k and ω_k are the mass-weighted momenta, coordinates, and the frequency for k^{th} harmonic oscillator, respectively. The system-bath coupling is assumed to be of the form,

$$V = \alpha\sigma_z \sum_k c_k \hat{Q}_k, \tag{4.3}$$

where c_k is the coupling constant describing the strength of the interaction between the system and the k^{th} oscillator and $\alpha = \pm 1$. The system-bath interaction is fully characterized by the spectral density,

$$\begin{aligned} J(\omega) &= \frac{\pi}{2}\sum_k \frac{c_k^2}{\omega_k}\delta(\omega - \omega_k) \\ &= \xi\omega e^{-\omega/\omega_c}, \end{aligned} \tag{4.4}$$

which encodes the frequency-resolved coupling between the system and the oscillators that compose the bath. The second line in Eq. (4.4) corresponds to the often used Ohmic form for the spectral density [1] with an exponential cutoff. Here, ω_c is the cutoff frequency, which determines the correlation time for the bath at finite temperature. The Kondo parameter, ξ, describes the strength of the system-bath coupling and is proportional to the reorganization energy, $\lambda = \xi\omega_c/\pi = \pi^{-1}\int_0^\infty d\omega\ J(\omega)/\omega$, which represents energy dissipated after the system makes a Frank-Condon transition.

Mori-type GQME

As established in Paper I, the Mori (as well as the Nakajima-Zwanzig) approach stems from the generalized Mori-Zwanzig-Nakajima equation of motion for the propagator,

$$\begin{aligned}\frac{d}{dt}e^{i\mathcal{L}t} = ie^{i\mathcal{L}t}\mathcal{P}\mathcal{L} + i\mathcal{Q}e^{i\mathcal{L}\mathcal{Q}t}\mathcal{L} \\ - \int_0^t d\tau\ e^{i\mathcal{L}(t-\tau)}\mathcal{P}\mathcal{L}\mathcal{Q}e^{i\mathcal{L}\mathcal{Q}\tau}\mathcal{L},\end{aligned} \tag{4.5}$$

where $\mathcal{P}$ is the projection operator, which consists of the dynamical operators whose correlations we seek, and $\mathcal{Q} = 1 - \mathcal{P}$ is the complementary projection operator.

For ECFs, the Mori-type projector commonly takes the form,

$$\mathcal{P} = \frac{|\mathbf{A})(\mathbf{A}|}{(\mathbf{A}|\mathbf{A})}, \tag{4.6}$$

where the vector $\mathbf{A}$ consists of an operator A and its time derivative $\dot{A} = i\mathcal{L}A$, which ensures the idempotency of the projection operator [71, 106, 142, 143]. Instead of taking this approach, we employ a projector that recovers the symmetrized spin correlation functions for the SB model. Hence, we take $\mathbf{A}$ to consist of the Pauli matrices, σ_i, where $i \in \{x, y, z\}$, and define the inner product as,

$$(\boldsymbol{\sigma}|\mathcal{O}|\boldsymbol{\sigma})_{nm} \equiv \frac{1}{2}\mathrm{Tr}\Big[\rho\{\sigma_n, (\mathcal{O}\sigma_m)\}\Big], \tag{4.7}$$

where $\{A, B\} = AB + BA$ is the anticommutator, $\rho = e^{-\beta H}/\mathrm{Tr}[e^{-\beta H}]$ is the canonical density operator, and $\beta = [k_B T]^{-1}$ is the inverse thermal energy. Using the components of the projection operator to close Eq. (4.5) from both sides, we obtain the Mori-type GQME,

$$\frac{d}{dt}\mathcal{C}(t) = \mathcal{C}(t)\dot{\mathcal{C}}(0) - \int_0^t d\tau\ \mathcal{C}(t-\tau)\mathcal{K}(\tau), \tag{4.8}$$

where $\mathcal{C}_{nm}(t) = \mathrm{Tr}[\rho\{\sigma_n, \sigma_m(t)\}]/2 \equiv \mathrm{Re}\langle\sigma_n(0)\sigma_m(t)\rangle$ is the symmetrized or real part of the correlation function for the Pauli spin operators. The memory kernel takes the following form

$$\mathcal{K}(t) = (\boldsymbol{\sigma}|\mathcal{L}\mathcal{Q}e^{i\mathcal{Q}\mathcal{L}t}\mathcal{Q}\mathcal{L}|\boldsymbol{\sigma}). \tag{4.9}$$

Given the difficulties associated with treating the dynamics required by the projected propagator in Eq. (4.9), we follow Shi and Geva [93] employ the Dyson decomposition,

$$e^{(A+B)t} = e^{At} + \int_0^t ds\ e^{As}Be^{(A+B)(t-s)} \tag{4.10}$$

$$= e^{At} + \int_0^t ds\ e^{(A+B)s}Be^{A(t-s)} \tag{4.11}$$

$$\tag{4.12}$$

to obtain the $\mathcal{Q}$-forward (f) and $\mathcal{Q}$-backward (b) self-consistent expansions of the memory kernel,

$$\mathcal{K}(t) = \mathcal{K}^{(1)}(t) + \int_0^t d\tau\ \mathcal{K}(t-\tau)\mathcal{K}^{(3f)}(\tau), \tag{4.13}$$

$$= \mathcal{K}^{(1)}(t) + \int_0^t d\tau\ \mathcal{K}^{(3b)}(t-\tau)\mathcal{K}(\tau), \tag{4.14}$$

where the normally evolved auxiliary kernels

$$\mathcal{K}^{(1)}(t) = (\boldsymbol{\sigma}|\mathcal{L}\mathcal{Q}e^{i\mathcal{L}t}\mathcal{Q}\mathcal{L}|\boldsymbol{\sigma}), \tag{4.15}$$

$$\mathcal{K}^{(3f)}(t) = -i\ (\boldsymbol{\sigma}|e^{i\mathcal{L}t}\mathcal{Q}\mathcal{L}|\boldsymbol{\sigma}), \tag{4.16}$$

$$\mathcal{K}^{(3b)}(t) = -i\ (\boldsymbol{\sigma}|\mathcal{L}\mathcal{Q}e^{i\mathcal{L}t}|\boldsymbol{\sigma}), \tag{4.17}$$

can be obtained via direct simulation. For more details about the derivation, we refer the reader to Ref. [104].

As discussed in the first paper of this series [104], different closures may lead to different results when using approximate dynamics to calculate the auxiliary kernels. For that reason we also explore the effect of the three additional closures that selectively replace the action of the Liouvillian with time-derivatives. For completeness, these alternative closures are reproduced below. In the first set, we replace the action of the Liouvillian acting on operators that require dynamic sampling with the time-derivative, such that

$$\mathcal{K}_1^{(1)}(t) = \dot{\mathcal{K}}^{(3b)}(t) - \mathcal{K}^{(3b)}(t)\dot{\mathcal{C}}(0), \tag{4.18}$$

$$\mathcal{K}_1^{(3b)}(t) = \mathcal{K}^{(3b)}(t), \tag{4.19}$$

$$\mathcal{K}_1^{(3f)}(t) = -\dot{\mathcal{C}}(t) + \mathcal{C}(t)\dot{\mathcal{C}}(0). \tag{4.20}$$

The second type replaces the action of the Liouvillian on static operators with the time derivative,

$$\mathcal{K}_2^{(1)}(t) = \dot{\mathcal{K}}^{(3f)}(t) - \dot{\mathcal{C}}(0)\mathcal{K}^{(3f)}(t), \tag{4.21}$$

$$\mathcal{K}_2^{(3b)}(t) = -\dot{\mathcal{C}}(t) + \dot{\mathcal{C}}(0)\mathcal{C}(t), \tag{4.22}$$

$$\mathcal{K}_2^{(3f)}(t) = \mathcal{K}^{(3f)}(t). \tag{4.23}$$

The final type replaces all Liouvillian operators with time derivatives,

$$\mathcal{K}_3^{(1)}(t) = -\ddot{\mathcal{C}}(t) + \{\dot{\mathcal{C}}(t), \dot{\mathcal{C}}(0)\} - \dot{\mathcal{C}}(0)\mathcal{C}(t)\dot{\mathcal{C}}(0), \tag{4.24}$$

$$\mathcal{K}_3^{(3b)}(t) = \mathcal{K}_2^{(3b)}(t), \tag{4.25}$$

$$\mathcal{K}_3^{(3f)}(t) = \mathcal{K}_1^{(3f)}(t). \tag{4.26}$$

It bears repeating that *all* closures presented above are permitted by quantum mechanics and, when exact methods are used to calculate the auxiliary kernels, the memory kernels

and GQME dynamics produced will be equivalent, regardless of the closure. However, as was shown in the nonequilibrium case [104], the memory kernels and GQME dynamics obtained from auxiliary kernels calculated via approximate schemes can differ from each other, depending on the closure. Explicit expressions for the various closures in the context of the SB model can be found in Appendix 4.B.

4.3 Results

As in the first paper of this series [104], we employ the Ehrenfest method to calculate the auxiliary kernels necessary for the extraction of the memory kernels. The Ehrenfest approach is a simple quasi-classical scheme where the system (bath) evolves in the mean field of the bath (system). While most implementations of the Ehrenfest method (and other low-level quasi- and semi-classical theories such as the surface hopping [63, 64] and linearized semiclassical initial value representation schemes [65–67] (LSC-IVR) use approximate forms for the fully correlated Boltzmann factor [65, 159–161], we employ a numerically exact representation which relies on the path integral approach developed in Ref. [162]. The importance of the exact rendering of the canonical density operator will become evident in Sec. 4.3. Within this path integral framework, it is possible to produce expressions for the canonical distribution that increase in accuracy with the number of path integral slices, N, used. The number of path integral steps taken in the rendering of a given realization of ρ is determined by the number of slices necessary for the convergence of static and dynamic data as a function of N. Details regarding the path integral approach to the canonical density are included in Appendix 4.A, and those regarding the implementation of the Ehrenfest method

in Appendix 4.B.

The protocol for the extraction of $\mathcal{K}(t)$ can be summarized as follows. Using the approximate auxiliary kernels obtained via the Ehrenfest scheme, we solve Eqs. (4.13) and (4.14) iteratively until the relative error $R.E.$ is negligible, i.e., $R.E. < 10^{-10}$, where $R.E. = \max[\text{abs}[\mathcal{K}_{n+1}(t) - \mathcal{K}_n(t)]]$ is the maximum absolute difference between two subsequent iterations of the memory kernel. With a converged solution for the memory kernel, we numerically integrate Eq. (4.8) using a second-order Runge-Kutta procedure, subject to the appropriate initial conditions, namely $\mathcal{C}_{ii}(t = 0) = 1$. To assess the viability of the GQME+MFT procedure in the equilibrium context we compare the solution of Eq. (4.8) using the self-consistently extracted $\mathcal{K}(t)$ to numerically exact results for $\mathcal{C}_{zz}(t)$ for the SB model with an Ohmic spectral density. We further specify that, in the same vein as previous implementations of the GQME coupled to the self-consistent solution of the memory kernel [93–104, 106], the finite lifetime of the memory kernel is explicitly included in the GQME evolution algorithm as a cutoff time, τ_c, beyond which the memory kernels is set to zero. In practice, τ_c is identified as any time point in the stability plateau corresponding to the range of time during which the memory kernel ceases to influence the GQME dynamics. When numerically exact methods are used to obtain the auxiliary kernels, this stability plateau is infinitely long.[1] Conversely, when approximate methods are used instead, the limited accuracy of the underlying method may cause the stability plateau to be finite or, in extreme

[1]There are problems where the memory kernels never decays to zero. A clear example of this is the case of a SB model where the bath consists of *one* oscillator, where the persistent quantum coherence results in a memory kernel that never decays. For problems where decoherence and dissipation are expected to be significant, a non-decaying memory kernel is a sign that the projection operator has to be chosen differently. Clearly, the GQME formalism cannot provide any advantages with respect to computational efficiency for cases where the memory kernel never decays.

cases, nonexistent. In all cases studied in this work, a well-defined stability plateau exists and all cutoff times for the memory kernels are specified.

Boosts in Efficiency and Accuracy

For nonequilibrium averages, the GQME+semiclassics approach has been shown to be uniformly beneficial in reducing the cost of the dynamics via short-lived memory kernels and generally advatageous in correcting approximate dynamics, especially for biased systems coupled weakly to the bath [93–104, 106]. In the following, we show that similar benefits can be reaped in the equilibrium case.

Before continuing to the ECFs, we note the almost Markovian appearance of the memory kernels shown in Fig. 4.1. Panels (a) and (b) correspond to an unbiased ($\varepsilon = 0$) system coupled to a moderately fast bath ($\omega_c = 2.5$), and panels (c) and (d) to a strongly biased system ($\varepsilon = -2$) coupled to a fast bath ($\omega_c = 15$). In both cases shown, the diagonal components of the memory kernel $\mathcal{K}_{xx}(t)$ and $\mathcal{K}_{yy}(t)$ are strongly peaked as $t = 0$ and decay quickly to zero (see panels (a) and (c)). Interestingly, the off-diagonal components $\mathcal{K}_{xy}(t)$ and $\mathcal{K}_{yx}(t)$ behave very differently; panel (b) shows memory kernels that fluctuate around zero with a small amplitude, while panel (d) displays a high-amplitude short-time peak, which indicates that the off-diagonal components of the memory kernel play a large role in the relaxation of the ECF dynamics for systems characterized by a large bias. Also, consistent with our expectations, the realization of the SB model in panels (a) and (b) characterized by a moderately fast bath ($\omega_c = 2.5$) exhibits a longer-lived memory kernel than the realization in panels (c) and (d) which corresponds to a faster bath ($\omega_c = 15$). Figs. 4.2(a) and 4.3(d) present the GQME+MFT dynamics obtained from the memory kernels in panels (a) and

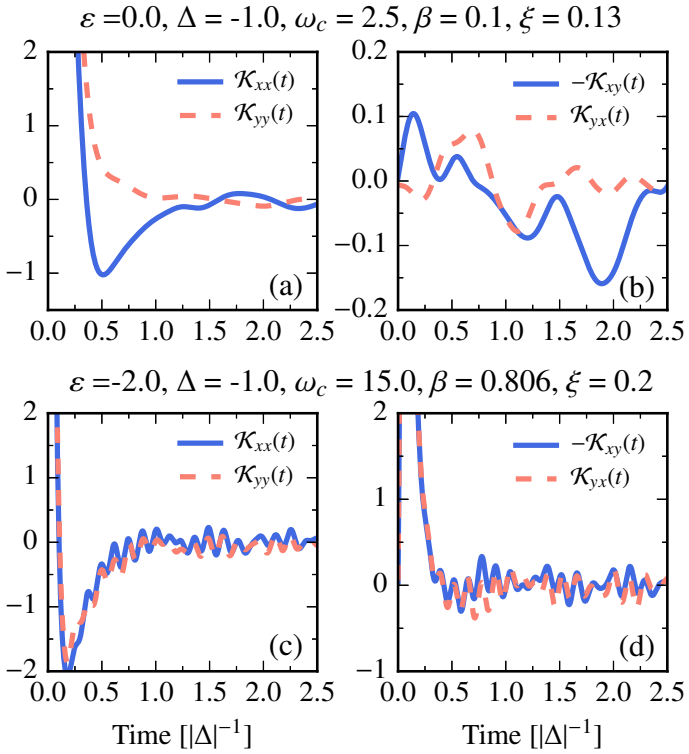

Figure 4.1: Memory kernels obtained using the $cf0$ closure for two realizations of the SB model. For panels (a)–(b), $\alpha = 1$ and for (c)–(d), $\alpha = -1$. By symmetry requirements, all other components of the memory kernel are identically zero.

(b), and (c) and (d), respectively.

As Figs. 4.2 and 4.3 illustrate, the advantages afforded by the GQME formalism for nonequilibrium averages are transferable to equilibrium situations. For example, Fig. 4.2 illustrates that in the weak coupling regime shown in panels (a) and (b), the GQME approach is able to easily reproduce the already accurate dynamics produced via the Ehrenfest method. In these instances, the GQME+MFT scheme also affords boosts in efficiency, since the memory kernel cutoffs used to recover the appropriate dynamics were $\tau_c = 0.5$ and $\tau_c = 1.0$

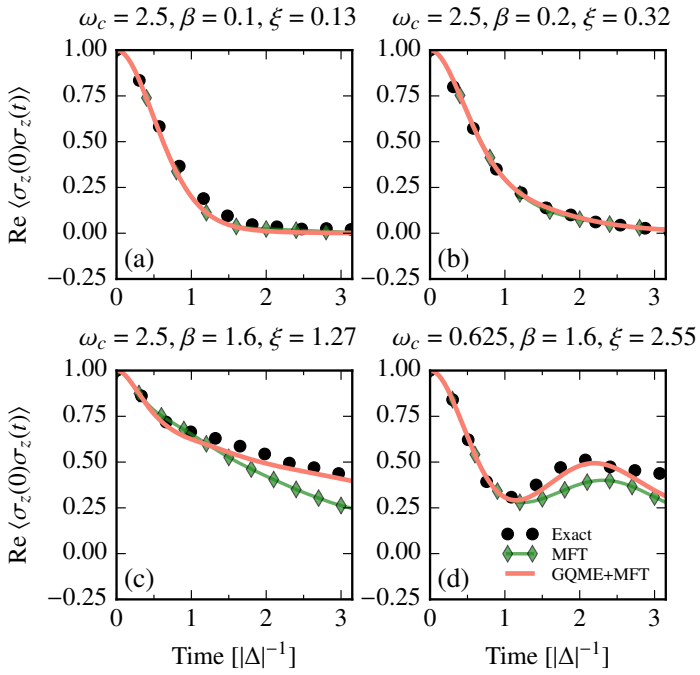

Figure 4.2: Comparison of $\mathcal{C}_{zz}(t) = \text{Re}\ \langle\sigma_z(0)\sigma_z(t)\rangle$ obtained from the $cf0$ memory kernels for the unbiased SB model ($\varepsilon = 0$) with $\Delta = -1$ and $\alpha = 1$. Converged representations of the canonical density required $N = 0, 1, 5, 6$ path integral slices for panels (a)–(d), respectively. Exact results are obtained from Ref. [151].

for panels (a) and (b), respectively. But the limited applicability of the Ehrenfest method can also lead to dynamics that significantly deviate from the exact results. Indeed, by virtue of its mean-field character, the Ehrenfest scheme is known to fail for cases where the system-bath coupling is large, as shown in panels (c) and (d). Here the Ehrenfest scheme leads to overly fast relaxation. In contrast, the GQME+MFT method is able to produce dynamics that are in notable agreement with the numerically exact results, albeit at a similar computational cost as the direct Ehernfest calculation for panels (c) and (d), where $\tau_c = 3.0$.

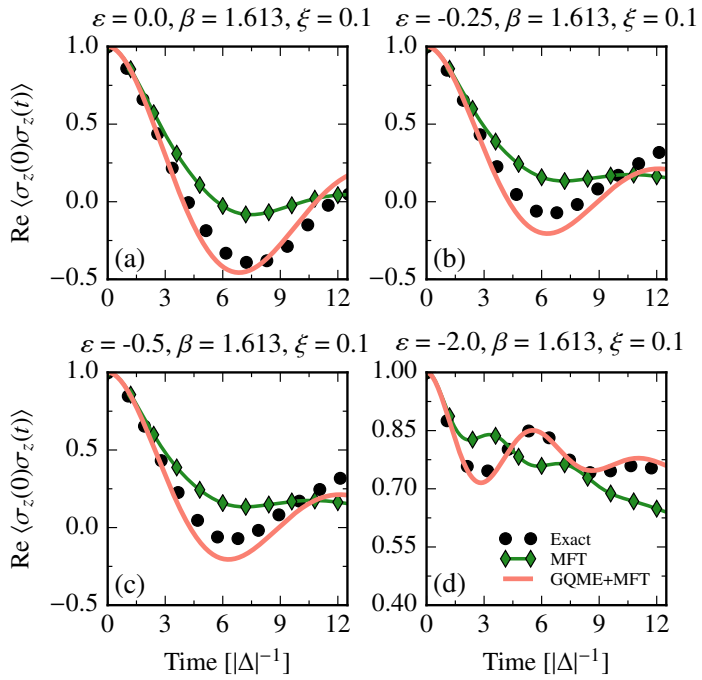

Figure 4.3: Comparison of $\mathcal{C}_{zz}(t) = \mathrm{Re}\,\langle\sigma_z(0)\sigma_z(t)\rangle$ obtained using the $cf0$ memory kernels for the biased SB model with $\Delta = -1$, $\omega_c = 14.0$, and $\alpha = -1$. For all panels (a)-(d) $N = 2$ path integral slices were taken to obtain a converged representation of the canonical density. Exact results are obtained from Ref. [152].

Further, it is remarkable that even for unbiased cases, which has been shown to be of little interest for nonequilibrium dynamics, the GQME+semiclassics approach can offer marked improvements.

The approximations that underlie the Ehrenfest approach also lead to incorrect dynamics in other parameter regimes. For instance, the classical treatment of the bath implies that the Ehrenfest scheme is most accurate for slow baths where quantum effects are negligible [62]. In addition, the mean-field character and classical treatment of the bath in the Ehren-

fest framework results in the breaking of detailed balance, a problem that becomes most pronounced in the dynamics of biased systems [141, 163]. Cases that violate the validity of these approximations for the Ehrenfest method are also those where the improvements afforded by the GQME+MFT approach are most dramatic, as Fig. 4.3 illustrates. Given the above considerations, it is not surprising that the Ehrenfest method can only qualitatively capture the relaxation of the ECF, leading to overly fast relaxation and, in the case of the strongly biased system in panel (d), leading to the wrong oscillation frequency. On the other hand, the dynamics produced by the GQME+MFT approach are in remarkable agreement with the numerically exact results. Hence, as in the nonequilibrium case, the present method represents an important tool that has the potential to correct the semiclassical dynamics of systems characterized by nonzero bias or coupling to fast baths.

One question continues to emerge from the continued success of the GQME+semiclassics formalism: where do such improvements in accuracy over bare approximate dynamics come from? In the first paper of this series [104] we conjectured that the source was, at least to some extent, the *exact* sampling of *distinct* initial conditions required for the calculation of the auxiliary kernels. As our added emphasis indicates, this improvement appears to rely on two different factors. The latter, in the nonequilibrium case, was identified as the "correction terms" arising from the Wigner transform of the product of the bath part of the system-bath interaction with the bath distribution. In the nonequilibrium case, this operator takes the form $\zeta^W_{noneq} = -\alpha \sum_k c_k P_k \tanh(\beta\omega_k/2)/\omega_k$ (see Eq. (D6) in Appendix D of Ref. [104]). Our treatment of the equilibrium problem produces the analogous bath operator given by Eq. (4.45) in Appendix 4.B). The inclusion of the correlation functions that require the sampling of this operator in the auxiliary kernels (see Eqs. (4.63)-(4.67)) is indeed

necessary to obtain the improved dynamics shown in Figs. 4.2 and 4.3. The importance of the second factor in the context of thermal equilibrium can only be confirmed by using representations of the canonical density that can be made arbitrarily accurate. It bears noting that, for realizations of the SB model where the system and bath are weakly coupled and at high temperature, the canonical distribution can be captured by a simple factorization approximation implemented earlier in the literature [65]. The two simplest approximations consist of rewriting the Boltzmann factor as simple products of system and bath operators, e.g., $e^{-\beta H} \approx e^{-\beta H_S} e^{-\beta H_B}$ and $e^{-\beta H} \approx e^{-\beta (H_B + H_{SB})/2} e^{-\beta H_S} e^{-\beta (H_B + H_{SB})/2}$, which we refer to in our path integral notation as containing $N = 0$ and $N = 1$ path integral slices, respectively. For cases where the system-bath coupling is strong (large ξ) or temperatures are low (large β), the Boltzmann factor can no longer be captured by such crude approximations. In these cases, we adopt the path integral scheme developed in Ref. [162] to obtain highly accurate expressions for the canonical density, ρ.

In Fig. 4.4 two sets of dynamics are presented. Panels (a) and (c) correspond to the direct Ehrenfest treatment of $C_{zz}(t)$ for two different realizations of the SB model using an increasing number, N, of path integral slices. As is evident in panel (a), which corresponds to a case with strong system-bath coupling ($\xi = 2.55$) and moderate to low temperatures ($\beta = 1.6$), a large number of path integral steps ($N = 6$) is required to achieve convergence. Conversely, the high temperature ($\beta = 0.806$) and weak coupling ($\xi = 0.2$) case presented in panel (c) only requires two path integral steps ($N = 2$) to achieve convergence. More importantly, panels (a) and (c) illustrate that the accurate representation of the Boltzmann factor can significantly improve the dynamics produced via the *bare* Ehrenfest method. Panels (b) and (d) present the GQME+MFT dynamics obtained using the different approximations for

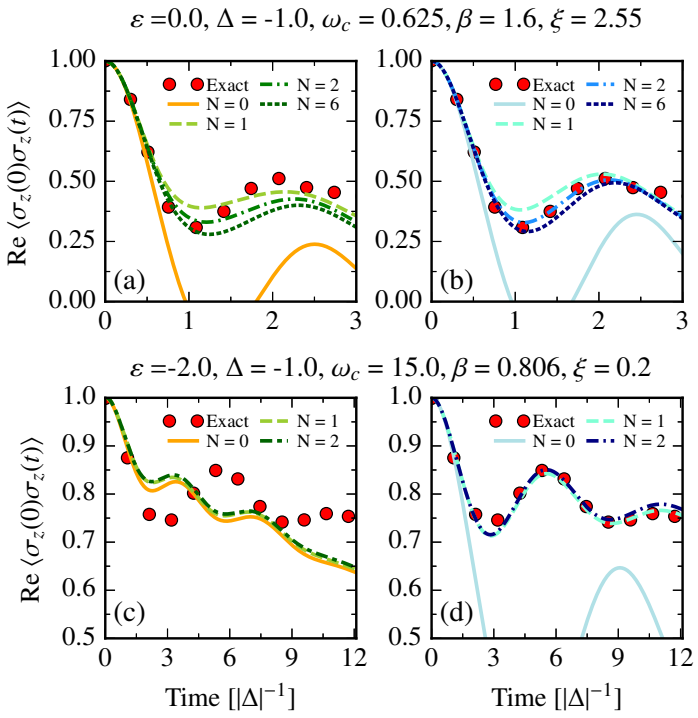

Figure 4.4: Convergence properties of the direct Ehrenfest and GQME+MFT approaches with respect to the number of path integral slices used in constructing the canonical density operator. Panels (a) and (c) correspond to direct Ehrenfest dynamics and panels (b) and (d) correspond to the analogous the GQME+MFT results. Further, for panels (a) and (b) $\alpha = 1$, while for panels (c)-(d) $\alpha = -1$.

ρ. As the figure suggests, the accurate rendering of the canonical distribution is critical in obtaining improved accuracy via the GQME framework. Moreover, the sensitive dependence of the improvements afforded by the GQME formalism on the accurate rendering of ρ lends credence to our conjecture [104] that the *exact* sampling of *distinct* initial conditions required by the auxiliary kernels is largely responsible for the improvements in accuracy afforded by the GQME framework.

Memory Kernel Closures

As was demonstrated in the first paper of this series [104], use of different closures can strongly influence the quality of the GQME+semiclassics dynamics for nonequilibrium averages. Here we show that a similar dependence also exists in the equilibrium case. In particular we determine that, while the differences between the forward and backward closures are minor, the forward closures outperform their backward counterparts. In the following analysis of the closures that employ numerical time derivatives ($cf1$, $cf2$, and $cf3$), we provide further numerical support for the analytical proofs in Ref. [106] regarding closures that can be written in terms of the original ECF and its time derivatives.

Initially we focus on the differences between dynamics produced via the $\mathcal{Q}$-forward and $\mathcal{Q}$-backward closures, presented in Fig. 4.5. Taking the zeroth order closures $cf0$ and $cb0$, which do not replace the action of the Liouvillian with numerical derivatives, as representative of the differences between the forward and backward closures, it is clear that the forward closure performs slightly better than the backward closure. This manifests in the difference between the GQME results in panels (a) and (b). The reason for this discrepancy, however, is not well understood and will require further analysis beyond the scope of the present work. These

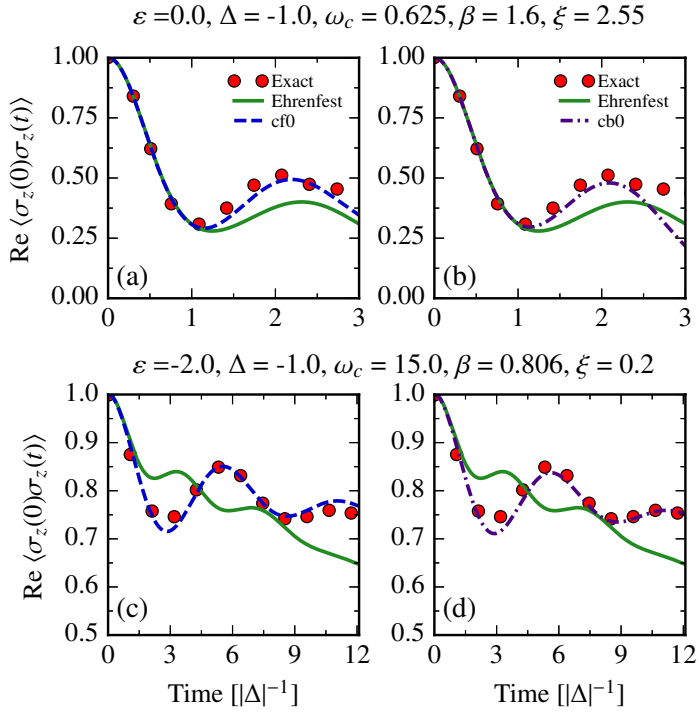

Figure 4.5: Comparison of $\mathcal{C}_{zz}(t) = \text{Re}\ \langle\sigma_z(0)\sigma_z(t)\rangle$ obtained using the $\mathcal{Q}$-forward and $\mathcal{Q}$-backward $cf0$ and $cb0$ closures for two realization of the SB model. For panels (a)-(b), $\alpha = 1$, while for panels (c)-(d) $\alpha = -1$.

differences notwithstanding, both the $cf0$ and $cb0$ closures clearly yield dynamics that are significantly more accurate than the bare quasiclassical results.

Restricting our attention to the forward closures, the kernels produced via the various closures can shed light on the factors that lead to distinct GQME dynamics. As panels (a)-(d) of Fig. 4.6 suggest, the closures can be subdivided into two main sets which yield similar memory kernels: the first group consists of closures $cf0$ and $cf1$, while the second of $cf2$ and $cf3$. The main difference between the kernels produced by these two groups is

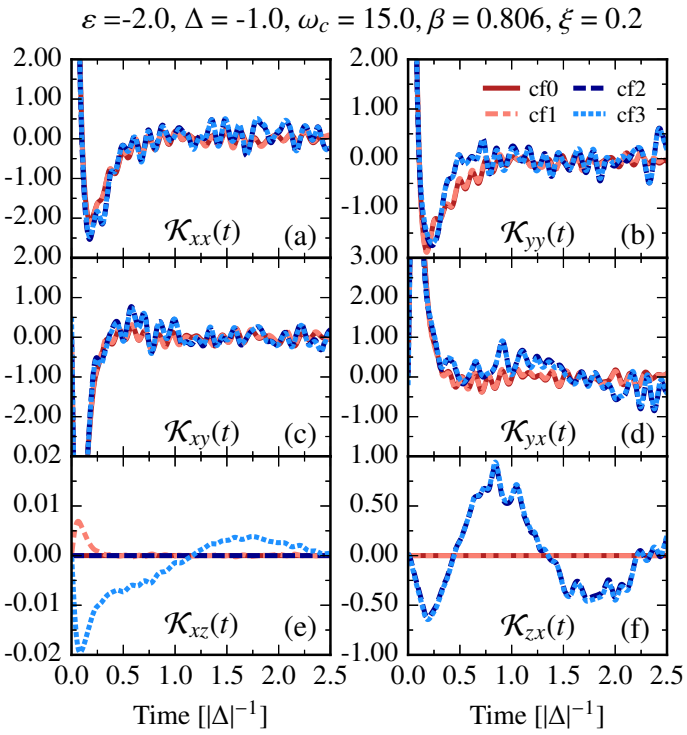

Figure 4.6: Comparison of the memory kernels obtained using the $\mathcal{Q}$-forward closures $cf0$, $cf1$, $cf2$, and $cf3$ for the SB model with $\alpha = -1$. Note that the $cf1$, $cf2$, and $cf3$ violate the symmetry requiment that stipulates that all memory kernels crossed with σ_z must be identically zero.

clearest at intermediate times. Before individually considering the kernel elements in panels (e) and (f), it is noteworthy that all components of the memory kernel that depend on σ_z, e.g., $\mathcal{K}_{xz}(t)$ and $\mathcal{K}_{zx}(t)$, must be zero by symmetry requirements.[2] In light of this, it is apparent that the $cf1$ closure leads to a violation of this symmetry requirement for $\mathcal{K}_{xz}(t)$ (and $\mathcal{K}_{xz}(t)$, not shown) in panel (e), while the $cf2$ closure leads to a similar violation for $\mathcal{K}_{zx}(t)$ (and $\mathcal{K}_{zy}(t)$, not shown) in panel (f). As the amplitudes of the memory kernels in panels (e) and (f) indicate, this violation is milder for $cf1$ than for $cf2$. The worst of these closures seems to be $cf3$, for which all z-components of the memory kernel are nonzero. To understand the source of these violations, it is sufficient to consider that while the symmetry requirements are satisfied via the analytical application of $\mathcal{QL}|\sigma)$ and $(\sigma|\mathcal{LQ}$, replacement of the Liouvillian with the numerical time derivative does not ensure this strict requirement. On the other hand, the severity of this artificial nonzero behavior cannot be estimated *a priori*.

The consequences of the differences among the different kernels can be best appreciated in the dynamics they produce, which are shown in Fig. 4.7. As panels (a) and (b) suggest, the $cf0$ and $cf1$ closures lead to the dynamics that most closely reproduce the exact results. Further, the exceptional agreement between the dynamics produced via the $cf0$ and $cf1$ closures indicate that the slight symmetry violation in Fig. 4.6(c) does not introduce serious errors in the GQME results. A similar conclusion can be drawn from the dynamics produced by closures $cf2$ and $cf3$, which are able to reproduce the Ehrenfest results to within graphical accuracy. Importantly, this agreement provides additional numerical proof for the analytical

[2]This becomes clear upon considering that $\mathcal{K}(t) = \mathcal{Y}^T(\delta V_B\sigma|e^{i\mathcal{QL}t}|\delta V_B\sigma)\mathcal{Y}$ and that the components of the static transformation matrices $\mathcal{Y}^T_{zi} = 0 = \mathcal{Y}^T_{iz}$, where $i \in \{x, y, z\}$.

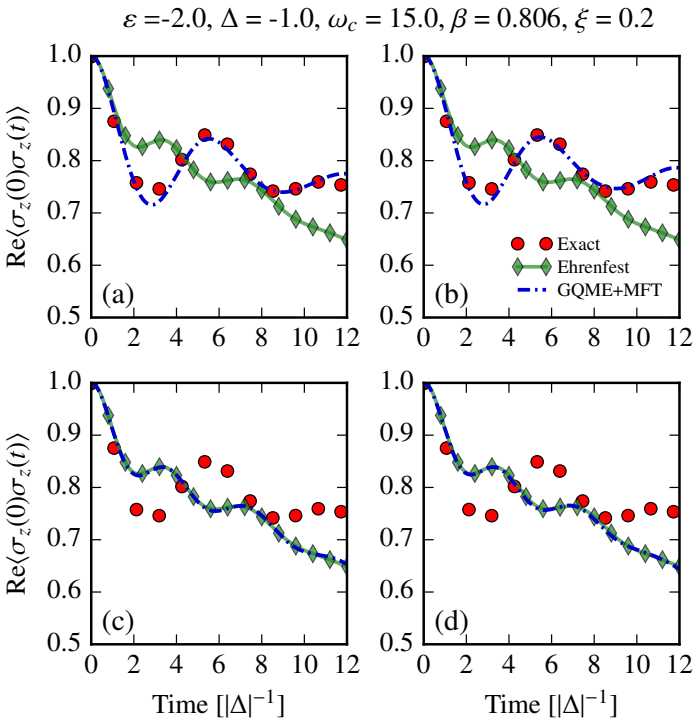

Figure 4.7: Comparison of $\mathcal{C}_{zz}(t) = \text{Re}\ \langle\sigma_z(0)\sigma_z(t)\rangle$ obtained using the $\mathcal{Q}$-forward and $\mathcal{Q}$-backward $cf0$ and $cb0$ closures for two realization of the SB model. For panels (a)-(b), $\alpha = 1$, while for panels (c)-(d) $\alpha = -1$.

arguments put forth in Ref. [106]. Specifically, because the auxiliary kernels for closure $cf3$ (and $cb3$) can be written in terms of the original ECF in Eq. (4.8) and its time derivatives, the memory kernel obtained using this closure *must* recover the bare Ehrenfest result. Because the $cf2$ (and $cb2$) closure also reproduces the Ehrenfest dynamics, as was the case in the nonequilibrium problem [104], it is clear that the Ehrenfest method permits replacing the action of the Liouvillian operator acting on a dynamically evolved operator with its time derivative. In turn, the fact that the $cf0$ and $cf1$ (and $cb0$ and $cb1$) closures yield GQME

dynamics that are distinct from the Ehrenfest results is consistent with the observation that the Ehrenfest procedure is not ensemble conserving. Nevertheless, the arguments in Ref. [106] do not explain the improvements afforded by the $cb0$ and $cb1$ closures. Instead, we again emphasize that the most likely reason for the improvement afforded by the $cf0$ and $cf1$ closures lies in the *exact* sampling of *distinct* bath operators alluded to in Sec. 4.3.

4.4 Conclusions

In this paper we have extended the GQME+MFT method introduced in the first paper of this series [104] to treat ECFs within the context of the Mori formalism. As Ref. [104] and the present work demonstrate, the Mori-based formulation furthered here provides a flexible framework to accurately study problems both in and out of equilibrium for SB-type models. We further emphasize that this approach is general and can be easily generalized to arbitrarily complex systems and dynamical quantities.

In the same spirit as earlier work on nonequilibrium dynamics [93–104, 106], we have demonstrated that equilibrium memory kernels for SB model can be short-lived in comparison to the ECF lifetime. Indeed, it is possible to say that *all* impurity-type systems where the bath consists of a large number of modes with a broad distribution of energies have short-lived memory kernels, as long as the projection operator includes all system states. We have also shown that, as in the nonequilibrium case, the GQME+semiclassics approach is capable of yielding impressive improvements in computational efficiency and accuracy over direct application of bare quasi- and semi-classical methods. Consequently, at least for these types of models, we foresee that the GQME approach can become an invaluable tool for

obtaining highly accurate nonequilibrium *and* equilibrium dynamics at a lower computational cost than would be necessary with conventional methods that go well beyond SB-type models, including the dynamics of liquid state systems with no system-bath distinction.

Via a systematic analysis of the dependence of the GQME dynamics on the kernel closures, we have further confirmed the analytical arguments posited in Ref. [106]. Specifically, the results obtained from the $cf3$ and $cb3$ closures, which reproduce the direct Ehrenfest dynamics, confirm the proof presented in Ref. [106] which states that when the auxiliary kernels can be written in terms of the original ECF and its time derivatives, the GQME results will be equivalent to those arising from direct application of the dynamical method. The fact that the $cf2$ and $cb2$ closures also reproduce the Ehrenfest results is in agreement with the the observation that the numerical time derivative of a correlation function is equivalent to the action of the Liouvillian on the dynamically sampled operator in the Ehrenfest method. We have also demonstrated that the $cf0$ closure yields the most accurate dynamics over a wide region of parameter space. Further, although the $cb0$ closure has been shown to produce slightly less accurate dynamics for some sets of parameters, it also affords a significant improvement over the bare mean-field dynamics, as do the $cf1$ and $cb1$ closures, despite the slight violation of the symmetry requirement that requires the memory kernels involving σ_z to be zero. The distinct results obtained from the $cf0$, $cb0$, $cf1$, and $cb1$ closures has also been shown to be consistent with the fact that the Ehrenfest method is *not* ensemble-conserving [106].

To conclude, we emphasize that the Mori formulation presented in this work and Ref. [104] is equally applicable to impurity-type models like the SB model and systems such as spin and fermion lattice models [5–7], and quantum fluids [8, 9, 72, 135]. In future papers,

we explore the extension of the Mori framework to multiple-time correlation functions and systems coupled to arbitrary baths as well as problems where the system-bath distinction is absent.

Appendix

4.A Path integral treatment of the Wigner transformed canonical density operator

After a partial Wigner transform with respect to the bath degrees of freedom, it is possible to write the system components of the canonical density operator as follows [162],

$$\begin{aligned}\rho^W_{a,b} &= [2\pi]^{-f} \int d\mathbf{s}\; e^{-i\mathbf{p}\cdot\mathbf{s}/\hbar} \langle \mathbf{x}+\mathbf{s}/2| \langle a| \rho |b\rangle |\mathbf{x}-\mathbf{s}/2\rangle \\ &\equiv N_{ab} \cdot \mathcal{R}^W_{a,b}(\mathbf{x},\mathbf{p}),\end{aligned} \tag{4.27}$$

where $\rho = e^{-\beta H}/\mathrm{Tr}[e^{-\beta H}]$, $a, b \in \{0, 1\}$ correspond to the two system states of the SB model, N_{ab} is temperature dependent normalization constant, and $\mathcal{R}^W_{a,b}(\mathbf{x},\mathbf{p})$ is a bath operator of unit partial trace, i.e., $\int d\mathbf{x}d\mathbf{p}\; \mathcal{R}^W_{a,b}(\mathbf{x},\mathbf{p}) = 1$, which can be interpreted as the bath distribution function. We henceforth drop the dependence of the bath distribution function on the bath coordinates and momenta, $(\mathbf{x},\mathbf{p})$, for notational clarity.

To obtain expressions for N_{ab} and $\mathcal{R}^W_{a,b}$ we follow the numerically exact framework presented in Ref. [162], which relies on the path integral expansion of the Boltzmann factor. This expansion employs the Trotter factorization, allowing us to rewrite the full Boltzmann

factor as an N-membered product of basic path integral units,

$$e^{-\beta H} \approx [e^{-\beta(H_B+H_{SB})/2N} e^{-\beta H_S/N} e^{-\beta(H_B+H_{SB})/2N}]^N. \tag{4.28}$$

Rigorously, this approximation becomes exact in the limit of $N \to \infty$, but in practical calculations convergence is achieved with a small N.

By substituting Eq. (4.28) into Eq. (4.27), introducing resolutions of the identity $\mathbf{1}_S = \sum_a |a\rangle \langle a|$ and $\mathbf{1}_B = \int d\mathbf{q} \, |\mathbf{q}\rangle \langle \mathbf{q}|$ for the system and bath subspaces, respectively, and integrating over the bath degrees of freedom one can obtain expressions for N_{ab} and $\mathcal{R}^W_{a,b}$. While the previous procedure formally eliminates the dependence on the bath degrees of freedom introduced with the resolutions of the identity, the same cannot be said of the system degrees of freedom. In fact, it is worthwhile to note that the number of paths grows exponentially with the number of path integral steps, and that each path can be associated with a sequence of indices that in indicate the electronic states visited along said path. To illustrate this point, consider the simpler case of applying the path integral formalism to the Boltzmann factor corresponding to the isolated two-level system:

$$\langle k_N | \, e^{-\beta H_S} \, | k_0 \rangle \approx \sum_{k_1,\ldots,k_{N-1}} \langle k_N | \, e^{-\beta H_S/N} \, | k_{N-1} \rangle \langle k_2 | \, e^{-\beta H_S/N} \, | k_1 \rangle \langle k_1 | \, e^{-\beta H_S/N} \, | k_0 \rangle \, , \tag{4.29}$$

where $k_n \in \{0, 1\}$ corresponds to the state used in the n^{th} path integral step of the expansion. For this decomposition, one may consider the path to consist of a string of numbers describing the identity of the states taken in the sequence, e.g., in an $N = 3$ expansion with the endpoints fixed, there are $4 (= 2^{N-1})$ such sequences, $\{k_3, 0, 0, k_0\}$, $\{k_3, 0, 1, k_0\}$, $\{k_3, 1, 0, k_0\}$, and $\{k_3, 1, 1, k_0\}$. In the following, we refer to the sum over the set $\{k_1, ..., k_{N-1}\}$ as the sum over paths.

4.A. PATH INTEGRAL TREATMENT OF THE WIGNER TRANSFORMED CANONICAL DENSITY OPERATOR

Before providing expressions for N_{ab} and $\mathcal{R}^W_{a,b}$, we provide a few definitions that render the notation simpler. We begin with the following basic definitions,

$$\begin{aligned} b_n^{(l)} &= -\langle k_n|\,\sigma_z\,|k_n\rangle\,\alpha c_l/\omega_l^2 \\ &= (-1)^{k_n}\alpha c_l/\omega_l^2, \end{aligned} \tag{4.30}$$

$$\theta_l = \frac{\beta\hbar\omega_l}{2N}, \tag{4.31}$$

$$\delta b_{nm}^{(l)} = b_n^{(l)} - b_m^{(l)}. \tag{4.32}$$

and the following path-independent quantities,

$$\gamma_p^{(l)} = \frac{\tanh(2\theta_l)}{\omega_l\eta_l}, \tag{4.33}$$

$$\gamma_x^{(l)} = \frac{\omega_l\nu_l}{\tanh(2\theta_l)}, \tag{4.34}$$

$$\eta_l = 1 - \frac{[\mathbf{A}_l^{-1}]_{1,1} - [\mathbf{A}_l^{-1}]_{1,N-1}}{\cosh^2(2\theta_l)}, \tag{4.35}$$

$$\nu_l = 1 - \frac{[\mathbf{A}_l^{-1}]_{1,1} + [\mathbf{A}_l^{-1}]_{1,N-1}}{\cosh^2(2\theta_l)}, \tag{4.36}$$

where $\mathbf{A}^{(l)}$ is a tridiagonal $N-1\times N-1$ matrix whose diagonal and off-diagonal entries are equal to 2 and $-\mathrm{sech}(2\theta_l)$, respectively.

A few quantities depend on the path taken in configuration space. These quantities, labeled by a tilde, take the following forms,

$$\tilde{\mathcal{S}}_{k_N,k_0} = \prod_{j=1}^{N}\langle k_j|\,e^{-\beta H_{ad}/N}\,|k_{j-1}\rangle\,, \tag{4.37}$$

$$\tilde{\boldsymbol{\delta}}^{(l)} = \frac{\mathbf{j}_l^T\cdot\mathbf{A}_l^{-1}}{\cosh(\theta_l)}, \tag{4.38}$$

$$\tilde{\mathbf{j}}_l = \begin{bmatrix} \Delta b_{21}^{(l)} - \Delta b_{10}^{(l)} \\ \Delta b_{32}^{(l)} - \Delta b_{21}^{(l)} \\ \vdots \\ \Delta b_{N,N-1}^{(l)} - \Delta b_{N-1,N-2}^{(l)} \end{bmatrix}, \tag{4.39}$$

$$\tilde{\kappa}_p^{(l)} = \begin{cases} -\frac{\omega_l}{2\tanh(2\theta_l)} \left[\frac{\cosh(\theta_l)}{\cosh(2\theta_l)} [(\Delta b_{N,N-1}^{(l)} + \Delta b_{1,0}^{(l)}) - (\tilde{\boldsymbol{\delta}}_{N-1}^{(l)} - \tilde{\boldsymbol{\delta}}_1^{(l)})] - \eta_l \Delta b_{N,0}^{(l)} \right] & : \quad N \geq 2, \\ -\frac{\omega_l}{\tanh(2\theta_l)} \left[\frac{\cosh(\theta_l)}{\cosh(2\theta_l)} \right] \Delta b_{1,0}^{(l)} [1 - \cosh(\theta_l)] & : \quad N = 1, \end{cases} \tag{4.40}$$

$$\tilde{\kappa}_x^{(l)} = \begin{cases} \frac{\cosh(\theta_l)}{2\cosh(2\theta_l)} \frac{[(\Delta b_{N,N-1}^{(l)} - \Delta b_{1,0}^{(l)}) - (\tilde{\boldsymbol{\delta}}_{N-1}^{(l)} + \tilde{\boldsymbol{\delta}}_1^{(l)})]}{\nu_l} - \frac{b_N^{(l)} + b_0^{(l)}}{2} & : \quad N \geq 2, \\ -\frac{b_N^{(l)} + b_0^{(l)}}{2} & : \quad N = 1, \end{cases} \tag{4.41}$$

$$\tilde{\Lambda}^{(l)} = \begin{cases} \frac{\omega_l}{4\tanh(2\theta_l)} \left[\frac{1+\cosh(2\theta_l)}{\cosh(2\theta_l)} \left[\sum_{j=1}^{N} [\tilde{\boldsymbol{\delta}} b_{j,j-1}^{(l)}]^2 - \frac{\tilde{\mathbf{j}}_l^T \cdot \mathbf{A}_l^{-1} \cdot \tilde{\mathbf{j}}_l}{\cosh(2\theta_l)} \right] \right. \\ \qquad -2\frac{\cosh(\theta_l)}{\cosh(2\theta_l)} \left[(\Delta b_{N,N-1}^{(l)} + \Delta b_{1,0}^{(l)}) - (\tilde{\boldsymbol{\delta}}_{N-1}^{(l)} - \tilde{\boldsymbol{\delta}}_1^{(l)}) \right] \Delta b_{N,0}^{(l)} \\ \qquad \left. -\left[\frac{\cosh(\theta_l)}{\cosh(2\theta_l)} \right]^2 \frac{[(\Delta b_{N,N-1}^{(l)} - \Delta b_{1,0}^{(l)}) - (\tilde{\boldsymbol{\delta}}_{N-1}^{(l)} + \tilde{\boldsymbol{\delta}}_1^{(l)})]^2}{\nu_l} + \eta_l [\Delta b_{N,0}^{(l)}]^2 \right] & : \quad N \geq 2, \\ \frac{\omega_l}{\tanh(2\theta_l)} \left[\frac{\cosh(\theta_l)}{\cosh(2\theta_l)} \right] [\Delta b_{1,0}^{(l)}]^2 [1 - \cosh(\theta_l)] & : \quad N = 1, \end{cases} \tag{4.42}$$

Using these definitions,

$$\mathcal{R}_{a,b}^W = \left[\prod_{l=1}^{F} \frac{\sqrt{\nu_l/\eta_l}}{\pi} \right] \sum_{\text{paths}} \frac{\tilde{W}_{a,b}}{\mathcal{W}_{a,b}} \prod_{l=1}^{F} \exp\Big[-\gamma_p^{(l)} (p_l + i\tilde{\kappa}_p^{(l)})^2 - \gamma_x^{(l)} (x_l + \tilde{\kappa}_x^{(l)})^2 \Big], \tag{4.43}$$

$$N_{ab} = \frac{\mathcal{W}_{a,b}}{\sum_a \mathcal{W}_{a,a}}, \tag{4.44}$$

where $\tilde{W}_{a\ldots b} = \tilde{\mathcal{S}}_{a,b} \exp[-\sum_l \tilde{\Lambda}^{(l)}]$, and $\mathcal{W}_{a,b} = \sum_{paths} \tilde{W}_{a,b}$.

Finally, in the following section, the Wigner transform of the product of ρ and $V_B = \alpha \sum_l c_l x_l$ will require the evaluation of the following operator,

$$\begin{aligned}\zeta &= \frac{1}{2\mathcal{R}^W_{a,b}} \frac{\partial \mathcal{R}^W_{a,b}}{\partial \mathbf{p}} \cdot \frac{V_B}{\partial \mathbf{x}} \\ &= -\alpha [\mathcal{R}^W_{a,b}]^{-1} \left[\prod_{l=1}^{F} \frac{\sqrt{\nu_l/\eta_l}}{\pi} \right] \sum_{\text{paths}} \frac{\tilde{W}_{a,b}}{\mathcal{W}_{a,b}} \Big[\sum_q c_q \gamma_p^{(q)} (p_q + i\tilde{\kappa}_p^{(q)}) \Big] \\ &\qquad \prod_{l=1}^{F} \exp\Big[-\gamma_p^{(l)} (p_l + i\tilde{\kappa}_p^{(l)})^2 - \gamma_x^{(l)} (x_l + \tilde{\kappa}_x^{(l)})^2 \Big].\end{aligned} \tag{4.45}$$

4.B Expressions for the Auxiliary kernels

We first introduce a notation based on static and dynamic matrices that facilitate the construction of the auxiliary kernels. Given the definition of the inner product in Eq. (4.7), one can easily verify that

$$(i\mathcal{Q}\mathcal{L})|\boldsymbol{\sigma}) = |\delta V_B \boldsymbol{\sigma}) \mathcal{Y}, \tag{4.46}$$

$$(\boldsymbol{\sigma}|(-i\mathcal{L}\mathcal{Q}) = \mathcal{Y}^T (\delta V_B \boldsymbol{\sigma}| \tag{4.47}$$

where $\mathcal{Y}_{nm} = -2\epsilon_{znm}$ is a static transformation matrix, ϵ_{ijk} is the Levi-Civita tensor, the T superscript in Eq. (4.47) denotes the transpose operation, and $\delta V_B = V_B - \langle V_B \rangle$ is the fluctuation of the interaction with the the bath from its equilibrium value. It is also necessary to evaluate one more static matrix for the GQME evolution in Eq. (4.8),

$$\dot{\mathcal{C}}_{nm}(0) = -2\Big[(\varepsilon + \langle V_B \rangle) \epsilon_{znm} + \Delta \epsilon_{xnm} \Big]. \tag{4.48}$$

The dynamic matrices are

$$\mathcal{C}^{(jk)}_{nm}(t) \equiv (V_{B,j}\sigma_n | V_{B,k}(t)\sigma_m(t)), \tag{4.49}$$

where

$$V_{B,k} = \begin{cases} V_B, & k = 1, \\ 1, & k = 0. \end{cases} \tag{4.50}$$

We further note that $\mathcal{C}^{(00)}_{nm}(t) = \mathcal{C}_{nm}(t)$.

Using these expressions, one can rewrite the auxiliary kernels thus,

$$\mathcal{K}^{(1)}(t) = \mathcal{Y}^T[\mathcal{C}^{(11)}(t) + \langle V_B\rangle^2\mathcal{C}^{(00)}(t) - \langle V_B\rangle(\mathcal{C}^{(01)}(t) + \mathcal{C}^{(10)}(t))]\mathcal{Y},$$

$$\mathcal{K}^{(3b)}(t) = \mathcal{Y}^T[\mathcal{C}^{(10)}(t) - \langle V_B\rangle\mathcal{C}^{(00)}(t)], \tag{4.51}$$

$$\mathcal{K}^{(3f)}(t) = -[\mathcal{C}^{(01)}(t) - \langle V_B\rangle\mathcal{C}^{(00)}(t)]\mathcal{Y}. \tag{4.52}$$

Quasi-classical treatment of $\mathcal{C}^{(jk)}_{nm}(t)$

In analogy to the definition of nonequilibrium averages [139], one may express a correlation function within the Ehrenfest formalism as

$$\begin{aligned} C_{XY}(t) &= \mathrm{Tr}[X_S(0)X_B(0)Y_S(t)Y_B(t)] \\ &\approx [2\pi\hbar]^{-N}\int d\Gamma\ X^W_B(0)Y^W_B(t)\mathrm{Tr}_S[X_S(0)Y_S(t)], \end{aligned} \tag{4.53}$$

where the superscript W indicates the partial Wigner transform of the operator with respect to the bath degrees of freedom, and N is the number of degrees of freedom over which the Wigner transform is being performed. The Wigner transform of an operator is defined as [125],

$$X^W(\mathbf{x},\mathbf{p}) = \int d\mathbf{s}\ e^{-i\mathbf{p}\cdot\mathbf{s}/\hbar}\left\langle \mathbf{x}+\mathbf{s}/2\right| \hat{X} \left|\mathbf{x}-\mathbf{s}/2\right\rangle. \tag{4.54}$$

In the following, we only perform the partial Wigner transform with respect to the bath degrees of freedom, as is required by the Ehrenfest procedure.

For equilibrium correlation functions of the form given by Eq. (4.49), it is necessary to obtain an expression for the partially transformed canonical density operator $\rho = e^{-\beta H}/\mathrm{Tr}[e^{-\beta H}]$. Here we adopt the approach presented in Ref. [162], and express partial Wigner transform of the canonical operator as

$$\rho^W = \sum_a N_a \mathcal{S}_a \otimes \mathcal{B}_a^W(\mathbf{x}, \mathbf{p}), \tag{4.55}$$

where $\mathcal{S}_a$ is a pure system operator, and $\mathcal{B}_a^W$ is corresponds to a normalized bath density operator, i.e., $\int d\Gamma \ \mathcal{B}_a^W(\mathbf{x}, \mathbf{p}) = 1$ (for detailed expressions, see Appendix 4.A). For convenience, we reexpress $\mathcal{S}_a$ in terms of a convenient basis, namely $\mathcal{S}_a = \sum_b r_{ab} S_b$, where $S_b \in \{\mathbf{1}_S, \sigma_x, \sigma_y, \sigma_z\}$. Using the above notation, we rewrite the expressions for the dynamic matrices in Eq. (4.49) as follows,

$$\begin{aligned} \mathcal{C}_{nm}^{(jk)}(t) \approx \frac{1}{2} \sum_p \int d\Gamma \ \Bigg[& i\Big([\mathcal{B}_p, V_{B,j}]\Big)^W V_{B,k}^W(t) \mathrm{Tr}_S[X_{pn}\sigma_m(t)] \\ & + \Big(\{\mathcal{B}_p, V_{B,j}\}\Big)^W V_{B,k}^W(t) \mathrm{Tr}_S[Y_{pn}\sigma_m(t)] \Bigg], \end{aligned} \tag{4.56}$$

where

$$X_{pn} = \sum_{l \in x,y,z} r_{pl} \epsilon_{lns} \sigma_s, \tag{4.57}$$

$$Y_{pn} = r_{pn} \mathbf{1}_S + r_{p1} \sigma_n \tag{4.58}$$

Noting that the Wigner transform of operator products can be obtained via the Moyal expansion [125, 145]

$$(AB)^W = A^W e^{i\Lambda/2\hbar} B^W, \tag{4.59}$$

we can express the commutator and anticommutator of the bath density operator and the bath part of the interaction as,

$$\Big(\mathcal{B}_p V_{B,j}\Big)^W = \mathcal{B}_p^W \Big[V_{B,j}^W - i\zeta_{B,j}^W\Big], \tag{4.60}$$

where

$$\zeta_{B,j}^W = \begin{cases} \zeta_B^W, & j=1, \\ 0, & j=0. \end{cases} \tag{4.61}$$

The expression for ζ_B^W can be found in Eq. (4.45).

Substituting expressions (4.60) into (4.56) yields,

$$\mathcal{C}_{nm}^{(jk)}(t) = \sum_p \int d\Gamma\ \mathcal{B}_p^W V_{B,k}^W(t)\Big[\zeta_{B,j}^W \mathrm{Tr}_S[X_{pn}\sigma_m(t)] + V_{B,j}^W \mathrm{Tr}_S[Y_{pn}\sigma_m(t)]\Big], \tag{4.62}$$

Explicitly evaluating X_{pn} and Y_{pn}, we provide explicit expressions for the $\mathcal{C}_{nm}^{jk}(t)$-functions in terms of functions that are simple to simulate,

$$\mathcal{C}_{xm}^{(ij)} = \sum_k [r_{k1} s_{xm,s}^{(ij,k)}(t) + r_{kx} s_{1m,s}^{(ij,k)}(t) + r_{kz} s_{ym,a}^{(ij,k)}(t) - r_{ky} s_{zm,a}^{(ij,k)}(t)], \tag{4.63}$$

$$\mathcal{C}_{ym}^{(ij)} = \sum_k [r_{k1} s_{ym,s}^{(ij,k)}(t) + r_{ky} s_{1m,s}^{(ij,k)}(t) + r_{kx} s_{zm,a}^{(ij,k)}(t) - r_{kz} s_{xm,a}^{(ij,k)}(t)], \tag{4.64}$$

$$\mathcal{C}_{ym}^{(ij)} = \sum_k [r_{k1} s_{zm,s}^{(ij,k)}(t) + r_{kz} s_{1m,s}^{(ij,k)}(t) + r_{ky} s_{xm,a}^{(ij,k)}(t) - r_{kx} s_{ym,a}^{(ij,k)}(t)], \tag{4.65}$$

where

$$s_{nm,s}^{(ij,k)}(t) = \int d\Gamma\ \mathcal{B}_{B,k}^W V_{B,i}^W(0) V_{B,j}^W(t) \mathrm{Tr}_S[B_n(0)\sigma_m(t)], \tag{4.66}$$

$$s_{nm,a}^{(ij,k)}(t) = \int d\Gamma\ \mathcal{B}_{B,k}^W \xi_{B,i}^W(0) V_{B,j}^W(t) \mathrm{Tr}_S[B_n(0)\sigma_m(t)], \tag{4.67}$$

are real and $B_n \in \{\mathbf{1}_S, \sigma_x, \sigma_y, \sigma_z\}$. Direct evaluation of these functions is straightforward via the Ehrenfest method. We direct the reader to Ref. [104] for instructions on how to properly treat the system initial conditions for these functions.

Chapter 5

Generalized Quantum Master Equations In and Out of Equilibrium: When Can One Win?[1]

5.1 Introduction

Generalized quantum master equations (GQMEs) provide a formal framework to describe the time evolution of observables and correlation functions in complex, many-body, systems based on the projection operator method [127, 128, 142]. The generalized master equation formalism has found extensive use both in allowing efficient and accurate calculations of material properties, including diffusion constants of liquids [164–168], density fluctuations

[1]Based on work published in J. Chem. Phys. **144**, 184105 (2016). Copyright 2016, American Institute of Physics.

in glasses [70–72, 169], and structural relaxation in polymers [170, 171]. In addition, it has also been heavily exploited as an analysis tool to uncover the inherent timescales in complex chemical systems [172], as a dimensionality reduction technique in the development of coarse-grained molecular models [173], and more broadly in areas such as meteorological and financial time-series analysis and optimal prediction methods [174–177]. The central quantity in the GQME formalism is the memory kernel, which encodes the effect of the projected dynamical degrees of freedom on the observable. However, the standard expressions for the memory kernel contain projected dynamical quantities that are impractical to simulate directly. This has led to the development of a number of ways to approximate the memory kernel that allow it to be recast in terms of unprojected dynamical quantities [88, 89], assumed functional forms [90], or a given (perturbative or Markovian) limit [1, 2, 42, 43, 91, 92].

Just over a decade ago, Shi and Geva derived a formally exact representation for the memory kernel of the Nakajima-Zwanzig GQME that requires only projection-free input [93]. This representation opened the door to using either numerically exact or approximate methods to simulate the memory kernel. For exact treatments, whose computational cost increases severely with propagation time, exploiting the rapid decay of the memory kernel has been shown to allow for significant gains in the efficiency of simulating charge and energy transport in the condensed phase [93–100, 138, 144, 178].

When approximate methods, such as those arising from the quantum-classical and semi-classical hierarchies[47, 63, 83, 179, 180], are used to calculate the memory kernel significant improvements in accuracy have been observed when compared to their direct application [100–104, 144]. However, such improvements sensitively depend on how one calculates the

projection-free partial kernels that are used to construct the memory kernel [104]. These observations naturally raise questions as to why this is and when proceeding via the projection operator formalism will be advantageous.

Here we show, for both equilibrium and nonequilibrium systems, the conditions under which proceeding via the GQME formalism yields results that are guaranteed to be identical to the original dynamics used in the projection free input, and suggest how this limitation can be overcome. To achieve this, we show how the memory kernel governing the evolution of equilibrium and nonequilibrium systems can be exactly recast in terms of unprojected correlation functions, which can be straightforwardly simulated using either exact or approximate methods. By analyzing these expressions, we derive the necessary requirements for an approximate dynamics to yield the same results when used directly and as an approximation to the memory kernel in the GQME approach. These results thus provide insights into when GQME methods might allow for improvement in accuracy or efficiency in equilibrium and nonequilibrium situations in a diverse set of systems.

5.2 GQMEs In and Out of Equilibrium

To begin we consider the Nakajima-Zwanzig GQME [127, 128], which provides a particularly straightforward route for describing the reduced dynamics of systems out of equilibrium. In this scheme the total system is decomposed into two parts: the system, which consists of all the degrees of freedom of interest in the problem, and the bath, which comprises the remaining degrees of freedom. For equilibrium systems the Mori approach is typically the preferred formulation [142]. However, the Mori formalism, which renders renders distinction

between system and bath unnecessary, is general and can be used for both equilibrium and nonequilibrium problems. Indeed, as observed in Ref. [104], both the Mori and Nakajima-Zwanzig approaches can be written in a unified formalism stemming from the projected equation of motion for the propagator,

$$\frac{d}{dt}e^{i\mathcal{L}t} = e^{i\mathcal{L}t}i\mathcal{L} = e^{i\mathcal{L}t}(\mathcal{P}+\mathcal{Q})i\mathcal{L} \tag{5.1}$$

where the Liouville operator is $\mathcal{L} = \frac{1}{\hbar}[\hat{H}, \cdot]$, $\hat{H}$ is the Hamiltonian operator, $\mathcal{P}$ is a projection operator and $\mathcal{Q} = \mathbf{1} - \mathcal{P}$ is the complementary projection operator.

Central to the Mori approach is the appropriate choice of projection operator, $\mathcal{P}$. In the following, we assume that it takes the form,

$$\mathcal{P} = |\mathbf{A})(\mathbf{A}|, \tag{5.2}$$

where $\mathbf{A}$ contains a subset of observables which are of particular interest. The definition of the inner product is chosen such that $(\mathbf{A}|\mathbf{A}) = \mathbf{1}$, thus satisfying the idempotency condition, $\mathcal{P}^2 = \mathcal{P}$. Consequently, the complementary projector, $\mathcal{Q}$, is by construction orthogonal to the subspace defined by $\mathcal{P}$.

Using the Dyson operator identity

$$e^{i\mathcal{L}t} = e^{i\mathcal{Q}\mathcal{L}t} + \int_0^t d\tau\ e^{i\mathcal{L}(t-\tau)}(\mathcal{P}i\mathcal{L})e^{i\mathcal{Q}\mathcal{L}\tau}, \tag{5.3}$$

to expand the second term in the second equality of Eq. (5.1) yields

$$\frac{d}{dt}e^{i\mathcal{L}t} = ie^{i\mathcal{L}t}\mathcal{P}\mathcal{L} + i\mathcal{Q}e^{i\mathcal{L}\mathcal{Q}t}\mathcal{L} - \int_0^t d\tau\ e^{i\mathcal{L}(t-\tau)}\mathcal{P}\mathcal{L}\mathcal{Q}e^{i\mathcal{L}\mathcal{Q}\tau}\mathcal{L}. \tag{5.4}$$

Restricting our attention to correlation functions defined by the inner product of the elements constituting $\mathcal{P}$, the equation of motion for the propagator in Eq. (5.4) yields the

following Mori-type GQME for the correlation function $\mathcal{C}(t) = (\mathbf{A}|\mathbf{A}(t))$,

$$\dot{\mathcal{C}}(t) = \mathcal{C}(t)\dot{\mathcal{C}}(0) - \int_0^t d\tau\ \mathcal{C}(t-\tau)\mathcal{K}(\tau), \tag{5.5}$$

and the memory kernel, $\mathcal{K}(t)$, takes the form,

$$\mathcal{K}(t) = (\mathbf{A}|\mathcal{L}\mathcal{Q}e^{i\mathcal{Q}\mathcal{L}t}\mathcal{Q}\mathcal{L}|\mathbf{A}). \tag{5.6}$$

Direct evaluation of the memory kernel in Eq. (5.6) is problematic, as it requires the action of the projected propagator, $e^{i\mathcal{Q}\mathcal{L}t}$.

To circumvent the difficulty of the projected propagator, the Dyson identity, Eq. (5.3), can be used to obtain a self-consistent expansion of the memory kernel,

$$\mathcal{K}(t) = \mathcal{K}_1(t) + \int_0^t d\tau\ \mathcal{K}_3(t-\tau)\mathcal{K}(\tau), \tag{5.7}$$

where the partial (auxiliary) kernels,

$$\mathcal{K}_1(t) = (\mathbf{A}|\mathcal{L}\mathcal{Q}e^{i\mathcal{L}t}\mathcal{Q}\mathcal{L}|\mathbf{A}), \tag{5.8}$$

$$\mathcal{K}_3(t) = -i(\mathbf{A}|\mathcal{L}\mathcal{Q}e^{i\mathcal{L}t}|\mathbf{A}), \tag{5.9}$$

no longer require the use of projected dynamics. The labels for the partial kernels of 1 and 3 are chosen so as to be consistent with earlier work [93, 100–104]. In principle, the memory kernel $\mathcal{K}(t)$ can be obtained by generating $\mathcal{K}_1(t)$ and $\mathcal{K}_3(t)$ from simulation and solving Eq. (5.7) numerically. Depending on the choice of projection operator and definition of the inner product, one can specialize this result to equilibrium correlation functions or equilibrium population dynamics.

In the equilibrium case, the Kubo-transformed correlation function is obtained by defining the inner product as

$$(\mathbf{A}|\mathcal{O}|\mathbf{A}) \equiv \int_0^\beta d\lambda\ \mathrm{Tr}[\rho_{eq}\mathbf{A}^\dagger(0)\mathcal{O}\mathbf{A}(i\lambda)] \cdot \chi_{AA}^{-1}, \tag{5.10}$$

where $\mathcal{O}$ is a general superoperator in Liouville space (e.g. $e^{i\mathcal{L}t}$), $\rho_{eq} = Z^{-1}e^{-\beta\hat{H}}$ is the canonical density operator, $Z = \mathrm{Tr}[e^{-\beta\hat{H}}]$ is the partition function, $\beta = 1/k_BT$ is the inverse of the thermal energy, and $\chi_{AA} = \mathrm{Tr}[\rho\mathbf{A}^\dagger(0)\mathbf{A}(0)]$. Commonly, the elements of the vector $\mathbf{A}$ are chosen to consist of a dynamical variable, $\mathbf{a}$, which is a function of the coordinates and momenta of the system, and its time derivative, $\dot{\mathbf{a}} = i\mathcal{L}\mathbf{a}$. For example, in the case of diffusion $\mathbf{a}$ could be chosen to be the position or velocity of some or all of the particles, and for infrared spectroscopy as the system dipole moment.

In nonequilibrium cases the inner product may be defined as [104]

$$(\mathbf{A}|\mathcal{O}|\mathbf{A})_{nm} \equiv \mathrm{Tr}[\mathcal{R}_B A_n^\dagger \mathcal{O} A_m], \tag{5.11}$$

where the set $\{A_n\}$ spans a limited subspace of the total Hilbert space of the system, and $\mathcal{R}_B$ is an operator that belongs to the complementary space, which is conventionally denoted as the bath. The normalization condition on $\mathcal{R}_B$ requires that the trace over the bath degrees of freedom yield unity, $\mathrm{Tr}_B[\mathcal{R}_B] = 1$. The elements of $\mathbf{A}$ can, for example, be chosen such that $\{A_n\}$ spans all outer products of the system states and $\mathcal{R}_B = e^{\beta H_B}/\mathrm{Tr}_B[e^{\beta H_B}]$ corresponds to the canonical distribution for the bath degrees of freedom. Such a choice for the projector provides access to nonequilibrium population and coherence dynamics of the system, and has been used in the context of the spin-boson model [93, 100–102, 104, 178], and in a wide class of quantum impurity models to access site occupation dynamics in the presence of one or more noninteracting fermionic or bosonic baths [95–99, 138].

5.3 When can one win?

The expressions in Eqs. (5.7), (5.8), and (5.9) have been shown to improve the accuracy of the dynamics produced by a number of approximate methods [100–104] when used in the GQME formalism. This is shown in Fig. 5.1 for the spin boson problem, where the three different approximate semiclassical methods yield almost quantitatively exact results when used as an approximation to the memory kernel (solid lines) but fail markedly when used directly (dashed lines).

Using manipulations that are exactly satisfied in quantum mechanics, but not necessarily by approximate methods, here we show how the memory kernel can be written in a form that returns a result that is identical to that obtained using the approximate method directly (irrespective of the approximate method employed). By analyzing the steps that are necessary to derive this expression, we are thus able to show the classes of approximate dynamics methods that will be guaranteed to always yield the same result when used directly or via the memory kernel formalism, no matter which expression for the memory kernel is used.

One begins by expanding the complementary projection operator $\mathcal{Q}$ and applying the Liouville operators [104]. Carrying out the former operation for $\mathcal{K}_3$ (Eq. (5.9)) yields,

$$\mathcal{K}_3(t) = -i(\mathbf{A}|\mathcal{L}e^{i\mathcal{L}t}|\mathbf{A}) + i(\mathbf{A}|\mathcal{L}|\mathbf{A})(\mathbf{A}|e^{i\mathcal{L}t}|\mathbf{A}). \tag{5.12}$$

The Liouville operator, $\mathcal{L}$, can then be applied backwards on the static part or forwards to generate the time derivative. Doing the latter allows the partial kernel to be written purely as a function of $\mathcal{C}(t)$ and its time derivatives,

$$\mathcal{K}_3(t) = -\dot{\mathcal{C}}(t) + \dot{\mathcal{C}}(0)\mathcal{C}(t). \tag{5.13}$$

Proceeding similarly for $\mathcal{K}_1$ gives,

$$\begin{aligned}\mathcal{K}_1(t) &= (\mathbf{A}|\mathcal{L}e^{i\mathcal{L}t}\mathcal{L}|\mathbf{A}) - \dot{\mathcal{C}}(0)\mathcal{C}(t)\dot{\mathcal{C}}(0) + i\dot{\mathcal{C}}(0)(\mathbf{A}|e^{i\mathcal{L}t}\mathcal{L}|\mathbf{A}) + i(\mathbf{A}|\mathcal{L}e^{i\mathcal{L}t}|\mathbf{A})\dot{\mathcal{C}}(0) \\ &= (\mathbf{A}|e^{i\mathcal{L}t}\mathcal{L}^2|\mathbf{A}) - \dot{\mathcal{C}}(0)\mathcal{C}(t)\dot{\mathcal{C}}(0) + i\{\dot{\mathcal{C}}(0), (\mathbf{A}|e^{i\mathcal{L}t}\mathcal{L}|\mathbf{A})\} \\ &= -\ddot{\mathcal{C}}(t) + \{\dot{\mathcal{C}}(0), \dot{\mathcal{C}}(t)\} - \dot{\mathcal{C}}(0)\mathcal{C}(t)\dot{\mathcal{C}}(0),\end{aligned} \tag{5.14}$$

where in the second and last equalities the braces denote the anticommutator.

Due to the convolution-based structure of the equations relating the full memory kernel to the partial kernels, it is particularly convenient to consider its Fourier-Laplace representation. The Fourier-Laplace transform of $\mathcal{C}(t)$ is defined as,

$$\mathcal{C}(\omega) = \int_0^\infty dt\ e^{i\omega t}\mathcal{C}(t), \tag{5.15}$$

and its nth time-derivative, $\mathcal{C}^{(n)}(t) \equiv \frac{d^n}{dt^n}\mathcal{C}(t)$, is

$$\mathcal{C}^{(n)}(\omega) = (-i\omega)^n\mathcal{C}(\omega) - \sum_{k=1}^{n}(-i\omega)^{n-k}\mathcal{C}^{(k-1)}(t=0). \tag{5.16}$$

Application of the Fourier-Laplace transform to Eq. (5.7) gives,

$$\mathcal{K}(\omega) = [\mathbf{1} - \mathcal{K}_3(\omega)]^{-1}\mathcal{K}_1(\omega), \tag{5.17}$$

and to Eqs. (5.14) and (5.13) yields,

$$\mathcal{K}_1(\omega) = -\Omega(\omega)[\mathbf{1} + \mathcal{C}(\omega)\Omega(\omega)], \tag{5.18}$$

$$\mathcal{K}_3(\omega) = \mathbf{1} + \Omega(\omega)\mathcal{C}(\omega), \tag{5.19}$$

where $\Omega(\omega) = i\omega + \dot{\mathcal{C}}(t=0)$. Using the Fourier-Laplace transforms of the memory kernels in Eqs. (5.18) and (5.19) in Eq. (5.17) gives,

$$\mathcal{K}(\omega) = \mathcal{C}^{direct}(\omega)^{-1}[\mathbf{1} + \mathcal{C}^{direct}(\omega)\Omega(\omega)], \tag{5.20}$$

where we have introduced the superscript *direct* to highlight that $\mathcal{C}^{direct}(\omega)$ is the Fourier-Laplace transformed correlation function obtained from the direct dynamics. The corresponding GQME expression for the correlation function, $\mathcal{C}^{GQME}(\omega)$, can be obtained by Fourier-Laplace transforming and rearranging the equation of motion for the correlation function in Eq. (5.5),

$$\mathcal{C}^{GQME}(\omega) = [\mathcal{K}(\omega) - \Omega(\omega)]^{-1} \tag{5.21}$$

where we have used $\mathcal{C}(t = 0) = \mathbf{1}$, which follows from the idempotency property of the projector. Inserting the expression for the memory kernel in terms of the direct correlation function from Eq. (5.20) in this expression and rearranging gives $\mathcal{C}^{GQME}(\omega) = \mathcal{C}^{direct}(\omega)$. Hence, *when one uses expressions for the partial kernels that depend only on the original correlation function, $\mathcal{C}(t)$, and its time-derivatives, one is certain to recover exactly the same result as would be obtained from a direct application of the dynamics used to calculate the partial kernels.*

This result therefore proves that no accuracy benefit can be obtained through the GQME for any approximate method using Eqs. (5.13) and (5.14).[2] More explicitly, using manipulations that are exactly satisfied by quantum mechanics to recast the partial kernels in terms of the original correlation function and its time derivatives removes any potential benefit for gains in accuracy by proceeding via the GQME formalism. This is shown in Fig. 5.1 where, when Eqs. (5.13) and (5.14) are simulated using Ehrenfest mean field theory (blue dotted line), the same result is obtained as a direct application of mean field theory (blue dashed line).

[2]We note that a second decomposition of the memory kernel can be obtained from Eq. (5.6) through the use of the identity $e^{i\mathcal{Q}\mathcal{L}t}\mathcal{Q} = \mathcal{Q}e^{i\mathcal{L}\mathcal{Q}t}$.[104] A similar proof for this type of closure is straightforward and follows the same steps outlined above

It should be noted that all the expressions given for the partial kernels in the preceding equations (i.e., Eqs. (5.8) and (5.9) as well as Eqs. (5.14) and (5.13)) are guaranteed to give the same result as a direct application when exact quantum dynamics is used to generate them. However, if the partial kernels are shorter-lived than the correlation function, one can still obtain significant efficiency gains when using numerically exact methods, which scale poorly with simulation time.

The fact that Eqs. (5.13) and (5.14) cannot be used to obtain an increase in accuracy for any approximate method begs the question: What are the conditions that an approximate method must satisfy to guarantee that the same result will be obtained by using Eqs. (5.8) and (5.9) as Eqs. (5.14) and (5.13)? Identifying such conditions allows the identification of the classes of approximate methods which *cannot* gain accuracy benefits by combination with the GQME formalism. Indeed, we can immediately see that approximate methods only need to satisfy two such conditions. The first is that

$$\frac{d}{dt}\mathcal{C}(t) = (\mathbf{A}|e^{i\mathcal{L}'t}[i\mathcal{L}'\mathbf{A}]), \tag{5.22}$$

where $\mathcal{L}'$ indicates a Liouville operator corresponding to an approximate dynamics. Explicitly, this condition requires that the correlation function of $\mathbf{A}$ and the operator resulting from the action of the Liouvillian acting on $\mathbf{A}$ is equivalent to the time-derivative of the original correlation function. While the equality in Eq. (5.22) is trivially maintained for numerically exact methods, the same is not necessarily true for approximate methods. The second condition requires that the approximate Liouville operator commutes with the propagator,

$$[\mathcal{L}', e^{i\mathcal{L}'t}] = 0. \tag{5.23}$$

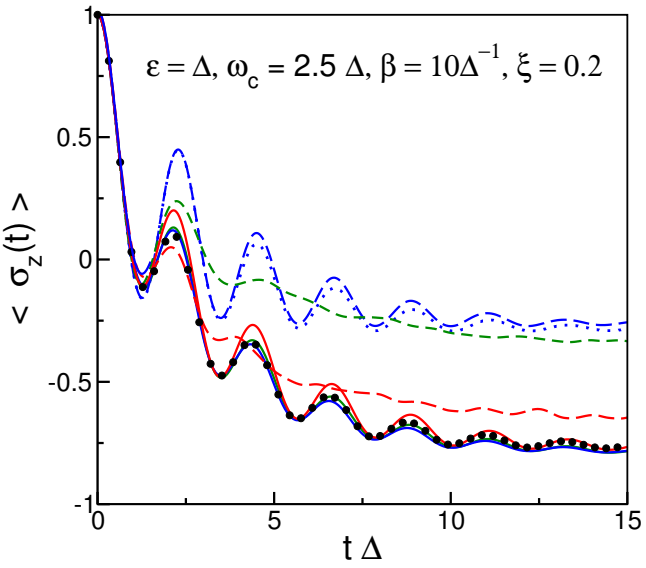

Figure 5.1: Evolution of the subsystem population difference versus time for the nonequilibrium relaxation of a spin-boson system initially prepared in the excited state. Numerically exact QUAPI [19] (black dots), Ehrenfest mean field (blue), PBME [181] (green), FBTS [182] (red). Solid lines represent results using the GQME kernels in Eqs. (5.8) and (5.9), and dotted lines use those given in Eqs. (5.14) and (5.13). The dashed lines are direct dynamics. The simulation procedures and definition of the parameters are as used in Refs. [102] and [104].

These conditions are all that are required of an approximate method to perform the manipulations in Eq. (5.14) and likewise to obtain Eq. (5.13) from Eq. (5.9). Consequently, *the GQME approach cannot yield improvements in accuracy when the approximate method used to calculate the partial kernels satisfies the conditions given by Eqs. (5.22) and (5.23).*

In the case of equilibrium correlation functions, where the Liouville operator commutes with the canonical density matrix, Eq. (5.23) is equivalent to time-translational invariance.

For example, dynamics methods such as CMD [53], RPMD [54, 57], and purely classical mechanics satisfy these properties and thus are guaranteed not to obtain increased accuracy when used to approximate equilibrium correlation functions via the GQME approach. However, for nonequilibrium correlation functions, and for methods that do not satisfy these conditions, one can expect the dynamics resulting from the GQME to differ from the direct application of the approximate method, as has been shown in previous work where significant gains in both efficiency and accuracy have been achieved [100–104, 144].

5.4 Conclusions

In this paper, we have shown that when the memory kernel is formally cast in terms of the original correlation function and its time derivatives, the GQME is guaranteed to return the same result as that obtained from a direct simulation, regardless of the method used to construct the kernel. Further, we have used this to define the criteria that, if satisfied by an approximate dynamics method, guarantees that that the method will produce GQME dynamics that are identical to that given by its direct dynamics, independent of the way the partial kernels are expressed. In these cases, where no such benefit in accuracy can be obtained, one may still expect the GQME scheme to yield improved efficiency if the memory kernels are short-lived. Conversely, violation of the criteria in Eqs. (5.22) and (5.23) imply that the resulting GQME dynamics will in general be different from direct simulation of the correlation functions. Previous studies [100–104] and Fig. 5.1 have indeed confirmed that the GQME approach is capable of yielding significant gains both in efficiency and accuracy, when one does not invoke the formal recasting of the partial kernels in Eqs. (5.13) and

(5.14), using a wide range of approximate theories. These insights thus outline a path for future applications of the GQME formalism by allowing one to assess the benefits that it may afford.

Chapter 6

Path integral approach to the Wigner representation of canonical density operators for discrete systems coupled to harmonic baths

6.1 Introduction

Practical and accurate representations of fully correlated canonical density operators are essential for the determination of both thermodynamic and dynamic properties of many-body systems. The description of the thermodynamics of a system provides access to quantities like entropy, heat capacity, and various susceptibilities, which provide insight into, for example, the nature of equilibrium phase transitions. On the dynamical side, equilibrium time

correlation functions, which require sampling from the full equilibrium Boltzmann operator, lie at the heart of the description of linear and nonlinear spectroscopy [15], the determination of transport coefficients in condensed phase systems [146, 183], and the calculation of chemical rate constants [134, 149, 172, 184]. The development of schemes that accurately represent the canonical density operator has been the objective of a large number of theoretical efforts that have, in turn, produced an impressive spectrum of numerically exact [38, 132, 156, 185–191] and approximate methods [47, 48, 50, 51, 53, 54, 56]. However, despite significant progress, the calculation of static and dynamical properties of many-body quantum systems remains a challenging task.

For many complex systems, the phase space formulation of quantum mechanics, as encoded by the Wigner distribution, has provided a particularly convenient platform for the investigation of both dynamics and thermodynamics [125, 145, 192–194]. While the phase space formulation provides a rigorous, if generally impractical, protocol for the evolution of operators via the Moyal bracket [125, 145], its utility lies in its compatibility with the semi-classical hierarchy of techniques. The incorporation of the Wigner approach into these approximate methods not only sidesteps the complications associated with the Moyal bracket expansion, but also allow for the choice of the level of sophistication and accuracy necessary for dynamical calculations. Indeed, this is an essential factor as the simple Ehrenfest [61, 62], surface hopping [63, 64], and linearized semiclassical initial value representation [65–67] (LSC-IVR) schemes become the only practical approaches for many complex systems. In addition, the phase space framework has also been an integral component in the development of successful hybrid schemes that combine numerically exact quantum approaches or traditional perturbation theories with classical time evolution [27, 28, 81, 109, 113].

Unfortunately, the Wigner transformation of the canonical density for complex systems can rarely be obtained analytically, and its numerical determination contends with the challenge of the highly oscillatory phase associated with the Fourier transform [65]. Nevertheless, a variety of approximations have been developed. These range from the simple replacement of the quantum Boltzmann operator with its classical counterpart, an approximation that is only appropriate at sufficiently high temperatures where the zero-point energy is negligible, to sophisticated path integral-based techniques [49, 58, 60, 159, 161, 195–205]. These approaches have proven useful in the investigation of, for instance, vibrational spectra and relaxation rates [135, 195, 206, 207], proton transfer problems [204], and quantum diffusion in para-hydrogen [208] and liquid neon [199]. The benefits of these approximations notwithstanding, the general accuracy of approximate Wigner transformed density operators in complex systems has been difficult to assess, especially when used in conjunction with dynamical calculations.

Here we show that for impurity-type problems where the system-bath coupling is linear in the bath coordinates and the bath can be approximated as harmonic, the Wigner transform of the canonical density operator can be obtained analytically. For this reason, we focus on the simplest nontrivial model that captures the relaxation and dephasing of generic quantum systems coupled to a quantum bath with arbitrary coupling strength: the spin-boson (SB) model. Of course, even for the SB model the integration of the bath degrees of freedom required by the Wigner transformation cannot be achieved without a Hamiltonian splitting procedure, achieved in the path integral framework by means of the Trotter approximation. Naturally, the formalism provided here is not restricted to SB model, but is also applicable to any generalization where the bath remains harmonic and the coupling linear in the bath

coordinate. To ensure that the resulting density operator can be used in conjunction with quasi-classical methods such as the Ehrenfest and surface hopping schemes as well as with conventional semi-classical methods, we implement only the partial Wigner transform with respect to the bath degrees of freedom. Extension to the full Wigner transformation can be achieved simply through the use of the mapping variable formalism [44, 45, 209, 210].

Importantly, the present scheme provides a computationally simple approach to the calculation of thermodynamic data for SB-type systems. By providing a numerically exact representation for initial conditions to be used in dynamical simulations, this method also represents a important benchmark for the use of approximate Wigner transformed canonical densities both in the static and dynamic contexts. This property allows us to demonstrate that the current method converges rapidly with respect to the number of path integral slices for a large region of parameter space, and that proper rendering of the canonical density can dramatically influence the the accuracy of both thermodynamic and dynamic quantities. Interestingly, the analytical expression derived here reveals the canonical density as a linear superposition of bath distributions with weights determined by the paths allowed in configuration space.

It bears remarking that Moix, Zhao, and Cao have previously developed a related and highly efficient approach based on the influence functional formalism for the calculation of the reduced density matrix of a system coupled linearly to a harmonic bath [211]. The reduced density matrix, which corresponds to the partial trace over the bath degrees of freedom of the full canonical density operator, permits the calculation of thermodynamic averages of any *system* operator, but precludes calculation of any non-system property. In contrast, by providing an analytical form for the *full* canonical density operator, our approach permits the

calculation of *any* thermodynamic average, albeit at a higher computational cost. Another advantage of the present work is that, as stated above, it can be used to efficiently and exactly sample the initial conditions required for the quasi- or semi-classical calculation of equilibrium time correlation functions. Similar to the work of Moix *et al.*, our work can be easily generalized to N-level systems coupled to harmonic baths and is not limited to any specific form of the spectral density, $J(\omega)$.

The paper is organized as follows. In Sec. 6.2, we introduce the formalism used in the paper. Specifically, in Sec. 6.2, we present a brief review of the phase space formulation of quantum mechanics. Sec. 6.2 introduces the SB Hamiltonian. In Sec. 6.2 we introduce an outline of the derivation of the Wigner-transformed canonical density for the SB model (the extended derivation can be found in Appendix 6.A). Sec. 6.3 contains the results and in Sec. 6.4 we conclude.

6.2 Theory

Phase Space Formulation

As stated in the Introduction, the phase space formulation of quantum mechanics provides a framework that integrates the use of Monte Carlo sampling of initial conditions coupled with trajectory-based methods associated with quasi- and semi-classical methods. Within this framework, the trace over two operators can be expressed in phase space as

$$\mathrm{Tr}[\hat{A}\hat{B}] = [2\pi]^{-f} \int d\mathbf{x}d\mathbf{y}\ A^W(\mathbf{x},\mathbf{y})B^W(\mathbf{x},\mathbf{y}), \tag{6.1}$$

where $A^W(\mathbf{x},\mathbf{p})$ and $B^W(\mathbf{x},\mathbf{p})$ are Wigner transformed versions of operators $\hat{A}$ and $\hat{B}$, which become functions of the classical coordinate and conjugate momentum variables $\mathbf{x}$ and $\mathbf{p}$, respectively, and f is the number of degrees of freedom with respect to which the Wigner transform is performed. The Wigner transform of an operator, $\hat{O}$, is defined as,

$$O^W(\mathbf{x},\mathbf{p}) = \int d\mathbf{s}\; e^{-i\mathbf{p}\cdot\mathbf{s}} \left\langle \mathbf{x}+\mathbf{s}/2\right| \hat{O} \left|\mathbf{x}-\mathbf{s}/2\right\rangle . \tag{6.2}$$

As Eqs. (6.1) and (6.2) suggest, the phase space formulation can be used to obtain static averages when both A and B in Eq. (6.1) are independent of time, or correlation funtions when at least one of the operators is time evolved. In the following, we will be particularly interested in equilibrium time correlation functions of the form,

$$\begin{aligned} \mathcal{C}_{AB}(t) &= \mathrm{Tr}[\rho A(0)B(t)] \\ &= [2\pi\hbar]^{-f} \int d\mathbf{x}d\mathbf{p}\; [\rho A(0)]^W(\mathbf{x},\mathbf{p})[B(t)]^W(\mathbf{x},\mathbf{p}), \end{aligned} \tag{6.3}$$

where $\rho = e^{-\beta H}/\mathrm{Tr}[e^{-\beta}H]$ is the canonical density operator, $\beta = [k_B T]^{-1}$ is the inverse of the thermal energy, and $B(t) = e^{iHt/\hbar}Be^{-iHt/\hbar}$.

The Wigner transform for products of operators (e.g., $[\rho A(0)]^W$ in Eq. (6.3)) may be expressed as,

$$[\hat{O}\hat{P}]^W(\mathbf{x},\mathbf{p}) = O^W(\mathbf{x},\mathbf{p}) e^{i\overleftrightarrow{\Lambda}/2\hbar} P^W(\mathbf{x},\mathbf{p}), \tag{6.4}$$

where $\overleftrightarrow{\Lambda}$ is the Poisson bracket operator

$$\overleftrightarrow{\Lambda} = \overleftarrow{\nabla}_{\mathbf{p}} \cdot \overrightarrow{\nabla}_{\mathbf{x}} - \overleftarrow{\nabla}_{\mathbf{x}} \cdot \overrightarrow{\nabla}_{\mathbf{p}} \tag{6.5}$$

and the arrows above the gradient operators indicate the direction in which they act. For notational simplicity, we henceforth set $\hbar = 1$. As a final note, we remark on the fact that

it is well-known that the Wigner transform of the density operator need not be positive definite [125, 194]. This potential complication presents no difficulties in the calculations that follow.

Hamiltonian

The formalism we develop here is applicable to Hamiltonians consisting of a finite number of discrete states coupled to a noninteracting harmonic bath, with the coupling assumed to be linear in the bath coordinate. The reason for these restrictions is that the current treatment relies on the influence functional approach, which formally eliminates the bath degrees of freedom in from the path integral framework [212, 213].

While this restriction may seem severe, it is noteworthy that a wide spectrum of problems in the condensed phase may be mapped to such a Hamiltonian. For instance, the discrete degrees of freedom often correspond to a limited subset of the electronic or excitonic manifold coupled to an environment, often idealized as an infinite set of harmonic oscillators. Such Hamiltonians can be written as a sum of system, bath, and coupling contributions, $H = H_S + H_B + H_{SB}$. Perhaps the simplest in this class of models is the spin-boson (SB) Hamiltonian [1, 2]. In the SB model, the system part consists of two discrete states,

$$H_S = \varepsilon\sigma_z + \Delta\sigma_x, \tag{6.6}$$

where σ_i corresponds to the i^{th} Pauli matrix, 2ε is the bias energy difference between the two states, and Δ represents the off-diagonal coupling between the two sites and is assumed to be static.

The bath consists of independent harmonic oscillators,

$$H_B = \frac{1}{2}\sum_k \left[\hat{P}_k^2 + \omega_k^2 \hat{Q}_k^2 + \frac{c_k^2}{\omega_k^2}\right], \tag{6.7}$$

where P_k, Q_k and ω_k are the mass-weighted momenta, coordinates, and frequency for the k^{th} harmonic oscillator, respectively. The last term on the right hand side of Eq. (6.7) is a constant term added for later convenience. As mentioned above, the system-bath coupling term is assumed to be linear in the bath coordinates and antisymmetric with respect to the system,

$$H_{SB} = \alpha\sigma_z \sum_k c_k \hat{Q}_k, \tag{6.8}$$

where c_k is the coupling constant describing the strength of the interaction between the system and the k^{th} oscillator. The spectral density, $J(\omega)$, fully determines the coupling between the system and the bath and is assumed to take the functional form,

$$\begin{aligned} J(\omega) &= \frac{2}{\pi}\sum_k \frac{c_k^2}{\omega_k}\delta(\omega - \omega_k), \\ &= \frac{\pi}{2}\xi\omega e^{-\omega/\omega_c}, \end{aligned} \tag{6.9}$$

where the cutoff frequency ω_c determines the correlation time for the bath at finite temperatures, and the Kondo parameter, ξ, is a dimensionless measure of the coupling between the system and bath. The Kondo parameter is also proportional to the reorganization energy of electron transfer theory, $\lambda = \xi\omega_c/\pi = \pi^{-1}\int_0^\infty d\omega\ J(\omega)/\omega$, which represents the energy dissipated after the system undergoes a Frank-Condon transition. The functional form for the spectral density in the second line of Eq. (6.9) corresponds to the often used Ohmic spectral density [1] with an exponential cutoff.

Canonical density: A path integral treatment

Refering back to Eq. (6.3), it is clear that an expression for ρ^W is necessary. Because the system part of the Hamiltonian consists of discrete states, $\{|0\rangle, |1\rangle\}$, we focus on deriving an expression for an arbitrary matrix element of the canonical density after a partial Wigner transform with respect to the bath degrees of freedom,

$$\begin{aligned} \rho^W_{a,b} &= [2\pi]^{-f} \int d\mathbf{s}\ e^{-i\mathbf{p}\cdot\mathbf{s}/\hbar} \rho_{a,b}(\mathbf{x}+\mathbf{s}/2, x-\mathbf{x}/2) \\ &\equiv N_{ab} \cdot \mathcal{R}^W_{a,b}(\mathbf{x},\mathbf{p}), \end{aligned} \tag{6.10}$$

where $\rho_{a,b}(\mathbf{x}+\mathbf{s}/2, x-\mathbf{x}/2) = \langle \mathbf{x}+\mathbf{s}/2| \langle a| \rho |b\rangle |\mathbf{x}-\mathbf{s}/2\rangle$, $a, b \in \{0,1\}$, N_{ab} is temperature dependent normalization constant, and $\mathcal{R}^W_{a,b}(\mathbf{x},\mathbf{p})$ is a bath operator of unit trace, i.e., $\int d\mathbf{x}d\mathbf{p}\ \mathcal{R}^W_{a,b}(\mathbf{x},\mathbf{p}) = 1$, which can be interpreted as the bath distribution function. We henceforth drop the dependence of the bath distribution function on the bath coordinates and momenta, $(\mathbf{x},\mathbf{p})$, for notational clarity. We also note that we have included the prefactor $[2\pi]^{-f}$ in the definition of the Wigner transform of the canonical density so that it obeys the normalization condition $\sum_a \int d\mathbf{x}d\mathbf{p}\ \rho^W_{a,a}(\mathbf{x},\mathbf{p}) = 1$.

For systems where the total Hamiltonian can be partitioned into two components that are simple to diagonalize, the path integral framework can provide a practical route to obtaining the exponentiated form for the Hamiltonian necessary for the calculation of propagators and the Boltzmann factor. In this case, we employ the separation adopted previously by Makri and coworkers in the development of the quasi-adiabatic path integral scheme [18–21], $H = H_{ad} + H_{na}$, where $H_{ad} = H_S$ and $H_{na} = H_B + H_{SB}$, which refer to the adiabatic and nonadiabatic components of the Hamiltonian. With this partitioning, we rewrite the Boltzmann factor using the Trotter factorization as an N-membered product of basic path

integral units

$$e^{-\beta H} = \lim_{N\to\infty}[e^{-\beta H_{na}/2N}e^{-\beta H_{ad}/N}e^{-\beta H_{na}/2N}]^N. \tag{6.11}$$

When N is finite, the above equality ceases to be exact and the error it incurs is of the order $\mathcal{O}(N\cdot\exp\{-\beta[H_{ad},H_{na}]/2N\})$. Also note that the Hermiticity of the Boltzmann factor is maintained by the symmetrical splitting in Eq. (6.11). Using the Trotter decomposition in Eq. (6.11), introducing resolutions of the identity in the system and bath subspaces, $\mathbf{1}_S=\sum_a|a\rangle\langle a|$ and $\mathbf{1}_B=\int d\mathbf{q}\,|\mathbf{q}\rangle\langle\mathbf{q}|$, and performing the integrations over the bath coordinates analytically, it is possible to obtain expressions for temperature-dependent (global) normalization factor and bath distribution in Eq. (6.10). It bears remarking that after integration over the bath degrees of freedom, the sequence of spin-variables that characterize the path integral trajectory in configuration space remain, i.e., the sets $\{k_0,k_1,...,k_N\}$ where $k_j\in\{0,1\}$. To illustrate this, consider the simpler case of treating the isolated subsystem Boltzmann factor via the path integral procedure (with $N=3$) such that

$$\langle k_3|\,e^{-\beta H_S}\,|k_0\rangle \approx \sum_{k_1,k_2}\langle k_3|\,e^{-\beta H_S/3}\,|k_2\rangle\langle k_2|\,e^{-\beta H_S/3}\,|k_1\rangle\langle k_1|\,e^{-\beta H_S/3}\,|k_0\rangle\,, \tag{6.12}$$

where $|k_j\rangle\in\{|0\rangle\,,|1\rangle\}$. In the following, we refer to individual realizations of the sequence $\{k_0,k_1,k_2,k_3\}$ as "paths". Using this notation,

$$\mathcal{R}^W_{a,b}(\mathbf{x},\mathbf{p}) = \mathcal{N}\sum_{\{k_1,\ldots,k_{N-1}\}}\frac{\tilde{W}_{a,b}}{\mathcal{W}_{a,b}}\prod_{l=1}^{F}\exp\Big[-\gamma_p^{(l)}(p_l+i\tilde{\kappa}_p^{(l)})^2-\gamma_x^{(l)}(x_l+\tilde{\kappa}_x^{(l)})^2\Big], \tag{6.13}$$

$$N_{ab} = \frac{\mathcal{W}_{a,b}}{\sum_a\mathcal{W}_{a,a}}, \tag{6.14}$$

where $\mathcal{N}$ is a normalization factor, the ratio $\tilde{W}_{a,b}/\mathcal{W}_{a,b}$ corresponds to the weighting factors associated with individual paths, $\tilde{\gamma}_p$ and $\tilde{\gamma}_p$ ($i\tilde{\kappa}_p^{(l)}$ and $\tilde{\kappa}_x^{(l)}$) are the variances (means) for

the Gaussian distributions of coordinate and momentum of the l^th oscillator, p_l and x_l, respectively, for individual paths. In this notation, the tilde denotes that a quantity is path-dependent. Detailed expressions for these quantities and their derivation can be found in Appendix 6.A.

The interpretation of Eq. (6.13) is straightforward. The bath distribution function for the SB- and other impurity-type models where the bath is harmonic and the system-bath coupling linear in the bath coordinate can be expressed as a linear combination of Gaussian distributions in the bath coordinates where each contribution is weighted by a temperature- and path-dependent quantity $\tilde{W}_{a,b}/\mathcal{W}_{a,b}$ and for which the average displacements of the bath coordinate and momentum are path-dependent quantities. Importantly, Eqs. (6.13) and (6.14) constitute the main result of the analytical manipulations presented in this work. We emphasize as well that the expressions for the canonical density of the SB model derived here may be used to calculate thermodynamic properties and averages and can be easily incorporated into a quasi- and semi-classical descriptions of the equilibrium time correlation functions. This result is also to be considered in light of related treatments of the density operator, in particular the thermal Gaussian approximation [214] and the Feynman-Kleinert linearized path integral (FK-LPI) treatment [159]. In both, the Wigner transformed density operator is expressed as a single function rather than a superposition of Gaussian distributions.

6.3 Results

In this section we present some representative results obtained using Eqs. (6.13) and (6.14) for thermodynamic averages of spin variables and dynamic calculations of the correlation function, $\mathcal{C}_{zz}(t) = \mathrm{Re}\langle\sigma_z(0)\sigma_z(t)\rangle$. The dynamics are calculated using the quasi-classical Ehrenfest method, which propagates the system (bath) variables in the time-dependent mean-field of the bath (system) with neglect of the Moyal operator $e^{i\overleftrightarrow{\Lambda}/2\hbar}$. Via comparison with numerically exact results for $\mathcal{C}_{zz}(t)$, we illustrate the sensitivity of the Ehrenfest dynamics to the accurate rendering of the canonical distribution. Appendix 6.B provides details regarding the implementation of the Ehrenfest method.

Before turning to dynamical calculations, we show some representative calculations of thermodynamic averages of the population difference at equilibrium, $\langle\sigma_z\rangle$, for different realizations of the SB model. Fig. 6.1 illustrates the convergence of $\langle\sigma_z\rangle$ with the number of path integral steps for three cases where β or ξ is increased. As is evident from panel (a), $N = 0$ path integral slices is sufficient to obtain converged results in the high temperature, weakly coupled case. As panels (b) and (c) indicate, with decreasing temperature and increasing system-bath coupling, the number of path integral slices necessary for the converged calculation of thermodynamic averages increases. This is consistent with the fact that the error associated with the Trotter decomposition is of order $\mathcal{O}(N \cdot \exp\{-\beta[H_{ad}, H_{na}]/2N\})$, where the contribution from $[H_{ad}, H_{na}]$ generally grows with increasing ξ. Remarkably, even for significantly lower temperature and stronger system-bath coupling ($\beta = 10.0$ and $\xi = 5.0$), $N = 6$ is sufficient to obtain converged results. It is also worth noting that with increasing β and ξ, the polarization of the SB model with net bias becomes more severe, as is indicated

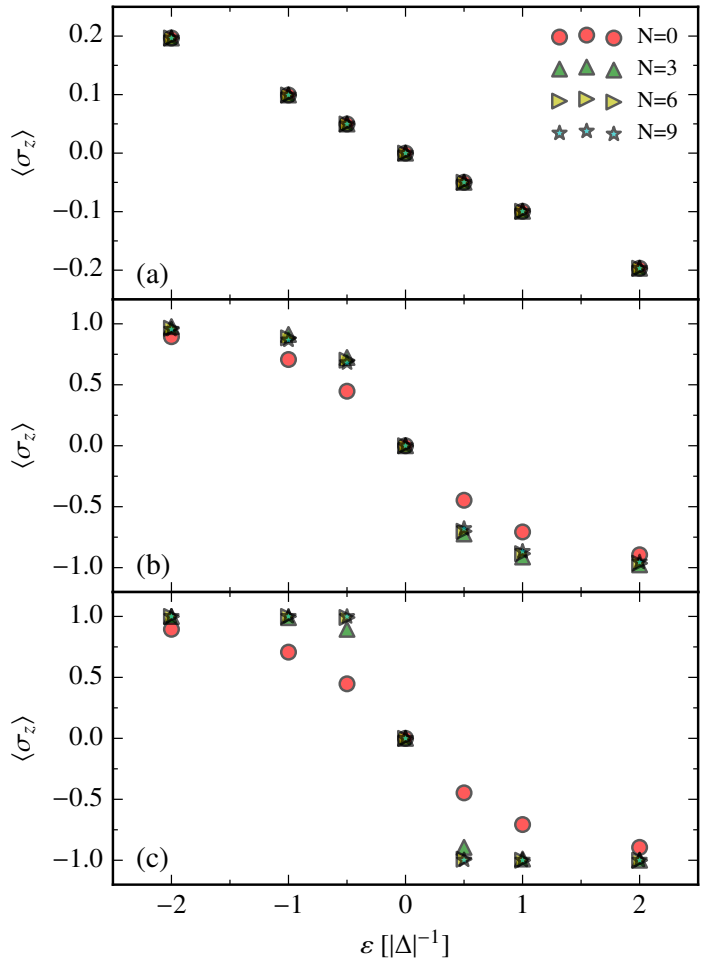

Figure 6.1: Calculation of the equilibrium population difference, $\langle\sigma_z\rangle$, as a function of the applied bias for the SB mode where $\Delta = \omega_c = 1$. For panel (a), $\beta = 0.1$, $\xi = 0.1$; for panel (b), $\beta = 5.0$, $\xi = 1.0$; for panel (c), $\beta = 10.0$, $\xi = 5.0$. The different markers correspond to the use of different number of path integral slices in the thermodynamic calculation.

by the difference in the magnitude of polarization from panel (a) to (b) and (c), and with the faster onset of full polarization with $|\varepsilon|$ between panels (b) and (c).

The current path integral approach to the density operator also permits the facile investigation of the dependence of thermodynamic averages on the continuous variation of parameters. Fig. 6.2 shows the dependence of the population difference as a function of β with the variation of the applied bias ε, the characteristic frequency of the bath ω_c, and the coupling between the system and bath ξ. Consistent with physical intuition, panel (a) shows that the system becomes more polarized at equilibrium with increasing bias and favors the polarized state with decreasing temperature. The dependence of the results on the variation of the characteristic frequency of the bath shown in panel (b) indicates that the faster the response of the bath (larger ω_c), the easier it becomes for the system to reach a stable polarized state, corresponding to the formation of a polaron. Finally, panel (c) shows the dependence of the polarization on the system-bath coupling. The results in panels (b) and (c) also agree with physical intuition which indicates that fast baths and strong system-bath coupling promote polaron formation.

The appropriate representation of the canonical density enabled by the path integral approach presented here also facilitates the calculation of equilibrium time correlation functions. For example, Fig. (6.3) shows the Ehrenfest results for $\mathcal{C}_{zz}(t)$ for the unbiased SB model ($\varepsilon = 0$) obtained using representations of the canonical density that differ in the number of path integral slices employed. Panel (a), which corresponds to a weak coupling, high temperature case, required only a minimal number of path integral slices ($N = 1$) for the convergence, indicating that the system and bath are indeed approximately independent. Also consistent with our expectations, the Ehrenfest method, which is most appropriate for

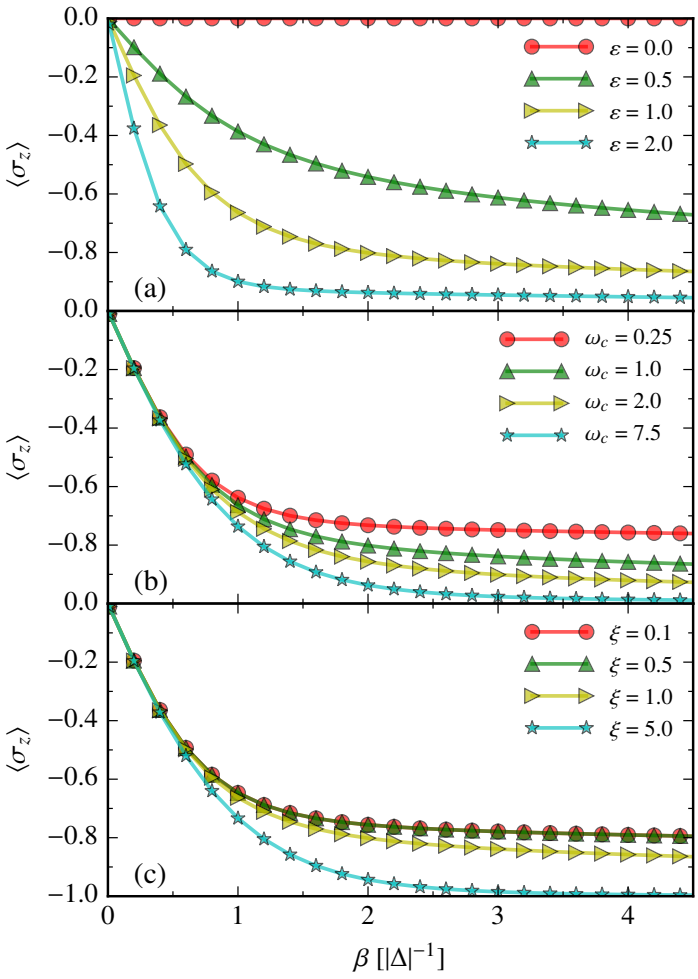

Figure 6.2: Expectation value for the equilibrium population difference as a function of inverse temperature β and variation in the applied bias ε, characteristic response time of the bath ω_c, and system-bath coupling strength ξ. For all panels, $\Delta = 1$ and $\alpha = -1$. For panel (a), $\omega_c = \xi = 1.0$; for $\varepsilon = \xi = 1.0$; and for (c), $\varepsilon = \omega_c = 1.0$.

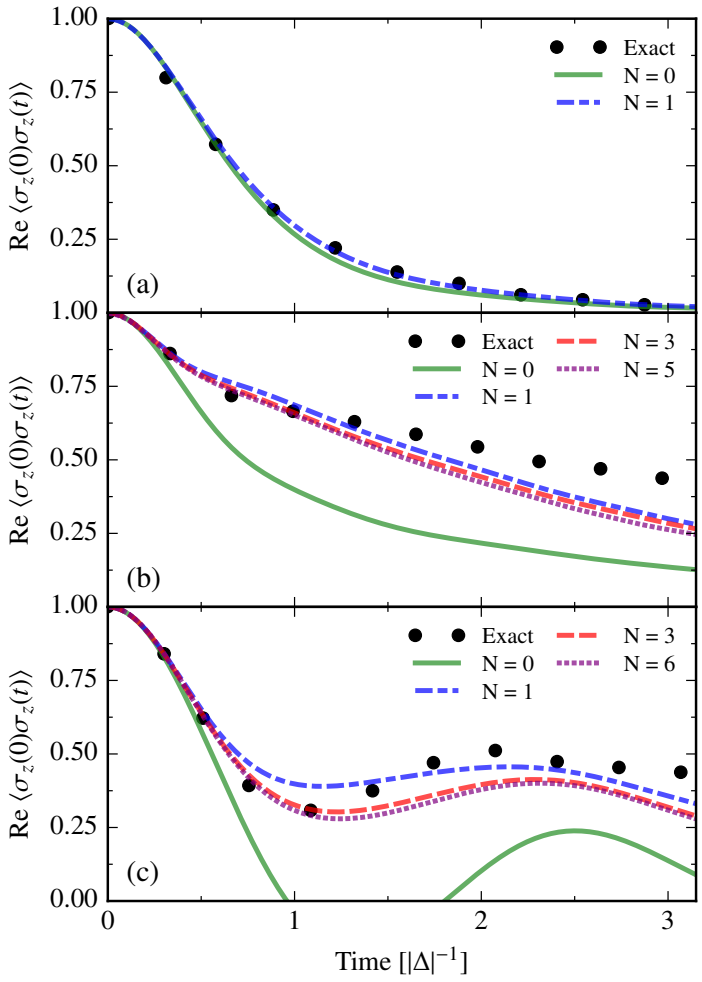

Figure 6.3: Representative Ehrenfest dynamics for correlation function, $\mathcal{C}_{zz}(t) = \mathrm{Re}\langle\sigma_z(0)\sigma_z(t)\rangle$, for several realizations of the unbiased ($\varepsilon = 0$) SB model. For all panels, $\Delta = -1$ and $\alpha = 1$. For panel (a), $\omega_c = 2.5$, $\beta = 0.2$, and $\xi = 0.32$; for (b), $\omega_c = 2.5$, $\beta = 1.6$, and $\xi = 0.51$; for (c), $\omega_c =$, $\beta = 1.6$, and $\xi = 2.55$. Exact results are obtained from Ref. [151].

systems at high temperature and weak system-bath coupling, is able to recover the exact dynamics easily. This picture changes drastically in panels (b) and (c), which correspond to lower temperatures and greater system-bath coupling. In these cases both the Ehrenfest method and the crude approximation for the density operator that treats the system and bath as approximately independent break down. For both panels, the number of path integral steps necessary for the convergence of the dynamics were $N = 5$ and 6, respectively. It is noteworthy that the accurate rendering of the equilibrium density operator resulted in improved accuracy for the dynamics for longer times, correctly capturing the slow relaxation in panels (b) and (c), as well as the short-time behavior up to $t = \Delta^{-1}$ quantitatively. Finally, we emphasize again that our scheme for the representation of the canonical distribution can be easily incorporated into other quasi- and semi-classical schemes; we have used the Ehrenfest method to illustrate the advantages of the current approach.

6.4 Conclusions

In this work we have derived an expression for the partial-Wigner transformed canonical density operator of the SB model which can be made arbitrarily accurate with increasing number of path integral slices, N. This approach can be used for the evaluation of thermodynamic averages and in conjunction with quasi- and semi-classical evolution methods for the calculation of equilibrium time correlation functions. Importantly, the current work permits the systematic testing of common approximations to the quantum canonical distribution function (e.g., the thermal Gaussian and FK-LPI approaches). Moreover, the generalization of the procedure presented here to an M-level system coupled linearly to a harmonic bath

is straightforward.

We have demonstrated the feasibility of the method in the calculation of thermodynamic averages for the spin and bath variables of the SB model, showing their dependence throughout parameter space. Using the current approach with the Ehrenfest method, we have illustrated sensitivity of the calculated dynamics to the accuracy of the representation of the canonical density operator, which is especially notable in the low temperature and high system-bath coupling regimes. The compatibility of the expressions provided here with quasi- and semi-classical dynamical schemes opens the door to more accurate semiclassical calculations of, for instance, transport coefficients and rate constants. We reserve the investigation of such properties for future publications.

Appendix

6.A Path Integral Treatment of the Canonical Density Operator

To derive an expression for $\rho_{a,b}(\mathbf{x}+\mathbf{s}/2, x-\mathbf{x}/2)$, necessary for the Wigner transformation of the canonical density operator in Eq. (6.10), we first obtain expressions for the matrix elements of the Boltzmann factor using the path integral procedure outlined in Sec. 6.2. Specifically, we use the Trotter decomposition in Eq. (6.11) and introduce resolutions of the identity in the system and bath subspaces, $\mathbf{1}_S = \sum_a |a\rangle \langle a|$ and $\mathbf{1}_B = \int d\mathbf{q} \, |\mathbf{q}\rangle \langle \mathbf{q}|$, so that the matrix elements of the Boltzmann factor can be rewritten as

$$\begin{aligned} F_{k_N,k_0}(\mathbf{Q}_N, \mathbf{Q}_0) &= \langle \mathbf{Q}_N | \langle k_N | \, e^{-\beta H} \, | k_0 \rangle \, | \mathbf{Q}_0 \rangle \\ &\approx \sum_{\{k_1,\ldots,k_{N-1}\}} \tilde{\mathcal{S}}_{k_N,k_0} \tilde{\mathcal{B}}_{k_N,k_0}(\mathbf{Q}_N, \mathbf{Q}_0), \end{aligned} \tag{6.15}$$

where

$$\tilde{\mathcal{S}}_{k_N,k_0} = \prod_{j=1}^{N} \langle k_j | \, e^{-\beta H_{ad}/N} \, | k_{j-1} \rangle \,, \tag{6.16}$$

$$\tilde{\mathcal{B}}_{k_N,k_0}(\mathbf{Q}_N, \mathbf{Q}_0) = \int d\mathbf{Q}_1 ... d\mathbf{Q}_{N-1} \prod_{j=1}^{N} \langle \mathbf{Q}_j | \, e^{-\beta H_{na}^{k_j}/2N} e^{-\beta H_{na}^{k_{j-1}}/2N} \, | \mathbf{Q}_{j-1} \rangle \,, \tag{6.17}$$

$$H_{na}^{k_j} = \frac{1}{2} \sum_l \Big[\hat{P}_l^2 + \omega_l^2 (\hat{Q}_l - b_{k_j}^{(l)})^2 \Big], \tag{6.18}$$

$$b_{k_j}^{(l)} = (-1)^{k_j} \alpha c_l / \omega_l^2. \tag{6.19}$$

In this notation,

$$\rho_{a,b}(\mathbf{x} + \mathbf{s}/2, x - \mathbf{x}/2) = \frac{F_{a,b}(\mathbf{x} + \mathbf{s}/2, \mathbf{x} - \mathbf{s}/2)}{Z}, \tag{6.20}$$

$$Z = \sum_a \int d\mathbf{x} \; F_{a,a}(\mathbf{x}, \mathbf{x}). \tag{6.21}$$

The the path integral unit, $\langle \mathbf{Q_n} | \, e^{-\beta H_{nd}^{k_n}/2N} e^{-\gamma H_{nd}^{k_m}/2N} \, | \mathbf{Q}_m \rangle$, in Eq. (6.17) takes the following form [18, 19],

$$\begin{aligned} \langle \mathbf{Q_n} | \, e^{-\beta H_{nd}^{k_n}/2N} e^{-\gamma H_{nd}^{k_m}/2N} \, | \mathbf{Q}_m \rangle = & \prod_{l=1}^{f} \sqrt{\frac{\omega_l}{2\pi \sinh(2\theta_l)}} \\ & \exp \Bigg[- \frac{\omega_l}{2 \sinh(2\theta_l)} \Big[[(\delta Q_n^{(l)})^2 + (\delta Q_m^{(l)})^2] \cosh(2\theta_l) + 2 \cosh(\theta_l) (\delta Q_n^{(l)} \\ & - \delta Q_m^{(l)}) \Delta b_{nm}^{(l)} - 2 \delta Q_n^{(l)} \delta Q_m^{(l)} + (\Delta b_{nm}^{(l)})^2 \cosh^2(\theta_l) \Big] \Bigg], \end{aligned} \tag{6.22}$$

where $\delta Q_n^{(l)} = Q^{(l)} - b_n^{(l)}$ is the difference between the coordinate of the l^{th} harmonic oscillator and its displacement due to the system-bath coupling, $\Delta b_{nm}^{(l)} = b_n^{(l)} - b_m^{(l)}$, and $\theta_l = \beta \omega_l / 2N$.

With the previous definitions, it is possible to obtain the following expression

$$\tilde{\mathcal{B}}_{a,b}(\mathbf{x}+\mathbf{s}/2, x-\mathbf{x}/2) = \prod_{l=1}^{f} \sqrt{\frac{\omega_l}{\pi \det[\mathbf{A}^{(l)}]}} \exp\left[-\gamma_x^{(l)}(x_l + \tilde{\kappa}_x^{(l)})^2 - \gamma_p^{(l)} s_l^2 + \tilde{\kappa}_p^{(l)} s_l - \tilde{\Lambda}^{(l)} \right], \tag{6.23}$$

where $\mathbf{A}^{(l)}$ is a tridiagonal $N-1 \times N-1$ matrix whose diagonal and off-diagonal entries are equal to 2 and $-\mathrm{sech}(2\theta_l)$, respectively. For $N < 2$, $\det[\mathbf{A}^{(l)}] = 1$. The path-dependent quantities above (marked by a tilde) take the forms,

$$\tilde{\kappa}_p^{(l)} = \begin{cases} -\frac{\omega_l}{2\tanh(2\theta_l)} \left[\frac{\cosh(\theta_l)}{\cosh(2\theta_l)} [(\Delta b_{N,N-1}^{(l)} + \Delta b_{1,0}^{(l)}) - (\tilde{\boldsymbol{\delta}}_{N-1}^{(l)} - \tilde{\boldsymbol{\delta}}_1^{(l)})] - \eta_l \Delta b_{N,0}^{(l)} \right] & : \quad N \geq 2, \\ -\frac{\omega_l}{\tanh(2\theta_l)} \left[\frac{\cosh(\theta_l)}{\cosh(2\theta_l)} \right] \Delta b_{1,0}^{(l)} [1 - \cosh(\theta_l)] & : \quad N = 1, \end{cases} \tag{6.24}$$

$$\tilde{\kappa}_x^{(l)} = \begin{cases} \frac{\cosh(\theta_l)}{2\cosh(2\theta_l)} \frac{[(\Delta b_{N,N-1}^{(l)} - \Delta b_{1,0}^{(l)}) - (\tilde{\boldsymbol{\delta}}_{N-1}^{(l)} + \tilde{\boldsymbol{\delta}}_1^{(l)})]}{\nu_l} - \frac{b_N^{(l)} + b_0^{(l)}}{2} & : \quad N \geq 2, \\ -\frac{b_N^{(l)} + b_0^{(l)}}{2} & : \quad N = 1, \end{cases} \tag{6.25}$$

$$\tilde{\Lambda}^{(l)} = \begin{cases} \frac{\omega_l}{4\tanh(2\theta_l)} \left[\frac{1+\cosh(2\theta_l)}{\cosh(2\theta_l)} \left[\sum_{j=1}^{N} [\tilde{\boldsymbol{\delta}} b_{j,j-1}^{(l)}]^2 - \frac{\tilde{\mathbf{j}}_l^T \cdot \mathbf{A}_l^{-1} \cdot \tilde{\mathbf{j}}_l}{\cosh(2\theta_l)} \right] \right. \\ \qquad -2\frac{\cosh(\theta_l)}{\cosh(2\theta_l)} \left[(\Delta b_{N,N-1}^{(l)} + \Delta b_{1,0}^{(l)}) - (\tilde{\boldsymbol{\delta}}_{N-1}^{(l)} - \tilde{\boldsymbol{\delta}}_1^{(l)}) \right] \Delta b_{N,0}^{(l)} \\ \qquad \left. -\left[\frac{\cosh(\theta_l)}{\cosh(2\theta_l)} \right]^2 \frac{[(\Delta b_{N,N-1}^{(l)} - \Delta b_{1,0}^{(l)}) - (\tilde{\boldsymbol{\delta}}_{N-1}^{(l)} + \tilde{\boldsymbol{\delta}}_1^{(l)})]^2}{\nu_l} + \eta_l [\Delta b_{N,0}^{(l)}]^2 \right] & : \quad N \geq 2, \\ \frac{\omega_l}{\tanh(2\theta_l)} \left[\frac{\cosh(\theta_l)}{\cosh(2\theta_l)} \right] [\Delta b_{1,0}^{(l)}]^2 [1 - \cosh(\theta_l)] & : \quad N = 1, \end{cases} \tag{6.26}$$

where

$$\tilde{\mathbf{j}}_l = \begin{bmatrix} \Delta b_{21}^{(l)} - \Delta b_{10}^{(l)} \\ \Delta b_{32}^{(l)} - \Delta b_{21}^{(l)} \\ \vdots \\ \Delta b_{N,N-1}^{(l)} - \Delta b_{N-1,N-2}^{(l)} \end{bmatrix}, \tag{6.27}$$

and $\tilde{\boldsymbol{\delta}}^{(l)} = \mathbf{j}_l^T \cdot \mathbf{A}_l^{-1} / \cosh(\theta_l)$. Also, when $N = 0$, $\tilde{\kappa}_p^{(l)} = \tilde{\kappa}_x^{(l)} = \tilde{\Lambda}^{(l)} = 0$.

The path-independent quantities take the following forms,

$$\eta_l = 1 - \frac{[\mathbf{A}_l^{-1}]_{1,1} - [\mathbf{A}_l^{-1}]_{1,N-1}}{\cosh^2(2\theta_l)}, \tag{6.28}$$

$$\nu_l = 1 - \frac{[\mathbf{A}_l^{-1}]_{1,1} + [\mathbf{A}_l^{-1}]_{1,N-1}}{\cosh^2(2\theta_l)}, \tag{6.29}$$

$$\gamma_p^{(l)} = \frac{\tanh(2\theta_l)}{\omega_l \eta_l}, \tag{6.30}$$

$$\gamma_x^{(l)} = \frac{\omega_l \nu_l}{\tanh(2\theta_l)}. \tag{6.31}$$

For $N < 2$, $\eta_l = \nu_l = 1$.

Substituting Eqs. (6.23) and (6.16) into Eq. (6.15), setting $\mathbf{s} = 0$, and performing the integration in Eq. (6.21) leads to the following expression for the partition function,

$$Z = \Big[\sum_a \mathcal{W}_{a,a}\Big] \prod_{l=1}^{f} \Big[2\cosh(2\theta_l)\eta_l \det[\mathbf{A}_l]\Big]^{-1/2}, \tag{6.32}$$

where the path-dependent weights take the form $\tilde{W}_{a,b} = \tilde{\mathcal{S}}_{a,b} \exp[-\sum_l \tilde{\Lambda}_{a,b}^{(l)}]$, and $\mathcal{W}_{a,b} = \sum_{paths} \tilde{W}_{a,b}$.

One final integration over $\mathbf{s}$ in Eq. (6.10) leads to the following expressions for the partial

bath distribution and normalization factor,

$$\mathcal{R}^W_{a,b}(\mathbf{x},\mathbf{p}) = \left[\prod_{l=1}^{F}\frac{\sqrt{\nu_l/\eta_l}}{\pi}\right]\sum_{\{k_1,\ldots,k_{N-1}\}}\frac{\tilde{W}_{a,b}}{\mathcal{W}_{a,b}}\prod_{l=1}^{F}\exp\Big[-\gamma_p^{(l)}(p_l+i\tilde{\kappa}_p^{(l)})^2-\gamma_x^{(l)}(x_l+\tilde{\kappa}_x^{(l)})^2\Big], \tag{6.33}$$

$$N_{ab} = \frac{\mathcal{W}_{a,b}}{\sum_a \mathcal{W}_{a,a}}. \tag{6.34}$$

6.B Ehrenfest method

The Ehrenfest method is a wavefunction-based approach where the system (bath) evolves in the mean field of the bath (system). In addition, this scheme assumes that the bath dynamics are correctly captured by classical mechanics. One may rigorously formulate the Ehrenfest method by first performing a partial Wigner transform with respect to the bath degrees of freedom of the dynamical object to be calculated, e.g., nonequilibrium average or time correlation function,

$$\begin{aligned} C_{AB}(t) &= \mathrm{Tr}[\mathcal{A}_S(0)\mathcal{A}_B(0)\mathcal{B}_S(t)\mathcal{B}_B(t)] \\ &\approx \int d\mathbf{xp}\ \mathcal{A}_B^W\mathcal{B}_B^W(t)\mathrm{Tr}_S[\mathcal{A}_S(0)\mathcal{B}_S(t)] \end{aligned} \tag{6.35}$$

where X_S (X_B) is a generic system (bath) operator.

The heart of the approximation in the Ehrenfest method lies in the dynamical treatment of the operators. In this scheme, the time-dependence is given by the equations of motion for the system and bath. In the case of the system, the wavefunction is evolved via the quantum Liouville equation under the influence of a modified Hamiltonian,

$$\frac{d}{dt}\rho_S(t) = -i[H_S^{Eh},\rho(t)], \tag{6.36}$$

where

$$H_{S,Eh}(t) = [\varepsilon + \lambda^{cl}(t)]\sigma_z + \Delta\sigma_x, \tag{6.37}$$

is the modified system Hamiltonian and $\lambda^{cl}(t) = \alpha \sum_k c_k Q_k(t)$ is the classical fluctuation in the bias provided by the classical treatment of the bath. Here, $\rho_S(0)$ is the initial density matrix for the system. In Eq. (6.35), this corresponds to operator $\mathcal{A}(0)$. Since the Ehrenfest is a wavefunction based method, initial conditions corresponding to coherences, $\rho_S(0) = |i\rangle \langle j|$ where $i \neq j$, must first be sampled correctly for the Ehrenfest method to yield appropriate results. Details regarding the generation may be found in Ref. [104].

The equations of motion for the bath variables are given by the classical Hamilton's equations subject to the time-dependent Hamiltonian,

$$\frac{dP_k}{dt} = -\frac{\partial H_B^{Eh}}{\partial Q_k}, \tag{6.38}$$

$$\frac{dQ_k}{dt} = \frac{\partial H_B^{Eh}}{\partial P_k}, \tag{6.39}$$

where

$$H_B^{Eh}(t) = \frac{1}{2}\sum_k \left[P_k^2 + \omega_k^2 Q_k + 2\alpha\bar{\sigma}_z(t)c_k Q_k\right], \tag{6.40}$$

and $\bar{\sigma}_z(t) = \mathrm{Tr}_S[\rho_S(t)\sigma_z]$

Given the previous considerations, $\mathcal{C}_{zz}(t)$ takes the form,

$$\begin{aligned} C_{zz}(t) &= \mathrm{Re}\ \mathrm{Tr}[\rho\sigma_z(0)\sigma_z(t)] \\ &= \mathrm{Re}\sum_a \Bigg[N_{a,1}\int d\mathbf{x}d\mathbf{p}\ \mathcal{R}_{a,1}^W(\mathbf{x},\mathbf{p})\mathrm{Tr}_S[|a\rangle\langle 1|\,\sigma_z(t)] \\ &\qquad + N_{a,2}\int d\mathbf{x}\mathbf{p}\ \mathcal{R}_{a,2}^W(\mathbf{x},\mathbf{p})\mathrm{Tr}_S[|a\rangle\langle 1|\,\sigma_z(t)]\Bigg]. \end{aligned} \tag{6.41}$$

To calculate $\mathcal{C}_{zz}(t)$, a second-order Runge-Kutta scheme was implemented. During individual time steps, $\bar{\sigma}_z(t)$ is kept constant for the evolution of the bath, while $\lambda^{cl}(t)$ is kept constant during the evolution of the system. Over a half time step, the equations for the classical variables take the forms,

$$Q_k\left(t+\frac{\delta t}{2}\right) = \gamma_k(t)\cos\left(\frac{\omega_k \delta t}{2}\right) - \frac{\alpha c_k}{\omega_k^2}\bar{\sigma}_z(t) + \frac{P_k(t)}{\omega_k}\cos\left(\frac{\omega_k \delta t}{2}\right), \tag{6.42}$$

and

$$P_k\left(t+\frac{\delta t}{2}\right) = P_k(t)\cos\left(\frac{\omega_k \delta t}{2}\right) + \omega_k \gamma_k(t)\sin\left(\frac{\omega_k \delta t}{2}\right), \tag{6.43}$$

where

$$\gamma_k(t) = Q_k(t) + \frac{\alpha c_k}{\omega_k^2}\bar{\sigma}_z(t). \tag{6.44}$$

Convergence for the correlation functions was achieved using $\sim 5\times 10^4 - 10^5$ trajectories.

Bibliography

[1] A. J. Leggett, S Chakravarty, A Dorsey, M Fisher, A Garg, and W Zwerger, Rev. Mod. Phys. **59**, 1 (1987).

[2] U Weiss, *Quantum Dissipative Systems* (World Scientific, 1992).

[3] P. W. Anderson, Phys. Rev. **124**, 41 (1961).

[4] G. D. Mahan, *Many-Particle Physics* (Plenum Press, 1990).

[5] M. Rasetti, ed., *The Hubbard Model: Recent Results.* (World Scientific, 1991).

[6] S. Sachdev, *Quantum Phase Transitions*, Second (Cambridge University Press, New York, 2011).

[7] T. Giamarchi, *Quantum Physics in One Dimension* (Oxford University Press, New York, 2004).

[8] E. Feenberg, *Theory of quantum fluids* (Academic Press, New York, 1969).

[9] D. Pines and P. Nozieres, *The theory of quantum liquids, Vol. 1 and 2* (Advanced Book Classics, 1966).

[10] A. Garg, J. N. Onuchic, and V. Ambegaokar, J. Chem. Phys. **83**, 4491 (1985).

[11] Y. Georgievskii, C.-P. Hsu, and R. a. Marcus, J. Chem. Phys. **110**, 5307 (1999).

[12] M. Thorwart and P. Hänggi, Phys. Rev. A **65**, 012309 (2001).

BIBLIOGRAPHY

[13] T. A. Costi and R. H. McKenzie, Phys. Rev. A **68**, 034301 (2003).

[14] M. J. Storcz and F. K. Wilhelm, Phys. Rev. A **67**, 042319 (2002).

[15] S. Mukamel, *Principles of Nonlinear Optical Spectroscopy* (Oxford University Press, New York, 1995).

[16] J. Adolphs and T. Renger, Biophys. J. **91**, 2778 (2006).

[17] A. Ishizaki and G. R. Fleming, Proc. Natl. Acad. Sci. **106**, 17255 (2009).

[18] N. Makri, Chem. Phys. Lett. **193**, 435 (1992).

[19] D. E. Makarov and N. Makri, Chem. Phys. Lett. **221**, 482 (1994).

[20] N. Makri and D. E. Makarov, J. Chem. Phys. **102**, 4600 (1995).

[21] N. Makri and D. E. Makarov, J. Chem. Phys. **102**, 4611 (1995).

[22] R. Kubo, "A Stochastic Theory of Line Shape," in *Adv. chem. phys.* Vol. 25 (1969), p. 101.

[23] Y. Tanimura and R. Kubo, J. Phys. Soc. Jpn. **58**, 101 (1989).

[24] A. Ishizaki and G. R. Fleming, J. Chem. Phys. **130**, 234111 (2009).

[25] H.-D. Meyer, U Manthe, and L. S. Cederbaum, Chem. Phys. Lett. **165**, 73 (1990).

[26] M Beck, A Jäckle, G. A. Worth, and H.-D. Meyer, Phys. Rep. **324**, 1 (2000).

[27] H Wang, M Thoss, and W. H. Miller, J. Chem. Phys. **115**, 2979 (2001).

[28] M. Thoss, H. Wang, and W. H. Miller, J. Chem. Phys. **115**, 2991 (2001).

[29] H. Wang and M. Thoss, J. Chem. Phys. **119**, 1289 (2003).

[30] D. Thirumalai and B. Berne, Comput. Phys. Commun. **63**, 415 (1991).

[31] J. Doll, D. Freeman, and T. Beck, "Equilibrium and dynamical Fourier path integral methods," in *Adv. chem. phys*, Vol. 78 (1990), p. 61.

[32] C. H. Mak and R. Egger, "Monte Carlo Methods for Real-Time Path Integration," in *Adv. chem. phys.* Vol. 93 (1996), p. 39.

[33] E. Gull, A. J. Millis, A. I. Lichtenstein, A. N. Rubtsov, M. Troyer, and P. Werner, Rev. Mod. Phys. **83**, 349 (2011).

[34] G. Vidal, Phys. Rev. Lett. **91**, 147902 (2003).

[35] G. Vidal, Phys. Rev. Lett. **93**, 040502 (2004).

[36] S. R. White and A. E. Feiguin, Phys. Rev. Lett. **93**, 076401 (2004).

[37] A. J. Daley, C. Kollath, U. Schollwöck, and G. Vidal, J. Stat. Phys., P04005 (2004).

[38] U. Schollwöck, Ann. Phys. **326**, 96 (2011).

[39] G. Cohen, E. Gull, D. R. Reichman, and A. J. Millis, Phys. Rev. Lett. **112**, 146802 (2014).

[40] G. Cohen, D. R. Reichman, A. J. Millis, and E. Gull, Phys. Rev. B **89**, 115139 (2014).

[41] G. Cohen, E. Gull, D. R. Reichman, and A. J. Millis, Phys. Rev. Lett. **115**, 266802 (2015).

[42] F Bloch, Phys. Rev. **105**, 1206 (1957).

[43] A. G. Redfield, Adv. Magn. Opt. Reson. **1**, 1 (1965).

[44] H.-D. Meyer and W. H. Miller, J. Chem. Phys. **70**, 3214 (1979).

[45] G. Stock and M. Thoss, Phys. Rev. Lett. **78**, 578 (1997).

[46] W. H. Miller, J. Phys. Chem. A **102**, 793 (2001).

[47] W. H. Miller, J. Phys. Chem. A **105**, 2942 (2001).

[48] W. H. Miller, J. Phys. Chem. A **113**, 1405 (2009).

[49] J Liu and W. H. Miller, J. Chem. Phys. **126**, 234110 (2007).

[50] J. Cao and G. A. Voth, J. Chem. Phys. **100**, 5093 (1994).

[51] J. Cao and G. A. Voth, J. Chem. Phys. **100**, 5106 (1994).

[52] S. Jang and G. A. Voth, J. Chem. Phys. **111**, 2357 (1999).

[53] S. Jang and G. A. Voth, J. Chem. Phys. **111**, 2371 (1999).

[54] I. R. Craig and D. E. Manolopoulos, J. Chem. Phys. **121**, 3368 (2004).

[55] I. R. Craig and D. E. Manolopoulos, J. Chem. Phys. **122**, 084106 (2005).

[56] I. R. Craig and D. E. Manolopoulos, J. Chem. Phys. **123**, 034102 (2005).

[57] S. Habershon, D. E. Manolopoulos, T. E. Markland, and T. F. Miller, Annu. Rev. Phys. Chem. **64**, 387 (2013).

[58] S. Egorov and J. L. Skinner, Chem. Phys. Lett. **293**, 469 (1998).

[59] S. a. Egorov, K. F. Everitt, and J. L. Skinner, J. Phys. Chem. A **103**, 9494 (1999).

[60] Q. Shi and E. Geva, J. Phys. Chem. A **107**, 9059 (2003).

[61] R. B. Gerber, V Buch, and M. A. Ratner, J. Chem. Phys. **77**, 3022 (1982).

[62] G. Stock, J. Chem. Phys. **103**, 1561 (1995).

[63] J. C. Tully, J. Chem. Phys. **55**, 562 (1971).

[64] J. C. Tully, J. Chem. Phys. **93**, 1061 (1990).

[65] H. Wang, X. Sun, and W. H. Miller, J. Chem. Phys. **108**, 9726 (1998).

[66] X. Sun, H. Wang, and W. H. Miller, J. Chem. Phys. **109**, 7064 (1998).

[67] Q. Shi and E. Geva, J. Chem. Phys. **118**, 8173 (2003).

[68] E. Rabani and D. R. Reichman, J. Chem. Phys. **116**, 6271 (2002).

[69] D. R. Reichman and E. Rabani, J. Chem. Phys. **116**, 6279 (2002).

[70] E. Rabani and D. R. Reichman, J. Chem. Phys. **120**, 1458 (2004).

[71] E. Rabani and D. R. Reichman, Annu. Rev. Phys. Chem. **56**, 157 (2005).

[72] T. E. Markland, J. A. Morrone, B. J. Berne, K. Miyazaki, E. Rabani, and D. R. Reichman, Nat. Phys. **7**, 134 (2011).

[73] M. Jarrell and J. E. Gubernatis, Phys. Rep. **269**, 133 (1996).

[74] E Gallicchio, B. J. Berne, E Gallicchio, and B. J. Berne, J. Chem. Phys. **105**, 7064 (1996).

[75] M. Boninsegni, J. Low Temp. Phys. **104**, 339 (1996).

[76] E. Sim, G. Krilov, and B. J. Berne, J. Phys. Chem. A **105**, 2824 (2001).

[77] G. Krilov, E. Sim, and B. J. Berne, J. Chem. Phys. **114**, 1075 (2001).

[78] A. A. Golosov, D. R. Reichman, and E. Rabani, J. Chem. Phys. **118**, 457 (2003).

[79] B. B. Laird, J. Budimir, and J. L. Skinner, J. Chem. Phys. **94**, 4391 (1991).

[80] H.-P. Breuer and F. Petruccione, *The Theory of Open Quantum Systems* (Oxford University Press, Oxford, 2007).

[81] A. Montoya-Castillo, T. C. Berkelbach, and D. R. Reichman, J. Chem. Phys. **143**, 194108 (2015).

[82] N. Makri, Annu. Rev. Phys. Chem. **50**, 167 (1999).

[83] W. H. Miller, J. Chem. Phys. **125**, 132305 (2006).

[84] R. Kapral, Annu. Rev. Phys. Chem. **57**, 129 (2006).

[85] L. Turi and P. J. Rossky, Chem. Rev. **112**, 5641 (2012).

[86] A. V. Akimov, A. J. Neukirch, and O. V. Prezhdo, Chem. Rev. **113**, 4496 (2013).

[87] L. Wang, R. Long, and O. V. Prezhdo, Annu. Rev. Phys. Chem. **66**, 549 (2015).

[88] B. J. Berne, J. P. Boon, and S. A. Rice, J. Chem. Phys. **45**, 1086 (1966).

[89] B. J. Berne, M. E. Tuckerman, J. E. Straub, and A. L. R. Bug, J. Chem. Phys. **93**, 5084 (1990).

[90] X. Chen and R. J. Silbey, J. Chem. Phys. **132**, 204503 (2010).

[91] H. Dekker, Phys. Rev. A **35**, 1436 (1987).

[92] Y. C. Cheng and R. J. Silbey, J. Phys. Chem. B **109**, 21399 (2005).

[93] Q. Shi and E. Geva, J. Chem. Phys. **119**, 12063 (2003).

[94] M.-L. Zhang, B. J. Ka, and E. Geva, J. Chem. Phys. **125**, 044106 (2006).

[95] G. Cohen and E. Rabani, Phys. Rev. B **84**, 075150 (2011).

[96] G. Cohen, E. Y. Wilner, and E. Rabani, New J. Phys. **15**, 073018 (2013).

[97] G. Cohen, E. Gull, D. R. Reichman, A. J. Millis, and E. Rabani, Phys. Rev. B **87**, 195108 (2013).

[98] E. Y. Wilner, H. Wang, G. Cohen, M. Thoss, and E. Rabani, Phys. Rev. B **88**, 045137 (2013).

[99] E. Y. Wilner, H. Wang, M. Thoss, and E. Rabani, Phys. Rev. B **89**, 205129 (2014).

[100] Q. Shi and E. Geva, J. Chem. Phys. **120**, 10647 (2004).

[101] A. Kelly and T. E. Markland, J. Chem. Phys. **139**, 014104 (2013).

[102] A. Kelly, N. Brackbill, and T. E. Markland, J. Chem. Phys. **142**, 094110 (2015).

[103] W. C. Pfalzgraff, A. Kelly, and T. E. Markland, J. Phys. Chem. Lett. **6**, 4743 (2015).

[104] A. Montoya-Castillo and D. R. Reichman, J. Chem. Phys. **144**, 184104 (2016).

[105] A. Montoya Castillo and D. R. Reichman, "Approximate but accurate quantum dynamics from the Mori formalism: II. Equilibrium time correlation functions," 2016.

[106] A. Kelly, A. Montoya-Castillo, L. Wang, and T. E. Markland, J. Chem. Phys. **144**, 184105 (2016).

[107] A. Nitzan, *Chemical Dynamics in Condensed Phases: Relaxation, Transfer, and Reactions in Condensed Molecular Systems* (Oxford University Press, New York, 2006).

[108] B. R. Landry and J. E. Subotnik, J. Chem. Phys. **142**, 104102 (2015).

[109] T. C. Berkelbach, D. R. Reichman, and T. E. Markland, J. Chem. Phys. **136**, 34113 (2012).

[110] W. T. Pollard, A. K. Felts, and R. A. Friesner, "The Redfield Equation in Condensed-Phase Quantum Dynamics," in *Adv. chem. phys.* Vol. 93 (1996), p. 77.

[111] D. V. Matyushov, J. Chem. Phys. **139**, 25102 (2013).

[112] H Bässler, Phys. Stat. Sol. (b). **175**, 15 (1993).

[113] T. C. Berkelbach, T. E. Markland, and D. R. Reichman, J. Chem. Phys. **136**, 84104 (2012).

[114] G. S. Engel, T. R. Calhoun, E. L. Read, T.-K. Ahn, T. Mancal, Y.-C. Cheng, R. E. Blankenship, and G. R. Fleming, Nature **446**, 782 (2007).

[115] T.-M. Chang and J. L. Skinner, Physica A **193**, 483 (1993).

[116] R. Zwanzig, J. Chem. Phys. **34**, 1931 (1961).

[117] S. Jang, J. Cao, and R. J. Silbey, J. Chem. Phys. **116**, 2705 (2002).

[118] F. Shibata and T. Arimitsu, J. Phys. Soc. Jpn. **49**, 891 (1980).

[119] B Yoon, J. M. Deutch, and H. F. Jack, J. Chem. Phys. **62**, 4687 (1975).

[120] S. Mukamel, I. Oppenheim, and J. Ross, Phys. Rev. A **17**, 1988 (1978).

[121] H. P. Breuer, B. Kappler, and F. Petruccione, Phys. Rev. A **59**, 1633 (1999).

[122] R. D. Coalson and D. G. Evans, Chem. Phys. **296**, 117 (2004).

[123] M. Yang and G. R. Fleming, Chem. Phys. **275**, 355 (2002).

[124] M. A. Palenberg, R. J. Silbey, C. Warns, and P. Reineker, J. Chem. Phys. **114**, 4386 (2001).

[125] M. Hillery, R. F. O'Connell, M. O. Scully, and E. P. Wigner, Phys. Rep. **106**, 121 (1984).

[126] J. C. Tully, Farad. Discuss. **110**, 407 (1998).

[127] S. Nakajima, Prog. Theor. Phys. **20**, 948 (1958).

[128] R. Zwanzig, J. Chem. Phys. **33**, 1338 (1960).

[129] H Grabert, *Projection Operator Techniques in Nonequilibrium Statistical Mechanics* (Springer, Berlin, 1982).

[130] E. Fick and G. Sauermann, *The Quantum Statistics of Dynamic Processes* (Springer-Verlag, Berlin, 1990).

[131] S. Jang, J. Chem. Phys. **135**, 34105 (2011).

[132] Y. Tanimura, J. Chem. Phys. **142**, 144110 (2015).

[133] A. Ivanov and H.-P. Breuer, Phys. Rev. A **92**, 032113 (2015).

[134] T. Yamamoto, J. Chem. Phys. **33**, 281 (1960).

[135] J. A. Poulsen, G. Nyman, and P. J. Rossky, Proc. Natl. Acad. Sci. **102**, 6709 (2005).

[136] C Aslangul, N Pottier, and D Saint-James, J. Phys. **46**, 2031 (1985).

[137] M. Sparpaglione and S. Mukamel, J. Chem. Phys. **88**, 3263 (1988).

[138] L. Kidon, E. Y. Wilner, and E. Rabani, J. Phys. Chem. **143**, 234110 (2015).

[139] R. Grunwald, A. Kelly, and R. Kapral, "Quantum Dynamics in Almost Classical Environments," in *Energy transf. dyn. biomater. syst.* (2009), p. 383.

[140] A. A. Golosov and D. R. Reichman, J. Chem. Phys. **114**, 1065 (2001).

[141] P. V. Parandekar and J. C. Tully, J. Chem. Theory Comput. **2**, 229 (2006).

[142] H. Mori, Prog. Theor. Phys. **33**, 423 (1965).

[143] D. R. Reichman and P. Charbonneau, J. Stat. Mech., P05013 (2005).

[144] Q. Shi and E. Geva, J. Chem. Phys. **121**, 3393 (2004).

[145] K. Imre, J. Math. Phys. **8**, 1097 (1967).

[146] R. Kubo, M. Toda, and N. Hashitsume, *Statistical Physics II. Nonequilibrium Statistical Mechanics* (Springer-Verlag, Berlin, 1991).

[147] R. Kubo, J. Phys. Soc. Jpn. **12**, 570 (1957).

[148] R. Kubo, M. Yokota, and S. Nakajima, J. Phys. Soc. Jpn. **12**, 1203 (1957).

[149] G. A. Voth, D. Chandler, and W. H. Miller, J. Phys. Chem. **93**, 7009 (1989).

[150] C. H. Mak and D. Chandler, Phys. Rev. A **41**, 5709 (1990).

[151] C. H. Mak and D. Chandler, Phys. Rev. A **44**, 2352 (1991).

[152] R Egger and U Weiss, Z. Phys. B **89**, 97 (1992).

[153] R. Egger and C. H. Mak, Phys. Rev. B **50**, 15210 (1994).

[154] J. Shao and N. Makri, Chem. Phys. **268**, 1 (2001).

[155] J. Shao and N. Makri, J. Chem. Phys. **116**, 507 (2002).

[156] Y. Tanimura, J. Chem. Phys. **141**, 044114 (2014).

[157] L. Song and Q. Shi, J. Chem. Phys. **142**, 174103 (2015).

[158] C Aslangul, N Pottier, and D Saint-James, J. Phys. **47**, 1657 (1986).

[159] J. A. Poulsen, G. Nyman, and P. J. Rossky, J. Chem. Phys. **119**, 12179 (2003).

[160] J. Liu and W. H. Miller, J. Chem. Phys. **128**, 144511 (2008).

[161] J. Liu and W. H. Miller, J. Chem. Phys. **131**, 074113 (2009).

[162] A. Montoya-Castillo and D. R. Reichman, "Exact Wigner representation of the canonical distribution for systems linearly coupled to harmonic baths," 2016.

[163] P. V. Parandekar and J. C. Tully, J. Chem. Phys. **122**, 94102 (2005).

[164] P. C. Martin and S. Yip, Phys. Rev. **170**, 151 (1968).

[165] G. Harp and B. Berne, Phys. Rev. A **2**, 975 (1970).

[166] D. Levesque and L. Verlet, Phys. Rev. A **2**, 2514 (1970).

[167] J.-P. Boon and S. A. Rice, J. Chem. Phys. **47**, 2480 (1967).

[168] T.-W. Nee and R. Zwanzig, J. Chem. Phys. **52**, 6353 (1970).

[169] T. E. Markland, J. A. Morrone, K. Miyazaki, B. J. Berne, D. R. Reichman, and E. Rabani, J. Chem. Phys. **136**, 074511 (2012).

[170] B. U. Felderhof, J. M. Deutch, and U. M. Titulaer, J. Chem. Phys. **63**, 740 (1975).

[171] K. S. Schweizer, J. Chem. Phys. **91**, 5802 (1989).

[172] D. Chandler, J. Chem. Phys. **68**, 2959 (1978).

[173] C. Hijón, P. Español, E. Vanden-Eijnden, and R. Delgado-Buscalioni, Farad. Discuss. **144**, 301 (2010).

[174] A. J. Chorin, O. H. Hald, and R Kupferman, Proc. Natl. Acad. Sci. **97**, 2968 (2000).

[175] D. T. Schmitt and M. Schulz, Phys. Rev. E **73**, 056204 (2006).

[176] M. Niemann, T. Laubrich, E. Olbrich, and H. Kantz, Phys. Rev. E **77**, 011117 (2008).

[177] D Venturi and G. E. Karniadakis, Proc. R. Soc. A **470**, 20130754 (2014).

[178] E. Y. Wilner, H. Wang, M. Thoss, and E. Rabani, Phys. Rev. B **92**, 195143 (2015).

[179] A. D. McLachlan, Mol. Phys. **8**, 39 (1964).

[180] R. Kapral, J. Phys. Condens. Matter **27**, 073201 (2015).

[181] H. Kim, A. Nassimi, and R. Kapral, J. Chem. Phys. **129**, 84102 (2008).

[182] C. Y. Hsieh and R. Kapral, J. Chem. Phys. **137**, 22A507 (2012).

[183] N. G. V. Kampen, *Stochastic Processes in Physics and Chemistry*, Third (Elsevier, Amsterdam, 2007).

[184] G. A. Voth, D. Chandler, and W. H. Miller, J. Chem. Phys. **91**, 7749 (1989).

[185] K. Binder and D. W. Heermann, *Monte Carlo Simulation in Statistical Physics*, Fifth (Springer-Verlag, Heidelberg, 2010).

[186] J. A. Barker, J. Chem. Phys. **70**, 2914 (1979).

[187] M. Parrinello and A. Rahman, J. Chem. Phys. **80**, 860 (1984).

[188] K. G. Wilson, Rev. Mod. Phys. **47**, 773 (1975).

[189] R. Bulla, T. A. Costi, and T. Pruschke, Rev. Mod. Phys. **80**, 395 (2008).

[190] S. R. White, Phys. Rev. Lett. **102**, 1 (2009).

[191] T. Barthel, U. Schollwöck, and S. White, Phys. Rev. B **79**, 245101 (2009).

[192] E. Wigner, Phys. Rev. **40**, 749 (1932).

[193] E. J. Heller, J. Chem. Phys. **65**, 1289 (1976).

[194] A. Polkovnikov, Ann. Phys. **325**, 1790 (2010).

[195] J. L. Skinner and K. Park, J. Phys. Chem. B **105**, 6716 (2001).

[196] H. Kim and P. J. Rossky, J. Phys. Chem. B **106**, 8240 (2002).

[197] K. K. G. Smith, J. A. Poulsen, G. Nyman, and P. J. Rossky, J. Chem. Phys. **142**, 244112 (2015).

[198] P. A. Frantsuzov, A. Neumaier, and V. A. Mandelshtam, Chem. Phys. Lett. **381**, 117 (2003).

[199] J. Liu and W. H. Miller, J. Chem. Phys. **125**, 224104 (2006).

[200] J. Liu, J. Chem. Phys. **134**, 194110 (2011).

[201] J. Liu, J. Chem. Phys. **140**, 224107 (2014).

[202] D. C. Marinica, M. P. Gaigeot, and D. Borgis, Chem. Phys. Lett. **423**, 390 (2006).

[203] J Beutier, D Borgis, R Vuilleumier, and S Bonella, J. Chem. Phys. **141**, 84102 (2014).

[204] M. Basire, D. Borgis, and R. Vuilleumier, Phys. Chem. Chem. Phys. **15**, 12591 (2013).

[205] A. Bose and N. Makri, J. Chem. Phys. **143** (2015).

[206] Q. Shi and E. Geva, J. Phys. Chem. A **107**, 9070 (2003).

[207] C. P. Lawrence and J. L. Skinner, Proc. Nat. Acad. Sci. **102**, 6720 (2005).

[208] J. A. Poulsen, G. Nyman, and P. J. Rossky, J. Phys. Chem. B **108**, 19799 (2004).

[209] W. H. Miller and C. W. McCurdy, J. Chem. Phys. **69**, 5163 (1978).

[210] M. Thoss and G. Stock, Phys. Rev. A **59**, 64 (1999).

[211] J. M. Moix, Y. Zhao, and J. Cao, Phys. Rev. B **85**, 115412 (2012).

[212] R. P. . Feynman and F. L. Vernon, Ann. Phys. **24**, 118 (1963).

[213] R. P. Feynman and A. R. Hibbs, *Quantum mechanics and Path Integrals* (Dover, New York, 2010).

[214] J. Liu, A. Nakayama, and N. Makri, Mol. Phys. **104**, 1267 (2006).